



8-2016

Fundamental Understanding of Bond Formation During Solid State Welding of Dissimilar Metals

Niyanth S

University of Tennessee, Knoxville, sniyanth@vols.utk.edu

Follow this and additional works at: https://trace.tennessee.edu/utk_graddiss

 Part of the [Metallurgy Commons](#)

Recommended Citation

S, Niyanth, "Fundamental Understanding of Bond Formation During Solid State Welding of Dissimilar Metals. " PhD diss., University of Tennessee, 2016.
https://trace.tennessee.edu/utk_graddiss/3959

This Dissertation is brought to you for free and open access by the Graduate School at TRACE: Tennessee Research and Creative Exchange. It has been accepted for inclusion in Doctoral Dissertations by an authorized administrator of TRACE: Tennessee Research and Creative Exchange. For more information, please contact trace@utk.edu.

To the Graduate Council:

I am submitting herewith a dissertation written by Niyanth S entitled "Fundamental Understanding of Bond Formation During Solid State Welding of Dissimilar Metals." I have examined the final electronic copy of this dissertation for form and content and recommend that it be accepted in partial fulfillment of the requirements for the degree of Doctor of Philosophy, with a major in Energy Science and Engineering.

Sudarsanam S. Babu, Major Professor

We have read this dissertation and recommend its acceptance:

Ryan R. Dehoff, George M. Pharr, Hahn Choo

Accepted for the Council:

Carolyn R. Hodges

Vice Provost and Dean of the Graduate School

(Original signatures are on file with official student records.)

Fundamental Understanding of Bond Formation During Solid
State Welding of Dissimilar Metals

A Dissertation Presented for the

Doctor of Philosophy

Degree

The University of Tennessee, Knoxville

Niyanth S

August 2016

Dedicated to memory of my uncle and mentor

Dr.Prakash Krishnaswami

Acknowledgements

I would like to express my sincere gratitude to my advisor **Prof Sudarsanam Suresh Babu**, but for his mentoring I would not be where I'm. His "dig deeper" approach made me go to the depths of the problem and his constructive criticism of the interpretation of my results and hypothesis helped me greatly to develop as an independent researcher. I really have to mention Suresh's unconventional style of teaching and his knack to simplify complex scientific phenomena into simple analogies, something that has made me passionate about thermodynamics and phase transformations.

I consider myself fortunate to have worked with **Dr Kurt Terrani** and **Dr Ryan Dehoff** at ORNL. Both Kurt and Ryan invested their valuable time towards my development as a researcher. They were instrumental in providing a platform to test my ideas and hypothesis and were always open for discussions and constructive criticism of my ideas.

I would also like to thank **Prof George Pharr** and **Dr. Hahn Choo** at UTK for being in my committee and always open to discussing my ideas, something that helped me develop a good problem statement to work on. In addition Prof Pharr's class on Nano indentation and small scale contact mechanics is easily the best class that I've ever taken where complicated maths was simplified into the actual physical phenomena. It was a class which gave me significant insight and appreciation for the nano indentation technique. I would like to thank **Prof. Lee Riedinger** Director, Bredesen center for providing an opportunity to engage in interdisciplinary research, something unique only to the students of the Bredesen center.

My thanks are also due to **Dr Aslan Miriyev** (previously with the Israeli Ministry of Defense (IMOD)) currently a post-doctoral fellow at Columbia University **Prof Nachum Frage** and **Asaf Levy** at the Ben Gurion University (BGU)-Israel for inviting and hosting me at BGU for

a month during the course of my PhD. The time I spent at BGU is easily one of the best parts of my PhD. In addition to providing a platform to develop international collaborations I got the opportunity to taste the delicious Israeli cuisine and also visit the historical sites during my stay!

A simple word of thanks would not be enough to thank **Dr. Dieter Isheim** and **Prof David Seidman** at the Northwestern University Center for Atom-Probe Tomography (NUCAPT) for their contributions. Both Dieter and Prof Seidman always welcomed me to use their atom probe and accommodated me during my numerous trips to Northwestern University. A special word of thanks to Dieter who was instrumental in me developing an appreciation for the atom probe technique. Our visits to the Tava Indian Restaurant in Evanston, where Dieter and I spent a lot of time discussing details of the atom probe technique is something that I will always cherish.

The acknowledgement section would be incomplete if I did not thank **Prof. Marcelo Dapino**, **Paul Wolcott** and **Tyler** from the Ohio State University and **Mark Norfolk** from Fabrisonics. They were always ready to help me out by providing samples whenever I requested them. I'm grateful to Paul for performing the push pin tests at OSU. Mark was a great sponsor and mentor and I consider myself fortunate to have worked with him for the past four years.

Discussions with **Ryan Smith**, **Avinash**, **Ben**, **Naren** and all the members of the Advanced Materials and Manufacturing Group (AMMG) have been very fruitful.

Last but not the least I would like to thank my parents and brother who always been a pillar of support and were always supportive of my dreams no matter what. I would also like to thank all my teachers and mentors for shaping me into the person that I'm today.

Abstract

Dissimilar metal welds are used in a wide range of applications to effect light weighting and for corrosion resistance. While fusion welding techniques are limited in their ability to fabricate dissimilar metal welds, solid state welding techniques are limited in their ability to fabricate complex geometries with dissimilar metal combinations. Hence alternative techniques need to be explored to fabricate complex geometries with dissimilar metals welds in the solid state. Ultrasonic additive manufacturing in a solid state additive manufacturing process that combines ultrasonic welding with mechanized tape layering to fabricate dissimilar metal welds in the solid state. Though extensive feasibility studies have been performed to fabricate dissimilar metal welds using ultrasonic additive manufacturing, the fundamental mechanisms related to the bond formation mechanism are not fully understood. In this work multi scale characterization using scanning electron microscopy, electron backscatter diffraction, nano indentation and atom probe tomography was performed to rationalize the mechanism of bond formation in dissimilar metal welds. The fundamental questions that needed to be answered were

1. Is possible for a solid state bond to form with extensive plastic deformation occurring only on one metal in a dissimilar metal combination
2. The effect of plastic deformation on the oxide layer at the interface of dissimilar metal welds.

To answer the above questions various dissimilar metal combinations (Steel-Ta) BCC-BCC, (Al-Ti) FCC-HCP, (Al-Steel) FCC-BCC were fabricated using ultrasonic additive manufacturing and characterized using the above-mentioned techniques. Bonded regions were characterized to study the role of plastic deformation by analyzing the micro texture developed at the interface. The general conclusion is the presence of a strong shear texture in the softer metal while the harder metal did not show any evidence of change in texture. To understand the effect of plastic

deformation on the oxide dispersion atom probe tomography analysis was performed and the results indicate the possibility of oxide breakdown resulting in oxygen super saturation in the lattice. The bond formation is hypothesized to occur as a result of plastic deformation localized in the softer metal alone.

Table of Contents

Chapter-1: Dissimilar metal joining

| | |
|---|----|
| 1.1. Dissimilar metal joining a perspective | 1 |
| 1.2. Friction Welding | 2 |
| 1.3. Friction stir welding | 4 |
| 1.4. Diffusion bonding | 7 |
| 1.5. High strain rate solid state welding | 8 |
| 1.6. Additive manufacturing to fabricate dissimilar metal welds | 11 |

Chapter-2: Ultrasonic additive manufacturing

| | |
|--|----|
| 2.1. Introduction and the evolution of VHP UAM | 12 |
| 2.2. Effect of Process parameters | 13 |
| 2.3. In situ observation of bonding using photon Doppler velocimetry | 14 |
| 2.4. Mechanical strength of UAM builds | 15 |
| 2.5. Solid State Welding | 16 |
| 2.5.1. Film Theory | 17 |
| 2.5.2. Energy barrier theory | 18 |
| 2.6. Multiscale characterization of Ultrasonic additive | 20 |
| 2.6.1. Nature of oxide dispersion | 20 |
| 2.6.2. Grain structure at the interface | 21 |
| 2.6.3. Microtexture studies at the interface | 24 |
| 2.6.4. Dissimilar metal joining using VHP UAM | 26 |

| | |
|---|-----------|
| Chapter-3: Problem statement and research objectives | 28 |
|---|-----------|

| | |
|---|----|
| 1.1.Problem Statement | 28 |
| 1.2.Research Objectives | 29 |
| Chapter-4: Experimental details | 30 |
| 4.1. Breakdown of the proposed tasks | 30 |
| 4.2. Optical microscopy | 31 |
| 4.3. Scanning electron microscopy and electron dispersive spectroscopy | 31 |
| 4.4. OIM using Electron backscatter diffraction | 33 |
| 4.5. Transmission electron microscopy | 35 |
| 4.6. Hardness measurements using load displacement sensing | 35 |
| 4.7. Mechanical testing | 36 |
| Chapter-5: Multi scale characterization of Al-Steel (FCC-BCC) dissimilar metal combination | 38 |
| 5.1. Introduction | 38 |
| 5.2. Experimental Procedure | 39 |
| 5.3. Sample Manufacturing | 39 |
| 5.3.1. Joint Characterization | 40 |
| 5.3.2. Results and discussions | 41 |
| 5.3.3. Conclusions | 46 |
| Chapter-6: Rationalization of bond formation mechanism in FCC-HCP dissimilar metal combination | 48 |
| 6.1. Introduction | 48 |
| 6.2. Experimental Procedure | 49 |
| 6.3. Results and Discussions | 50 |

| | |
|---|-----------|
| 6.3.1. Optical microscopy | 50 |
| 6.3.2. Electron Back Scatter Diffraction | 51 |
| 6.3.2.1. Characterization of original foil microstructure | 51 |
| 6.3.2.2. Microstructure evolution at the interfaces | 51 |
| 6.3.2.3. Misorientation and grain size distribution | 51 |
| 6.3.2.4. Evolution of micro texture at the interface | 53 |
| 6.4. Characterization of the heat treated samples | 55 |
| 6.5. Mechanical testing and fractography of builds | 56 |
| 6.6. Summary and Conclusions | 57 |
| Chapter-7 Rationalization of bond formation mechanism in BCC-BCC metal combination | 58 |
| 7.1. Introduction | 58 |
| 7.2. Experimental Work | 60 |
| 7.3. Results | 61 |
| 7.3.1. Scanning Election Microscopy and EDS of VHP-UAM builds | 61 |
| 7.3.2. Orientation Imaging Microscopy (OIM) using Electron Back Scattered diffraction | 63 |
| 7.3.3. Hardness measurements using Nano-Indentation | 67 |
| 7.4. Discussions | 69 |
| 7.4.1. Bond formation mechanism during VHP UAM | 69 |
| 7.4.2. On the evolution of grain structure at the interface | 71 |
| 7.4.3. On the texture evolution at the interfaces | 74 |
| 7.5. Conclusions | 76 |

| | |
|--|-----|
| Chapter-8 Summary and conclusions | 77 |
| 8.1. Summary | 77 |
| 8.2. Aluminum to steel | 77 |
| 8.3. Aluminum to titanium welds | 79 |
| 8.4. Steel to tantalum welds | 80 |
| Chapter-9 Future directions | 81 |
| 9.1. Future directions | 81 |
| References | 83 |
| Appendix | 99 |
| Vita | 137 |

List of Figures

- Figure 1.1 Typical continuous drive friction welding process (a) schematic showing fundamental steps and (b) plot of selected parameters versus time 100
- Figure 1.2 Schematic of friction stir welding process showing advancing and retreating side 100
- Figure 1.3 Experimentally determined concentration profiles of Mg at various depths across the weld center line for AA 1200 (advancing) and AA 6061 (retreating side) (b) Macrograph shows Fe and Ni in a transverse section illustrating the similar observation noted in (a) (c) Show the EDS data in the marked region in figure (b) 101
- Figure 1.4 Schematic illustration explaining the reason why the counterclockwise rotation of a pin cannot weld aluminum to steel: (a) clockwise rotation of a pin where the Al is transferred to the steel surface where the oxide has been removed resulting in a complete weld and (b) counterclockwise rotation of a pin where the Al is deposited on the side of the steel where the oxide layer is not removed by the action of the tool and hence welding is not complete. Note that in both the cases the steel is in the advancing side and the Al is in the retreating side but the direction of rotation plays a major role in determining if bonding occurs 102
- Figure 1.5 Sequence of metallurgical stages in diffusion bonding process (a) initial contact: limited to a few asperities (room temperature) (b) First stage deformation of surface asperities by plastic flow and creep (c) Second stage: grain boundary diffusion of atoms to voids and grain boundary migration (d) Third stage Volume diffusion of atoms to the voids 103

Figure 1.6 Effect of pressure on void formation of a titanium alloy diffusion bonded at temperatures of 980oC for 2 hours (a) Incomplete bond at 7.0 MPa (b) Complete bond at 10.0 MPa 103

Figure 1.7 Illustration of the wave formation process in explosion welding but can be applied to any high impact welding. The jetting process illustrated is key to the bond formation mechanism in explosively welded components 104

Figure 1.8 Shows the bright filed image on dislocation interaction and the cellular structure in AA6061 joint. The beam is along the [001]. The dislocation interaction at the grain interior where the grains were ~1micon away from the interface 105

Figure 2.1 Schematic showing the UAM process 105

Figure 2.2 Peel test data showing the effect of process parameters. Note that decreasing travel speed and increasing the amplitude has the same effect 106

Figure 2.3 Effect of process parameters on bond strength for Al3003 note the influence of travel speed 107

Figure 2.4 Increase in the vibration amplitude from 10 to 16 and increasing the preheat to ~150°C helped increase the LWD significantly 107

Figure 2.5 Results from the shear test showing no correlation between LWD and mechanical properties 108

Figure 2.6 Fractographs of both the specimens (a) High LWD and low strength showing no metallurgical bonding (b) Lower LWD and higher strength with metallurgical bonding 108

Figure 2.7 Welding of two gold Nano rods (a,b) One Nano rod (right) is caused to approach another (left) until their front surfaces come into contact. c–e, The welding process is

completed within 1.5 s (c-d) followed by structure relaxation (d-e). (f-i) After withdrawal of the STM probe (f-i), the as-welded nanowire is left in the free-standing state (i). Triangles indicate the front edges of the two Nano rods. Arrows indicate the withdrawing direction of the STM probe. Scale bars, 5 nm.

Figure 2.8 This indicates the fact that a threshold needs to be overcome to bond surfaces together. Fractographs of the faying surfaces of cold pressure welded Al, Cu and Ag at sub bonding strains. The strain was sufficient to cause oxide film rupture. The percentage deformations for various metals and the ratio of the oxide to metal is shown in figure 2.8(d)

Figure 2.9 Adhesion between metals increase with decrease in the recrystallization temperature. It was also observed that at higher temperatures the metals could be joined at lower deformations

Figure 2.10 Adhesion increases with plastic deformation

Figure 2.11 Comparison of builds fabricated with the (a) low power UAM (b) High power 9kW UAM processes

Figure 2.12 (a) Bonded interface shows continuous oxide layers. Dashed lines show possible interfaces of a pre-process asperity. White ‘flow’ lines indicate the possible directionality of the plastic deformation

Figure 2.13 Shows the ‘dumping’ of the oxide layers in the voids (Shimzu et.al,2014)

Figure 2.14 Interface showing grain refinement in Al-3003 (b)Interface showing grain refinement in Cu alloys (c) Interface showing grain refinement in Al-6061

Figure 2.15 (a) Comparing textures at different regions of the build (b)Comparing textures at different regions of the build in Al-6061

Figure 2.16 Variation of hardness across the interfaces. The drop in hardness while welding at higher amplitudes was attributed to softening due to adiabatic heating Note that there is no significant change in hardness when the normal load is increased 115

Figure 2.17 illustrating the bond formation steps involved in ultrasonic additive manufacturing 116

Figure 5.1 (a) (b) shows the SEM image of the interface showing continuous bond formation at the interface 117

Figure 5.2 Shows the results from the push pin tests (a) The push pin cure for the Al-Steel sample (b) Push pin test on the Al-Al weld Note the difference in the failure morphology. The Al-Steel weld fails by a shear while the Al-Al fails by de-bonding 117

Figure 5.3 Shows the SEM image of the fracture surfaces. (a) and (d) Shows the fractography of the failed surfaces. Where 1-4 corresponds to machined, shear, shear brittle, shear ductile, and ductile respectively. Details on the nomenclature of these terms are found in [refer] (b) and (c) Show the EDS maps of the fracture surfaces. Note the localized regions showing concentration of Fe indicative of material transfer 118

Figure 5.4 Shows the electron backscatter diffraction (a) Al-Steel build across 3 Al layers (b) Al-Steel interface at high magnification showing extensive deformation only in the Al (c) Al-Al interface showing deformation on both the sides of the interface 119

Figure 5.5 Shows the pole figures obtained from (a) Al-Steel dissimilar interface (b) Al-Al Similar interface. Note that in both the cases the Al shows a rotated cube texture. Also note that the texture strengths are different with the Al-Al showing a weaker texture while the Al-Steel interface shows a stronger texture 120

Figure 5.6 Shows the (a) Interface where bonding was complete (b) Region where sample extraction was performed (c) Tip after sharpening and polishing used for the analysis 120

Figure 5.7 Shows the reconstructed tips showing (a) Distribution of Al (b) distribution of Fe (c) Si distribution (d) O distribution (e) Mg distribution (f) C distribution. The respective interfaces are marked using arrows 121

Figure 5.8 Shows the presence of Oxygen peaks at 16 and 32 respectively confirming the presence of elemental oxygen at the interface 122

Figure 5.9 (a) shows the 6% Mg and Oxygen iso surface. Note the region marked using the black arrow indicating a region where there appears to be a local perforation in the oxide film (b) Shows Proxigram analysis performed along the direction marked using the red arrow (c) Shows the Proxigram analysis performed along the direction marked using the black arrow. Note that there is still considerable ~5 at% oxygen present in the region 123

Figure 6.1 (a) showing the schematic of the bilayer arrangement used to fabricate the build (b) Showing the optical micrograph of the build. The Substrate and the first bilayer. Note the regions where the Al-1100 flowed into the asperities created in the CP-Ti by the sonotrode 125

Figure 6.2 (a) IPF of as received Al-1100 (b) grain orientation spread of the Al-1100 sample (c) IPF of the as received titanium foil 126

Figure 6.3 (a) IPF overlaid with image quality maps showing (b) Showing the crystal orientations overlaid on an image quality map (c) Shows the grain orientation spread 126

Figure 6.4 Texture maps of Al-1100 (a) Layer-1 (b) Layer-2 (c) layer3 showing the presence of a strong $\{001\}<110>$ rotated cube texture 127

| | | |
|-------------|---|-----|
| Figure 6.5 | Showing the region of the interface where surface roughness is minimum. The diffusion distance and the thickness of the intermetallic layer is about 2-3 microns | 127 |
| Figure 6.6 | Showing the region of the interface near the sonotrode affected region showing significant interdiffusion of alloying elements. The diffusion distance and the thickness of the intermetallic layer is about 5 microns which is larger than that observed in figure 5.5 | 128 |
| Figure 6.7 | Shows the electron backscatter diffraction from the heat treated specimen. Note the grain growth at the Al interfaces while Cp-Ti does not show much difference. | 128 |
| Figure 6.8 | The results from the push pin tests on the as built and the heat treated samples | 129 |
| Figure 6.9 | Shows the failure morphology of the push pin specimens (a) Heat treated (b) As built | 129 |
| Figure 6.10 | Shows the fractographs of the as welded specimen. (a) Shows the presence of localized ductile failure at the interface (b) Shows the Al distribution map (c) Shows the Ti distribution map. Showing the absence of Ti in the region where the sample failed in a ductile fashion meaning complete bonding between the Al and Ti layers at that location | 130 |
| Figure 7.1 | Schematic illustration of build fabricated by VHP-UAM and specimens cut off from the build (indicated by a dotted line) | 131 |
| Figure 7.2 | (a) SEM image showing bonded regions voids and the waves (b) SEM image showing waves at the interface | 131 |
| Figure 7.3 | SEM micrographs of the Ta steel interface (a) Sliding debris (b) EDS spectrum of the debris | 132 |
| Figure 7.4 | EDS maps show oxygen concentration at the interface and in the sonotrode affected regions | 132 |

| | |
|---|-----|
| Figure 7.5 Microstructural characteristics of the unbounded area (a) Inverse pole figure of the unbonded region (b) Grain Orientation spread of the subject region(c) Image quality index of the corresponding region | 133 |
| Figure 7.6 Microstructural characteristics of the bonded area (a) Inverse pole figure of the bonded region (b) Corresponding GOS (c) IPF of the a bonded region in higher mag (d) Corresponding GOS map | 134 |
| Figure 7.7 Microstructural characteristics of a heavily deformed region (a) Inverse pole figure (b) Misorientation distribution for grain-1 , grain-2 and grain-3 | 135 |
| Figure 7.8 Grain size distribution in the both the bonded and the broken interface | 135 |
| Figure 7.9 (a) Texture at the region where bonding was observed (b) micro texture at the region where excess deformation was observed | 136 |
| Figure 7.10 (a) Load Vs. displacement curves on the Ta side of the interface (bonded) (b) Load vs. displacement curves on the Ta side of the interface (not bonded) (c) Load vs. Displacement curves on the steel side of the interface | 137 |

Chapter-1

Dissimilar metal joining

1.1. Dissimilar metal joining a perspective:

Dissimilar metal welds are used in a wide range of applications such as power plants [1], automobile [2] and aerospace industries [2]. Though it is possible to join dissimilar metals using fusion welding, there is a possibility of formation of intermetallic compounds (IMC's) as a result of high temperatures. IMC leads to deterioration of properties at the interface. Hence solid state welding has been widely adopted to join dissimilar metal welds for various applications. Solid state welding processes are those that produce coalescence of the faying surfaces at temperatures below the melting point of the base material joined without the addition of a braze or a solder filler metal. This may be achieved with or without the application of pressure and temperature [3]. While there are certain similar metal combinations fabricated using SSW techniques for economic reasons, there are wide range of dissimilar metals that are fabricated using SSW since there is no other technique that can be used for fabrication [2]. There is a wide range of solid state welding techniques available to fabricate dissimilar metal welds. The most popular solid state welding techniques used in the various industries to fabricate dissimilar metals are

- i. Friction welding
- ii. Friction stir welding
- iii. Diffusion bonding
- iv. Explosive welding and other high energy process

This chapter aims to provide the reader with the current state of the art on dissimilar metal welding in the solid state. The various bond formation mechanisms in different welding techniques are also

explored. Finally the relevance of additive manufacturing to fabricate dissimilar metal combination is explored.

1.2. Friction Welding:

As the name implies both the technique utilize frictional heat for joining [4]. The heat is produced by relative motion of the two interfaces being joined thereby relying on the direct conversion of mechanical energy to thermal energy without application of heat from an external source [3]. This process is classified into direct drive and inertia friction welding based on the drive used for joining [5]. The most commonly used friction welding is the direct drive friction welding. The major process parameters used to control the joint quality are the speed of rotation, friction load and duration of welding [6]. The welding proceeds in three stages, which can be characterized by distinct stages [7]. The steps involved are shown schematically in figure-1. During the first stage the torque increases continuously and reaches a steady state, which marks the beginning of the second stage [4, 5, 7]. The first two stages are the friction stages where the two sides are rubbing with adhesion taking place in several locations. When the adhesion is strong enough then material transfer takes place by local shearing and the interfacial temperature and torque continuously increases. With the increase in temperature the metal becomes plasticized and flows plastically. This results in the decrease in the torque and also prevents further rise in temperature, which is the second stage of the welding process [4]. The final stage is characterized by the application of the forge pressure[7]. The temperature drops steadily and the torque reaches a terminal peak as shown in figure 1(b). The application of the forge pressure causes axial shortening due to local extrusion of the metal at the interface called the flash, which is machined off [4]. The drop in temperature is attributed to the decrease in speed which consequently results in the cooling down of the weld [4]. Lucas showed that the forge has a dominant effect on joint strength since the forge serves to

contain the rate of frictional heating [6]. It was reported that without the forge pressure Austenitization and rapid grain growth of steel would take about 2 seconds. Thus the forge step prevents HAZ softening as a result of grain coarsening [6]. However the kinetics of the feasibility of the above process of grain growth was not taken into account and was not elaborated. Though a wide range of similar and dissimilar metals can be fabricated using friction welding the primary requirements for metals are that it should be (i) Forgeable (ii) Should generate frictional heat. Hence it is challenging to fabricate brittle and self-lubricating materials such as grey iron and materials such as copper with a high thermal conductivity [4] using this technique [3].

Taking into account the temperature rise and microstructure characterization at the interface Maalekian proposed that diffusion was the primary bond formation mechanism contributing to friction welding [5]. Hence the mutual solid solubility of metals is a factor that needs to be considered while fabricating dissimilar metals. Since the heating time during friction welding is relatively short it has been hypothesized that the extended cooling time contributes to the joint formation [5]. A wide range of dissimilar metals with widely different melting points has been successfully fabricated using this technique [4, 5]. Intermetallic layers (IMC) are reported while friction welding of aluminum alloy with stainless steels [8], Titanium alloys [9] and steels [10]. Yilbas et.al reported that IMC formation degrades joint strength for Al-Steel welds only if the thickness of the IMC exceeds 0.2-1 μ m [11]. In the case of Al-Cu welds the thickness of the intermetallic layer at the interface is not uniform but is thicker at the mid radius and thinner at the periphery. The thickness of the intermetallic layer was found to increase with an increase in the speed of rotation and a decrease in the load [11]. The tensile strength of the Al/IF steel varies inversely with welding time. This was because it was hypothesized that Al and steel welding took place over an intermetallic phase and the properties vary with the changes in the thickness of the

intermetallic layer [4, 5, 11]. The dominant factor influencing the joint strength in Al-Ti friction welds was also hypothesized to be the intermetallic layer thickness [9, 12]. However one major problem with welding dissimilar metals using friction welding is the formation of low melting phase formation at the interface. In particular the low melting phase can be formed in Ti-Steel systems and Al-Mg system [3]. The other problem that can arise is hot shortness in steels where excessive sulfur can result in the formation of low melting eutectics resulting in the formation of liquid phase at the interface [3].

1.3. Friction stir welding:

This is another solid state joining technique in which a rotating tool with a shoulder and terminating in a threaded pin moves along the butting surfaces of two rigidly clamped plates placed on a backing plate [2, 13]. A schematic of the process is shown in figure-2. In this process the shoulder of the pin generates heat and the heated plasticized material flows and completes the joint [2, 13]. The unique feature of friction stir welding is the fact that that transport of heat is accomplished by the flow of the material [13]. Most of the heat is generated in the advancing side while the material flow occurs along the retreating side of the tool [13]. The various process parameters that control the joint characteristics are welding speed, the tool rotational speed, the vertical pressure on the tool, the tilt angle of the tool and the tool design [13]. The peak temperature varies directly with welding speed and axial pressure. The torque, which provides a direct indication of the amount shear stress, varies inversely with tool rotation speed and the axial pressure. This is due to an increase in the temperature with increases tool rotation and pressure causing the material to deform more readily leading to a drop in the shear stress at the interface [13]. The heat generation is not influenced by the welding speed and hence the shear stress varies

inversely with the welding speed. While attempting to fabricate dissimilar metals using friction stir welding the following factor need to be considered

- i. Difference in the deformation behavior
- ii. Possibility of formation of detrimental intermetallic phases
- iii. Differences in the physical properties such as thermal conductivity [2]

This discontinuity of properties across the butting surfaces has a large influence on the stirring properties of the materials. Hence one of the most important aspect in friction stir welding of dissimilar metals is the selection of appropriate alloys for the advancing and the retreating side to obtain optimum mixing and hence mechanical properties [2]. During FSW of steel it was observed that by placing the steel in the advancing side the amount of martensite formed increases since the maximum temperature rise is observed in the advancing side [14]. Watanabe et.al showed that the tool rotation direction played a major role in joint formation [15]. When the steel was in the advancing side then a clockwise motion rotation of the pin achieved bonding whereas a counter clockwise direction did not achieve bonding. The rationale provided was that by rotating the pin counter clockwise the plasticized Al was transferred to the steel surface ahead of the tool, where the oxide removal in the steel was not complete. A schematic illustration of this process is shown in figure-3. This study points to the importance of oxide removal stage during friction stir welding of metals. This action by the tool removed oxide and carried the oxide particles into the Al matrix. Similarly while placing the steel in the retreating side bond formation was incomplete since it was difficult for the harder steel to flow around creating a joint [15]. Ayers et.al showed that during dissimilar welding using FSW the flow of the plasticized material depends on the distance from the shoulder and is complex [16]. In friction stir welds of dissimilar metals no evidence of intimate mixing or formation of solid solutions have been reported though extensive mechanical mixing has

been observed [2, 13, 15, 16]. Chen and Nataka while attempting to make Al-Steel dissimilar metal welds used Steel produced by hot dip galvanizing and observed enhanced strength [17]. They attributed the improved strength to the localized melting of Zn which exposed the nascent oxide free surfaces to promote a Zn-Al interfacial reaction leading to the formation low melting Al-Zn eutectic. The expulsion of this low melting eutectic phase aided by the pressure and plastic flow brought the Al-Steel nascent surfaces into intimate contact leading to the enhanced strength of welds [17]. The improvement of mechanical properties due to the formation of intermetallics was observed by Yamamoto et.al while friction stir welding Al and Mg [18]. They showed that the loads to failure for Al-Mg dissimilar metal were larger when the intermetallic thickness was 800nm and when it exceeded 1800nm the loads decreased sharply and fracture occurred at the intermetallic region [18]. The reason provided was that increased intermetallic thickness at the interface decreased the extent of mechanical interlock at the interface though this hypothesis was not elaborated. P.Xue et.al reported bond strengths in excess of 210MPa for Al-Cu friction stir welded joints when the thickness of the intermetallic layer was less than 1000nm [19]. Tanaka et.al also made similar observations [20]. However Watanabe et.al observed that the intermetallic sites served as regions where cracking initiated.[15]. The intermetallic formation was also not homogenous but formed only on the upper region of the weld where the temperature was the highest. The rise in temperature in the upper region was attributed to the friction between the shoulder and the top surface of the build [15]. However no quantitative measurement of the thicknesses of the intermetallics was made. Though friction stir welding has been effectively used to join steels rapid tool wear remains a major concern [21].

Chen and Nataka have successfully welding ADC12 Al alloy to CP Ti and observed that the interface strength was about 62% of that of the Al ADC12 alloy [22]. They attributed the decreased

strength to the formation of voids along the Ti side of the interface due to the insufficient flow of Ti. They also attributed bonding to interdiffusion of Al and Ti specimens and the formation of a thin interfacial layer [22]. The thickness of the intermetallic layer, which consisted primarily of TiAl_3 , was observed to vary with travel speed. The travel speed controlled the extent of heat input into the material. A high travel speed lead to incomplete bonding while a low travel speed lead to excessive heat generation resulting in the severe softening of Al which consequently lead to poor tensile properties [22]. Though Nandan et.al [13] proposed that decreasing the welding speed only moderately affected the heat input the results of Chen and Nataka seem to suggest that the welding speed does play a major role in controlling the heat input and hence the bond formation [22]. However no modeling was performed to confirm the above hypothesis.

To conclude in the case of friction stir welding, the “stirring” action of the tool provides a means to make the plasticized material flow leading to convective transfer and oxide removal. This flow of material leads to extensive mechanical mixing at the interface. There are relatively fewer studies that explore the role of oxide removal and asperity collapse during bonding. Majority of the research in friction and friction stir welding seem to indicate that intermetallic formation is central to bond formation during dissimilar metal welding. However they don’t explain the bonding mechanism for dissimilar metals that don’t form intermetallic compounds.

1.4. Diffusion bonding:

Diffusion bonding is a solid state joining technique where two nominally flat interfaces can be joined at an elevated temperature using an applied pressure for a time ranging several minutes [23]. The temperature is selected such a way that the temperature is between $0.5-0.8T_m$ and the pressure causes no macroscopic deformation of the material [3]. There are two variants of diffusion bonding

- i. Solid state: Where bonding is achieved by asperity collapse and oxide layer disruption
- ii. Transient liquid phase: where a liquid is formed and as a consequence of continued interdiffusion at the bonding temperature isothermal solidification occurs to effect the bond [3].

Similar to friction welding the most commonly dissimilar metal combinations joined using this technique are Al-Ti, Al-Steel, Al-Mg and Steel-Ti. Bonding takes occurs in a series of stages. The stages themselves cannot be discretely defined. During the first stage the contact area grows to a large fraction of joint by localized deformation of the contacting asperities. As this stage nears completion the interface becomes a discrete line with several voids inbetween separating it. The voids are then eliminated by grain boundary diffusion (i.e. surface diffusion) and grain boundary migration. The final step in the bond formation is the volume diffusion of atoms to the voids to close down the voids. Creep and diffusion mechanisms are important for this stage of the bond formation [3, 23].

1.5. High strain rate solid state welding:

This is a solid state welding technique that uses high the energy from impact from colliding metal surfaces to create a joint [3]. Impact energy welding has the potential to join a wide range of dissimilar metals that are thermodynamically incompatible [24]. The impact energy needs to have sufficient energy to cause the colliding surfaces to flow hydro dynamically to promote the solid state bond [25]. The solid at the interface is not able to support the huge shear stress at the interface and hence the material behaves like a fluid for a short period of time. The mechanism of bond formation depends on the jetting action at the interface where the jet waves clean up the oxide layers resulting in atomistic contact [26]. However Hammerschmidt and Kreye rejected that idea that explosion welding was a solids state welding and that bonding occurred by localized melting at

the interface [27]. They proposed that the melt cooled at a rate greater than 10^5Ks^{-1} resulting in the observed ultra fine grains [27]. However Akbari et.al modeled the explosive welding process using the AUTODYNE® predicted that the temperature rise is in fact less than the melting point of the metals investigated and cast doubts if there was actually localized melting at the interface [25]. Zhang et.al performed electron backscattered diffraction analysis on Al welded using magnetic pulse welding and observed significant grain refinement with inter grain misorientation in excess of 15° [28] In another independent study Zhang et.al observed that the grains have significant dislocation density [29]. The presence of dislocations shows that melting at the interface does not occur. Despite the debates about a localized melting at the interface, impact welding is widely recognized as a solid state weld where the jetting action at the interface results in the bonding. The energy source used for the impact welding can range from (i) Explosives [25] (ii) Electro magnetic force [24] (iii) Laser assisted ablation [30]. The strain rates for such process can exceed 10^7s^{-1} . In contrast the strain rate for friction stir welding is estimated between $5\text{-}10 \text{s}^{-1}$.

The major process parameters used to control the process are impact angle and the impact velocity. Several dissimilar metal weld combinations have been explored using this technique. The most common dissimilar metal combinations explored are Al-Steel, Steel-Cu, Al-Cu [31] and Ti-Steel [32]. For a constant impact angle a large velocity leads to excessive melting resulting in interfacial reactions leading to formation of brittle intermetallics [25]. The velocity of the plate needs to be lesser than the velocity of sound in either material. However a low impact velocity does not lead to the jetting action leading to incomplete bonding. This impact energy results in an increase in temperature at the interface albeit for a short time [25]. Wu et.al showed the presence of intermetallic formation in Al-Cu welds made using magnetic pulse welding [24]. Marya and Marya studied the microstructure of copper and Al and reported a hard intermetallic phase with the same

composition as that of the equilibrium Cu_2Al phase and interfacial voids which were used as evidence for Al melting [31]. However Wu et.al showed that the intermetallic formation in Al-Cu can in fact occur without melting in the interface [24]. However the formation of intermetallics at the interface is the subject of much debate where Kahraman et.al did not observe any intermetallics at the interfaces of Ti-Cu fabricated using explosive welding [33]. Aizawa performed feasibility studies on Al and steel magnetic pulse welding and observed that the strength of the interface always exceeded the strength of the weaker metal. Acarer explored the feasibility of joining Al-Dual phase steel and Al-HSLA steel [34, 35]. In both cases he reported that the interface did not exhibit any waves, but nevertheless had acceptable tensile and shear strength [34, 35]. However the authors did not explicitly state the acceptability criteria used to evaluate the welds. While attempting to weld Cu-Steel the authors observed that increasing the stand off distance and the explosive ratio did in fact result in the formation of waves. This was attributed to higher velocities of the flyer plate. They also recorded an increase in the hardness as the explosive content was increased which coincided with increased deformation at the interface. Zhang et.al performed detailed characterization using TEM and nano indentation on Al-Cu interfaces made using magnetic pulse welding. They reported an increased hardness the interface and related the increase in hardness to (i) grain refinement and (ii) increased dislocation density [29]. There are several unanswered questions relating to the fundamental bonding mechanism of impact welding. The current understanding is based on post welding characterization and it shows that the bonding mechanism is actually a combination of various mechanisms such as mechanical interlocking, physical bonding which involves atomic adhesion and chemical bonding which involves the formation of intermetallics. Melting at the interface is a function of input energy. So finally based on the literature it can be concluded that the level of contribution from each mechanism depends on

the input energy. To solve the question of intermetallic formation at the interface it is necessary to perform multiscale characterization of the weld interfaces made using a wide range of energies to determine the threshold energy level beyond which melting and intermetallic formation occurs.

1.6. Additive manufacturing to fabricate dissimilar metal welds:

Since its inception in the late 1980's additive manufacturing technologies has experienced more than 20 years development and presently one of the rapidly developing advanced manufacturing techniques in the world. Additive manufacturing is the layer by layer shaping and consolidation of feedstock to arbitrary configurations normally using a computer controlled laser as the energy source [36]. Apart from the ability to fabricate dissimilar metals additive manufacturing has the ability to fabricate fully functional parts. This makes it a relevant tool to fabricate dissimilar metal welds for heat exchanger applications and transition joints. Though there is wide range of additive manufacturing processes, only two processes have been used to fabricate join dissimilar materials.

- i. Laser directed energy deposition
- ii. Ultrasonic additive manufacturing

The directed energy deposition is a fusion welding technique that uses a high power laser to melt powder and deposit the molten powder on a substrate. Ultrasonic additive manufacturing however is a solid state hybrid manufacturing process which produces full scale parts by welding metallic tapes together in the solid state. Both these processes have their own merits and the remainder of the thesis focuses on utilizing advanced manufacturing techniques to fabricate and weld metals in the solid state. A detailed description of the process will be provided in the further chapters.

Chapter-2

Ultrasonic additive manufacturing

2.1. Introduction and the evolution of VHP UAM:

Ultrasonic additive manufacturing (UAM) is a new layered additive manufacturing technique that combines ultrasonic welding and mechanized tape layering to create solid state near net shape metallic parts as shown in figure 2.1. It involves applying an ultrasonic oscillation typically 20 kHz locally applied to the foils through a metal sonotrode under a static normal force [37]. At the beginning of each sequence, a new foil is placed over the previous layer and tack welded using low energy. Following tack welding at the edges of the foil and securing the foil the bonding is achieved by welding with a higher energy input. Consequently due to the nature of the process the rough surface texture of the sonotrode leave it's "imprint of hills and valleys" on top the surface where the sonotrode has been in contact with the foil. This has been termed as "sonotrode induced roughness" and has been hypothesized to be the primary cause of voids in the part. The voids are hypothesized to occur since the smooth top foil cannot flow into the valleys caused by the sonotrode.

The exact mechanism of bond formations is still not clear and it is widely believed that the process is similar to forge welding, which depends on extensive plastic deformation but not melting. Due to the virtue of the solid state nature of the process it benefits over conventional welding. One of the greatest advantages of the ultrasonic additive manufacturing process is that it combines the advantages of solid state welding and additive manufacturing to fabricate complex shapes and it's ability to fabricate hybrid materials. Due to these advantages there is significant interest in using this technique to fabricate dissimilar metals due to its low temperature rise at the interface.

2.2. Effect of Process parameters:

Significant advances have been made to understand the role of process parameters on the bond strength over the years. The major processing parameters used to control the power input are the vibration amplitude, the normal force and the travel speed [38]. Apart from the parameters that are listed above the role of pre heat [38], post weld heat treatment [39] and surface roughness of the foil [39] has also been extensively studied. The major area of focus of these researchers was to primarily minimize the total void fraction at the interface. The void fraction at the interface is quantified using the linear weld density, which is defined as the ratio of the bonded interface to the total length of the interface. The effect of the process parameters have been correlated to the LWD to identify a suitable processing window and it is widely agreed that increasing the vibration amplitude increases the LWD up to a certain limit and beyond which any further rise results in a poor LWD due to the breaking of the formed bond, which is shown in figure 2.2[38]. The reason why vibration amplitude has such a high influence on bond formation can be rationalized by the results shown by Tabor [40] on adhesion of metals and Tylecote on solid state joining of metals back in the 60's [41] where they documented that imposing a tangential force leads to an increase in metal transferred across the interface through adhesion. The contact areas were measured for various sliding pairs along the interface using electrical resistance measurements and it was observed that increasing the tangential force allowed for increased contact areas across the interface aided by enhanced plastic flow [42].

The normal force does play a minor role in the improving the LWD but however a sharp drop in the LWD occurred when the normal force was increased beyond 1900N [38]. This drop could be attributed to the fact that increasing the normal load could probably restrict the scrubbing action between the foils resulting in poor oxide dispersion and plastic deformation. Travel speed

showed a linear response where a decrease in the travel speed increased the LWD. The preheat temperature showed a linear increase in the linear weld density and it was attributed to improved plastic deformation occurring at the interface which resulted in a lower void fraction. However it was also hypothesized that preheating beyond a temperature may cause a decrease in the LWD since the material may oxidize more rapidly resulting in a bond degradation. The effect of the processing parameters on the mechanical strength was also studied using similar statistical tools by Kong et.al who then identified the processing window for Al 3003 [43] and Al 6061 [44] using mechanical testing and linear weld density. The changes in the mechanical properties with changes in process parameters are shown in figure 2.3 and 2.4. The data seemed to agree with the above results showing that the increasing the amplitude and normal force and decreasing the travel speed increased the LWD and enhanced strength at the interface. Based on this it was hypothesized that the friction at the interface led to interfacial heating and plastic deformation leading to the oxide removal from the interface leading to bonding at the interfaces.

2.3. In situ observation of bonding using photon Doppler velocimetry:

Based on the observations of Ramanujan et al. three conditions could be occurring during welding

- (a) When the normal force is low then the sonotrode may just slid over the top surface of the foil without transferring the energy into the interface
- (b) When the normal force is high and the vibration amplitude is low then it leads to the sticking of the sonotrode on the foil leading to no bonding.

These observations lead us to understand that there is a specific range of process parameters that lead to optimum bonding. Foster performed several elegant experiments using photon Doppler velocimetry to study the various stages of bonding during UAM [45]. Bonding

behavior was rationalized by measuring the relative velocities of the sonotrode, top foil and bottom foil.

By performing PDV Foster et.al observed that as the sonotrode approaches the bond zone (where the PDV sensors are positioned), the foil and the substrate “feel” the compressive force from the sonotrode. The direct result of the normal force is felt as a drop in the velocity of the top foil. This initial condition is called the “stick” condition where the sonotrode “locks” on to the top foil. With an increase in time the top foil bonds to the substrate with the further increase in the normal force the foil bonds, which is evident from the increase in the substrate velocity. However for an unsuccessful bond these results don’t show any changes to the velocity [45]. However no follow up and complementary characterization was performed at the regions where the PDV was performed to rationalize the macroscopic bonding behavior to the microstructure. This could be an interesting active area of future work and could possibly offer more insight into the fundamental bond formation mechanisms.

2.4. Mechanical strength of UAM builds:

Hopkins et.al carried out extensive DOE and using ANOVA techniques showed that the mechanical strength could not be correlated to the linear weld density [46]. They hypothesized that the bond strength is related to the extent of metallurgical bonding present between the foils being consolidated. The justification for such a hypothesis is based on the observation that builds made using parameters yielding lower linear weld density showed improved strength and ductility compared to the builds with a higher linear weld density[39] as shown in figure 2.5. On examination of the fractured surfaces, Adam showed that several distinct features on the fractographs shown in figure 2.6. He classified them into the following the

- i. Ductile

- ii. Shear ductile
- iii. Brittle
- iv. Machined

The ductile regions were the regions where metallurgical bonding occurred. Using point count method it was shown that samples showing a higher mechanical strength showed a higher fraction of the ductile feature on the fractographs. Hence it was hypothesized that it was necessary to maximize metallurgical bonding to maximize strength. To get a conceptual idea about metallurgical bonding it is important to understand the mechanisms of solid state welding.

2.5. Solid State Welding:

Solid state welding processes encompass all the methods in which metallic bonding occurs without the presence of re-solidified metal. Though there are studies where claims are made where there is localized melting at the interface leading to bonding [47, 48] the evidence is not convincing primarily because Gunduz et al [47], have hypothesized that in order for melting to occur the vacancy concentration should be close to 0.1% at the interface which is not practically feasible. It was shown in Dehoff [49] that melting occurred in certain conditions where the sonotrode did not lead to a “sticking condition” as previously stated but was merely sliding on the foil. However it is clear that melting in this case was not integral to the formation of bond and hence UAM can be classified as a solid state weld. The driving force for the formation of solid state bonds is the reduction of surface free energy [3]. The surface energy is defined as the increase in energy of a system divided by the area A caused by the creation of a new surface

$$\Gamma_{\text{surf}} = \Sigma \Delta E_i / A \text{-----}(1)$$

The atoms that contribute to the extra energy are usually within 10 lattice parameters or less of the surface. A freshly created surface has a higher energy while a relaxed surface has a

lesser free energy. The interfacial energy is the same as the surface energy but however there are two reference states

$$\Gamma_{\text{interface}} = [\Sigma \Delta E_i (A) + \Sigma \Delta E_i (B)]/A \text{-----}(2)$$

The ideal adhesion energy is the difference between the two surfaces and the interfacial energies

$$\Gamma_{\text{adhesion}} = \Gamma_{\text{surface}} (A) + \Gamma_{\text{surface}} (B) - \Gamma_{\text{interface}} (A/B) \text{-----}(3)$$

For a solid state weld to form the energy of adhesion needs to be minimized. This can be achieved by the formation of the atomic level bonds reducing the number of unsatisfied bonds in the surface. For the formation of the atomic level bonds it is important to bring the atoms on the surface into intimate contact such that their electron clouds overlap leading to the formation of a solid state bond [3]. This reduction in the surface energy can be achieved by a number of methods and there are two theories

2.5.1. Film Theory:

This theory proposes that pure metals without any oxide layer/surface impurities brought into intimate contact form a solid state bond immediately [3]. The plastic deformation necessary to initiate bonding merely serves to fragment the oxide film at the surface of the metal [23, 50] [51]. To explain the differences in weldability of various metals, this theory proposes that the differences arise from the differences in the properties of the oxide layer in the surface [52]. Vaidyanath et.al have expressed that the film theory is the major mechanism of joining since it was observed that bonding could be achieved when deformation causes the oxide layer to fragment [53]. The evidence for this theory was observed using in situ STEM where gold nano wires brought into contact joined spontaneously [54]. While this theory holds good for materials such as gold which don't have any oxide film this cannot explain as to why the extent of deformation required for welding metals such as Al, Cu is much higher than that required to fragment the oxide film as shown in figure 2.8. For

instance Parks observed that even when clean surfaces were brought into contact no bonding was observed and hence hypothesized that there might be other mechanisms operating [55].

2.5.2. Energy barrier theory:

The energy barrier theory states that even when both the metals are brought into intimate contact no weld will result since there is an energy barrier that needs to be overcome. Parks hypothesized that this energy barrier can be overcome by recrystallization [55]. The reason recrystallization had to occur at the interface to promote bonding was attributed to the fact that after overcoming the energy barrier the bond line is characterized as a highly dislocated high energy structure. Hence recrystallization had to occur at the interface to lower the overall energy of the system and it was hypothesized that decomposition of the interface by recrystallization gives better bond performance [55]. However it has been shown that this “energy barrier” can be overcome by extensive plastic deformation. For instance in the case of Al it has been shown that at least 40% reduction in area is necessary to initiate a solid state weld. The role of plastic deformation is to collapse the asperities on the surface of the metals. A simple rationalization for joint formation in solid state welding is the force applied causes the asperities to yield and plastically flow. This brings about the collapse of asperities thus bring the metal surface into contact [51] [41, 56]. The relative ease with which metals can be welded in the solid state can be obtained from the adhesion coefficient of metals. A high adhesion coefficient corresponds to easy welded in the solid state and vice versa. It is shown that the adhesion coefficient of metals increases with plastic deformation meaning that as the percentage deformation increases metals is welded easily as shown in figure 2.9 and 2.10. In most solid state welding techniques the imposed plastic deformation is not pure uni axial compressive but rather there is also a shear load brought

about by the sliding motion at the interface. Tabor hypothesized that adhesion occurs by the following two step process.

Step-1: When the surfaces are placed together under a normal load and plastic flow causes the asperities to yield creating a junction

Step-2: On the application of the shear load by the sliding motion the joint starts to flow plastically resulting in the bond expanding [40]

Based on the evidences of the proposed theories it can be concluded that the major conditions for solid state bonding to occur are

1. Oxide removal at the interface
2. Creating an atomistically flat surface to initiate contact with the nascent materials [41]

The second step involves the plastic flow of metal and the differences in solid-state weldability in dissimilar materials could be attributed to the difference in the stacking fault energy, hardness ratio and the plastic properties of oxides. Thus when the metals are brought into contact an energy barrier should be overcome before welding can take place. As pointed out previously there is no consensus if this energy barrier is recrystallization or plastic deformation or both [50]. However the role of plastic deformation in solid state joining is well recognized.

UAM being a completely solid state bonding it was recognized that increasing the power input is necessary to extend the process to join high strength materials. The traditional UAM delivers power up to 1.5kW using a single transducer low power UAM system. In contrast VHP UAM delivers power levels close to 9kW of power at 20 kHz resonant frequencies using two piezoelectric transducers instead of one on either side of the sonotrode. The transducers cause the sonotrode to that vibrate longitudinally and 180° out of phase, in “push–pull” mode, thereby reinforcing their displacements. Consequently, the sonotrode is set into vibrations at amplitudes of

up to 52 μm (twice as large as that of the UAM machine) under a static normal force of up to 15 kN (seven times larger than in the UAM machine)[57]. As a consequence of increasing the power input, builds fabricated using VHP UAM (9kW UAM) showed lower void fractions at the interface as shown in figure 2.11. Extensive multiscale characterization techniques have been used to understand the role of oxides, plastic deformation and recrystallization at the UAM and VHP UAM interfaces.

2.6. Multiscale characterization of Ultrasonic additive manufactured builds:

2.6.1. Nature of oxide dispersion:

Before discussing the characterization results from the UAM literature it is pertinent to go back to the research done on pressure welding, cold roll bonding and adhesion since they all relate to UAM. Majority of the seminal work in this area was carried out during the 60's. Adhesion and roll bonding showed that the plastic deformation is a pre requisite for oxide film breaking. There is no consensus in the solid state joining literature about the role of the oxide film at the interface. It has been shown for metals such as gold that oxide free metals when contacted bond instantly [54], however when tried with other metals a threshold deformation existed until which bonding could occur [41]. It was hypothesized that even while welding similar materials the oxide film need not fracture independently and that although the oxide film fractures on one surface it is quite possible that oxide layers may still cover the corresponding area on the opposite end [50]. The rationale that was postulated was that the threshold deformation required for initiating the solid-state weld in fact was used to fracture the unbroken oxide layer. Another hypothesis considers the ratio of hardness of the oxide layer and the metal. A high ratio would lead to complete fragmentation of the oxide layer at relatively low loads e.g. Aluminum and correspondingly a low ratio would mean that the oxide layer is ductile and needs relatively higher levels of deformation to fracture. The critical deformation for bonding is related to the ratio of the hardness of the metal oxide to the metal [41].

Research on the oxide fragmentation and dispersion at the UAM and ultrasonic spot-welding interfaces has not been extensive. The major techniques used to study these phenomena were scanning electron microscopy, DB-FIB [49, 58, 59], transmission electron microscopy [49] and Auger electron spectroscopy [60]. Johnson [58, 59] used a DB-FIB in conjunction with a TEM and observed oxygen enrichment of up to 13.8 Atomic% against a 1.6 atomic% in the bulk. He also correlated that the dispersion of the oxide layer was a strong function of the extent of plastic deformation that the underlying material exhibited. Johnson also observed a continuous film of oxide layer at the interfaces of Al-3003 alloy fabricated using UAM and attributed that to the lower vibration amplitude that resulted in the less effective oxide removal at the interface [59].

Dehoff et.al [49] used similar techniques and characterized an Al-3003 build made using a VHP UAM process with higher amplitude and force levels. He also reported similar observations and reported that a continuous layer of oxide was present at the interface. Later work by Shimizu et.al [61] showed that the surface oxide layer was broken down and gets squeezed to the nearby voids and that the solid-state weld occurs only at the places where the oxide layer is removed. Typical results on the oxide dispersion are summarized in figure 2.12 and 2.13. However the evidence was based only on EDS data and no atom probe tomography analysis was performed to quantify the %Oxygen at the interface. Such experiments coupled with valance EELS maps could give us more insight as to what happens to the oxygen at the interfaces.

2.6.2. Grain structure at the interface:

Johnson et.al [58] were the first to characterize the grain structure in Al-3003 samples made using UAM and observed significant refinement at the interface of the builds and also observed using TEM that the refinement was more pronounced at the surfaces where the sonotrode came into contact than by the interface deformation alone. He attributed the microstructure to

plastic deformation alone and the role of adiabatic heating was not well explored. Dehoff et.al [49] also observed similar microstructures at the interface. In addition they performed OIM in conjunction with TEM and observed that the grain at the interface were equiaxed with low dislocation density corresponding to a dynamic recrystallized structure. However the temperature rise during UAM was measured using thermocouples and showed only a moderate 120-150°C rise at the interface [62]. Since this is less than $0.5T_m$ the role of adiabatic heating was looked into. Adiabatic heating is known to occur during high strain rate deformation of materials and is associated with the fact that the heat generated during plastic deformation of the material is not able to escape out due to the high strain rate of the process [63].

Schick et.al estimated the strain rate that occurs during VHP UAM using the Zener Holloman parameter to be close to 10^5 [62, 64]. Hence there may be some relation between the microstructure that occurs as a result of VHP UAM and to the microstructures, which occur as a result of high strain rate deformation. Calculations of temperature rise due to adiabatic heating by Sriraman et.al in copper [57] showed that temperatures in excess of $0.5T_m$ for copper occurred during VHP UAM processing. Extensive TEM investigations of copper subjected to severe plastic deformation and high strain rate deformation also shows grain morphologies similar the interfaces obtained after VHP UAM [65]. On comparing the misorientation distribution in copper fabricated using VHP UAM and that of copper obtained after high strain rate deformation [66] we see a similarity with both the microstructures showing an increase in the high angle grain boundaries. Aluminum 3003 alloys after fabrication using VHP UAM also indicate similar microstructural features with an increase in the high angle grain boundaries at the interface [67]. These suggest that the bonding occurred as a result of dynamic recrystallization driven by the adiabatic heating.

It is pertinent to mention that the temperature rise in metals is sensitive to strain rate and the total strain in the samples [68] and hence an accurate measurement of the strain and strain rate is necessary. However experimental measurement of strain and hence the strain rate has not been carried out till date due to difficulties in measurements under ultrasonic frequencies.

The accumulative effects of bond formation have also been studied since it was shown that the bottom layers which went through a lot more thermal and mechanical cycles [67]. On examination using EBSD it was reported that the bottom region had a higher fraction of high angle grain boundaries compared to the top regions of the builds [67]. The increase in the fraction high angle grain boundary had been hypothesized to occur as a result of static recrystallization process. Static recrystallization at the bottom layers would have led to a change in the texture [69], which the authors did not observe. Al-6061 being an age hardenable alloy has higher yield strength and hence would be expected to show different deformation behavior. The microstructure evolution in Al 6061 during UAM and the effect of the normal force on microstructure and texture was examined, in the low power regime [69] and also in the very high power regime [61]. In both the cases a decrease in the LABs at the interface was reported albeit at different levels. Kittichai [70] had carried out systematic evaluations of the effect of the process parameters on the interface microstructures in Al 3003. He correlated the effect of process parameters on the hardness and quantitatively analyzed the microstructure and texture at the VHP UAM interfaces. The average hardness at the interface showed softening with the increase in the ultrasonic power and this was attributed to recrystallization at the interfaces made using VHP UAM. It was reported that the sample fabricated with the lowest power showed is closest to the as received foil for all the conditions that were considered. The deformed structure transforms progressively to a dynamically recovered structure and then to a dynamically recrystallized structure with the increase in the ultrasonic power similar

to that previously observed. Thus the microstructure evolution in various Al alloys and electrolytic tough pitch Cu shows similar microstructure evolution. Adiabatic heating leading to dynamic recrystallization primarily drives the microstructure evolution. Mechanical testing of Al-6061 fabricated in the T-6 temper showed that artificial aging after processing was necessary to bring the strength to close to the base metal. This may be due to the localized dissolution of the precipitates during the adiabatic heating but however this remains unsolved in the literature and would be worth looking into.

2.6.3. Micro texture studies at the interface:

In order to understand the bond formation mechanism it is very important to look at the micro textures at the interface. Textures leave a strong tell-tale signs of the physical processes that accompany the bond formation process since the orientation changes occurring during the deformation and recrystallization processes are not random [69]. The deformed metal acquires a distinct texture depending on the slip system on which the deformation occurs and also the extent to which the metal is strained [71]. Consequently different metals have different textures. During recrystallization since nucleation occurs on specific features in the microstructure, recrystallization results in a distinct texture [71]. Thus by studying the micro textures at the interface and comparing it with the as received material it is possible to rationalize the bonding mechanism that occurs during VHP UAM. Such tools have been used widely to understand and rationalize the bonding mechanisms occurring during friction stir welding [72] and for accumulative roll bonding [73, 74]. With relation to UAM and VHP UAM studies have been focused on only Al alloys where extensive and quantitative analyses of textures have been performed at UAM interfaces. The study by E.Mariani and E.Ghassemieh used recrystallized Al 6061 for their study [69]. FCC metals exhibit a strong cube $\{100\} \langle 100 \rangle$ texture in their recrystallized state [71]. Characterization after processing

showed that the initial recrystallization texture (i.e. Cube texture) starts to weaken at the interface with the increase in the normal load at the interface [70]. However since the power levels correspond to the lower power regions of the spectrum the final texture exhibited a fiber texture and not any distinct components. Fuji et.al [67] used VHP UAM to fabricate builds using rolled Al 3003 tapes and observed that the rolling components at the interface were replaced with a prominent shear texture $\{111\} \langle 110 \rangle$ at the interface. The formation of this shear texture was associated to be as a result of the severe shear deformation of the asperities at the interface. Similar shear textures were observed during VHP UAM of rolled Al 6061 [61]. Kittichai also reported similar textures and showed that the shear component $\{111\} \langle 110 \rangle$ fiber texture gets weaker as the input power increases. This was attributed to the presence of particles at the interface, which caused the textures at the interface to get random. The textures obtained during VHP UAM are significantly different from those obtained from accumulative roll bonding another solid state joining process which employs severe shear deformation at the interfaces to join thin foils. On accumulative roll bonding of Al-3003 Roy et.al obtained a combination of copper texture and a Dillamore texture at the interface as against a shear texture [75, 76].

It was shown that the strength of the copper and Dillamore component depended on the extent of deformation that occurred at the interface during accumulative roll bonding. No satisfactory explanation has been reported to rationalize the differences in texture evolution since both the processes involve severe shear deformation at the interfaces. It is well known that post weld heat treatment of solid state welds promotes more interatomic diffusion across the interface thus improving the strength along the 'z' direction [39]. Hence characterization of the microstructure and texture of post weld heat-treated builds made using VHP UAM have also been performed to understand the processes that occur during post weld heat treatment. David Schick documented that

there was no significant grain growth at the interface during post weld heat treatment of VHP UAM builds though no detailed microstructure analysis was performed [64]. Kittichai carried out systematic experiments under in situ conditions using a neutron beam line facility and observed that the shear textures at the interfaces are stable and that may be the reason for the sluggish grain growth at the interfaces. However no rationale for the sluggish grain growth at the interface was provided in the study [70].

2.6.4. Dissimilar metal joining using VHP UAM:

Since VHP UAM is a low temperature process without any significant time for diffusion it is a potential technique for fabricating dissimilar materials [39] [77] [78, 79]. An extensive feasibility study was performed in the 60's to fabricate heat resistant refractory metals using ultrasonic welding [77]. They reported extensive cracking at the interfaces of the dissimilar metals and attributed that behavior to the high cycle fatigue like conditions set up due to the ultrasonic oscillations at the interface. They also observed an increase in the cracking tendency when the vibration amplitude increases. They showed back in 1961 that only soft metals could be satisfactorily joined using ultrasonic welding a problem that exists even today!

A feasibility study to fabricate various combinations of dissimilar metals was performed by J.O.Obielodan et.al. [78, 79]. It was reported that Al-1100 interlayers were found to bond well with most of the materials. It was also reported that all Al alloys bonded well with the hard materials whereas none of the other FCC materials such as Copper, Nickel and Silver were reported to form a satisfactory bond. It is also pertinent to mention that the power used for the above study was in the lower power range. Another significant observation was that when hard to join refractory materials were joined with softer Al, the bulk of the deformation was concentrated in the Al. Among all the Al alloys used Al 3003 and Al 1100 bonded well when used in dissimilar

combinations but Al 6061 bonded only moderately. It is also worth mentioning that this conclusion was made just based on LWD measurements using an optical microscope and no in depth analysis was made in this case.

Troug performed detailed mechanical testing for joining dissimilar copper and aluminum [39]. Using push-pin testing Troug observed that by modifying the surface roughness of the foil he was able to improve the mechanical strength of the builds. It was hypothesized that the increased surface roughness increased the amount of mechanical interlocks at the interface and this resulted in improved strength. However no analysis using multi scale characterization was carried out to validate this observation.

In addition that effect of post weld heat treatment on the mechanical properties was also evaluated. Al-Cu welds showed improved the mechanical strength at the interface due to the formation of a thin layer of intermetallic at the interface. This thin intermetallic layer constricts the deformation at the interface leading to improved mechanical properties. XRD was performed at the interfaces and it was shown that the failure occurred at the metal adjacent to the intermetallic. Based on the literature it is clear that no extensive characterization has been performed on dissimilar metal welds made using ultrasonic additive manufacturing. Thus the goal of this work is to fabricate various dissimilar metal combinations and examine them using multi scale characterization techniques to study and gain a fundamental understanding of the bond formation mechanisms.

Chapter-3

Problem statement and research objectives

3.1. Problem Statement:

There is a drive to fabricate builds using dissimilar metals in the solid state using harder materials such as steel, titanium etc. Due to the inherent difficulty in deforming harder materials at room temperature, there is a need to use softer materials as interlayers. However it is not clear if a solid state bond could be achieved when using materials differing in hardness. Thus to effectively understand the above mentioned phenomena a fundamental understanding of the microstructure evolution and bond formation mechanism becomes important. The bond formation in dissimilar metals may be significantly different compared to that of the similar metals due to different amounts of deformation that the dissimilar metal combinations may undergo. Looking at the literature where dissimilar combinations have been joined using pressure-welding techniques at room temperatures, the initiation of a solid-state bond is thought of in terms of an energy barrier, which needs to be overcome [41]. This could be the energy required to re-orient the atoms at the surface of the metal [3], remove the oxide [52] or initiate recrystallization [55]. Since plastic deformation is of primary importance in processes where the interface temperature does not increase to allow for interatomic diffusion, the hardness of the material would be expected to play a significant role. This is indeed true with adhesion of metals. For instance hard metals like Ti, Cd etc. needs excess threshold deformation to initiate bonding compared to softer metals such as Al, Ni, Cu [80, 81]. Since the deformation of the underlying metals is primary for the disintegration of the oxide layers while welding dissimilar metals it would be interesting to observe how the bonding occurred due to the difference in the threshold deformation required to initiate the bonding.

3.2. Research Objectives:

The questions that would be answered during the course of this research activity are

- i. While welding dissimilar metals with a hard and soft combination should both the metals undergo deformation for a bond to form
- ii. Does the microstructure at the interface developed driven by plastic deformation alone or is heating an essential factor for the formation of bonding?
- iii. What happens to the oxygen at the interface after the oxide layer dis integrates during VHP UAM?

To gain an overall understanding of the bond formation dissimilar metals with different

1. Recrystallization temperatures
2. Hardness

were used to fabricate dissimilar metal welds using 9kW ultrasonic additive manufacturing. The following combinations will be explored

1. Steel to aluminum 6061
2. Aluminum 1100 to CP titanium
3. Steel to tantalum

Apart from having different hardness and recrystallization temperatures the metal combinations are relevant for industrial applications.

Chapter-4

Experimental details

4.1. Breakdown of the proposed tasks:

The Al-Ti and Al-Steel configurations proposed above would be fabricated using the 9kW UAM machine located at The Ohio State University in collaboration with the Professor Dapino's research group while Fe-Ta configuration would be performed at the 9kW machine at Fabrisonic. Multi scale characterization and hardness measurements would be performed on all the three combinations. However the mechanical testing would be performed only on combinations 2 and 3. The reason for this is primarily from the application perspective. The combination 1 would find applications only as clads and hence the mechanical properties need not be extensively investigated. However combinations 2 and 3 may find applications in the load bearing areas in aerospace applications, which makes mechanical property evaluations important. A brief description of the techniques that will be used for investigations are provided

Cross sectional imaging:

Cross sections of welds are normally investigated using multi scale characterization techniques with different length scales. In this work microstructures are investigated in the

- i. **Macro scale:** Optical microscopy
- ii. **Micro scale:** Scanning electron microscopy and Electron Backscattered diffraction
- iii. **Nano scale:** Transmission Electron Microscopy and Electron diffraction
- iv. **Atomic scale:** Atom probe tomography

The hardness measurements at the interface were performed using load displacement sensing techniques.

4.2. Optical microscopy:

The sample being opaque to light it is illuminated by reflected light. The product of the objective and the eyepiece of a particular combination is the magnification. Optical microscopy is typically used to reveal the grains at by etching the sample, however in this work etching was not used since optical microscopy cannot resolve the fine-grained structure at the interface. The resolution of any microscopy technique used is dependent on the wavelength of the imaging medium and the numerical aperture. The resolution is given by

$$d = \frac{\lambda}{2NA} \text{-----}(4)$$

Assuming the wavelength of light to be ~550 nm and a NA of 0.85 for air the resolution of the optical microscope is ~ 350nm. It should be noted that this is the maximum theoretical resolution of the microscope and in practice the obtained resolution is much lower than this due to the various aberrations in the lens. From a UAM perspective, optical microscopy is predominantly used for observing voids along the interface and is a widely used technique to quantify the linear weld density in UAM. As described previously in section 2.1, linear weld density is a destructive technique that involves sectioning and polishing the specimen and quantifying the extent of bonding which is a useful method for understanding if the parameters used are reasonable. It however has to be stressed that linear weld density cannot be used as tool to correlate the process parameters to the final mechanical properties of the builds.

4.3. Scanning electron microscopy and electron dispersive spectroscopy:

The scanning electron microscope uses electrons, which have a much higher energy than the visible light used and consequently lower wavelengths. Consequently the resolutions that can be obtained using a scanning electron microscope are higher than those obtained using a regular optical microscope. The sharpness and feature visibility of a SEM is dependent on

- i. Electron probe size
- ii. Electron probe current
- iii. The electron probe convergence angle
- iv. Electron beam accelerating voltage

The optimum conditions for imaging are dependent on the material being investigated. Ideally for the highest resolution the d_p must be as small as possible while at the same time containing sufficient current to produce sufficient contrast. The mechanism of contrast formation in SEM can arise due to (i) Topography differences (ii) Composition differences. This contrast arising is often used in UAM to predict the flow lines to study the nature of the oxide dispersion in the bonding materials [58, 59, 82]. In dissimilar metals the difference in contrast arising from the composition can be used to understand how the material flow occurs. In addition, most SEM's are equipped with an Energy dispersive X Ray spectrometer, which has the ability to measure spatial variations in composition thus greatly enhancing our understanding of the process. However the interaction volume of the electron beam limits the spatial resolution with the specimen. It is to necessary to understand that the electron beam interacts with a finite volume of the specimen which is dependent on the

- i. Beam energy
- ii. Atomic number
- iii. And surface tilt

For a more detailed effect of the influence of these parameters interested readers are directed to the text by Goldstein et.al. [83]. Electron beam interaction volume effects are normally simulated using Monte Carlo simulations. However this can be estimated using a relation due to Kanaya and Okayama [84]

$$R_{KO}(\mu m) = \frac{0.0276A}{Z^{0.89}\rho} E_0^{1.67} \text{ -----(5)}$$

Where Z is the atomic number, ρ is the density, E is the beam energy in (keV) and A is the atomic weight (g/mole). This can be used to identify the interaction volume and hence better quantify the line scans. The data from the line scans often lead to erroneous interpretations of the process if the interaction volume is not factored in as shown in [85]. While performing line scans using energy dispersive spectroscopy techniques it is always beneficial to have the distance between points greater than the R_{KO} for proper interpretation of data.

4.4. OIM using Electron backscatter diffraction:

As stated in the previous section, to understand the bonding mechanism it becomes important to understand the microstructure and texture at the interface. One of the easiest techniques to probe the Micro texture at the interface is EBSD. The reason for using this technique is two fold. The main reason is the relative ease with which the data on texture can be obtained. The other reason is that it is possible to measure the misorientation distribution inside each grain and the orientation spread that occurs on each grain making it possible to understand the mechanisms of plastic deformation and recrystallization at the interface. It is possible to observe a crystallographic contrast in a well polished specimen in a SEM when imaged using back scatter diffraction. The observed contrast is termed as channeling contrast. This arises primarily due to the fact that each crystallographic plane has a different number of atoms. This results in a difference in the backscatter yield. For instance a low index plane has relatively large interplanar spacing and consequently the backscatter yield is low as against a high index plane. However this does give qualitative information on the grain orientation but no quantitative information is obtained.

EBSD is an automatic crystal orientation mapping technique that is capable of obtaining several thousands of orientations every hour thus giving us a relation between the microstructure,

grain to grain misorientation, extent of deformation and the processing. EBSD has been widely used to understand deformation and recrystallization phenomena [71, 86]. The technique basically consists of tilting a well polished sample to 70° angle and illuminating the sample using an electron beam. The specimen is tilted at 70° to maximize the yield of the signal arising from the diffracted electrons. The resulting diffraction pattern is then automatically indexed and analyzed. The patterns are detected using a phosphor screen and a schematic is shown in the figure.

EBSD technique uses an automated algorithm to index Kikuchi diffraction patterns. The Kikuchi diffraction patterns are obtained as a result of electron diffraction and channeling. The result is it forms a cone with a very large apex angle with a semi angle of $(90^\circ - \theta_B)$ where is θ_B is the Bragg angle. Due to the small wavelengths of the electron sources the Bragg angle are small and typically less than 2° . Due to the diffraction from both the front and back of the atomic planes we observe two cones per plane. Due to the high apex angle the cones when intersected by the phosphor screen are displayed as lines. The separation distance between the lines is equal to the Bragg angle. From the discussion above it is clear that only the low loss backscatter electrons contribute to the diffraction pattern formation and from Monte Carlo simulations it has been well established that the low loss backscattered electrons arise from very near the surface. The resolution however is dependent on the atomic number and the accelerating voltage and probe diameter. For instance one study operating a FEG source at 2kV observed spatial resolutions of 30nm in Al and 10 nm in a brass sample [87]. The angular accuracy of the technique is $0.5\text{-}1^\circ$ between adjacent points.

In the case of UAM use of EBSD has been extensive to understand the grain size and texture at the interface as mentioned previously and was one of the technique that was used to rationalize the bond formation mechanism in similar materials.

4.5. Transmission electron microscopy:

In a transmission electron microscope (TEM), the electrons that are transmitted through a thin sample (~50-80nm thick) form the image. There are two types of contrast that can be obtained using a TEM viz.

1. Mass contrast
2. Diffraction contrast

Mass contrast arises from difference in the atomic numbers of the scattering elements or due to the difference in thickness in the samples. On the other hand the diffraction contrast arises from the diffraction of the electron beam by the lattice. To understand the theory of image formation in a TEM one must consider the electron beam as a wave. Normally a fraction of the incoming electrons strike the sample and diffract while the remained passes right through the specimen. These electrons that do not diffract constitute the direct beam or the un-diffracted beam. The remainder of the electrons diffracts through a number of crystallographic planes and they constitute the diffracted beam.

4.6. Hardness measurements using load displacement sensing:

Previously researchers have always used micro hardness as a tool to measure the hardening or softening behavior of the interfaces made using VHP UAM [57, 70]. The interface formed after VHP UAM is of the order of the 10-15 microns but for the test conditions used in the literature the length of the diagonal is close to 21 microns that is larger than the interaction zone at the interface. Hence using micro hardness may lead to averaging the bulk properties along with the interface properties. To avoid the problems mentioned above hardness measurement using load displacement sensing has been used in this research to map out the hardness distribution at the interface to measure the hardness values. Nano indentation has been used as an effective tool to probe the

interfaces in samples made using accumulative roll bonding and some authors were able to detect intermetallic formation during post weld heat treatment of the ARB builds made with Al and Ti. However the use of nano indentation to understand and rationalize the deformation and recrystallization phenomena in the VHP UAM interfaces have been somewhat limited. Load displacement sensing techniques have been used in the past to understand the nature of fiber embedment in VHP UAM builds. The authors observed increased hardness at the regions near the fibers and attributed the rise to Al matrix deforming around the fibers [88].

The enhanced spatial resolution is obtained due to the low depth levels that the nano indenter can go to. In this study a depth of 500 nm was used giving a spatial resolution of $\sim 10\mu\text{m}$. This high spatial resolution helps in probing the interface. Hardness measurements using micro hardness rely on calculating the hardness by physically measuring the lengths of the indentation made by the indenter. Nano indentation is different from a traditional micro hardness testing in that in nano indentation the size of the indent is not measured but rather calculated using principles from contact mechanics and hence is more accurate.

Mechanical testing:

Mechanical testing of bonded layers is extremely important and that can greatly influence the development of ultrasonic additive manufactured parts and its expansion in existing and new fields. The overall strength of a laminated structure depends on the bond strength between the layers. However with the peel tests and tensile tests it is not possible to evaluate the bond strength since it is difficult to control the location where the samples are expected to fail. These methods also need welded foils and an overall height of 1.9 cm that is approximately 130 foils. Hence this necessitates the need for alternate testing methods. It has been reported that the pushpin testing has been used successfully to estimate bond strengths at the interface. A detailed description of the

technique is described elsewhere {Zhang, 2009 #50}. Hence bond strengths of all the dissimilar joints were evaluated using the pushpin testing performed using the Gleeble 3800D thermo mechanical simulator. After testing the fracture surfaces were analyzed using SEM and EDS to determine the fracture morphology and analyze the exact location of the failure. By performing EDS it is possible to understand if metallic bonding had occurred since it is hypothesized that metallic bonding would lead to a failure at the foils rather than at the interface.

Chapter-5

Multi scale characterization of Al-Steel (FCC-BCC) dissimilar metal combination

5.1. Introduction:

In this chapter attempts were made to fabricate 4130 steel to Al-6061. The combination was chosen due to the industrial relevance of Al and Steel combinations which are widely used in the automotive and the aerospace sector to effect light weighting of parts [115].

While resistance spot-welding is widely adopted for joining steels in the automotive industry, frequent electrode wear and tool replacement limits its use in aluminum and dissimilar joints [115]. The issue of liquid metal embrittlement during resistance spot welding can also degrade the mechanical strength of these joints. Similarly, various intermetallic phases can form during fusion welding of Al and Steel, resulting in brittle failures at these surfaces. Hence solid-state welding techniques that involve no macroscopic rise in temperature are necessary to fabricate high strength welds.

Solid state welding processes, can facilitate the joining of these materials without property degradation due to thermal effects [116]. Though friction stir welding, another solid state welding process has been widely used to fabricate dissimilar metals, its use in Al-Steel joints is challenging due to the different deformation characteristics of both Al and Steel [13]. Apart from that, intermetallic formation has also been reported in these welds, degrading the mechanical properties at the interface [15, 114]. There are several other high strain rate processes such as magnetic pulse welding and magnetic seam welding where it is claimed that there is no interfacial reaction during welding. There is however literature suggesting otherwise [117]. Hence solid-state welding techniques that involve no macroscopic rise in temperature are necessary to fabricate such welds.

Solid-state welding techniques, such as ultrasonic welding, can facilitate dissimilar welding without degradation of mechanical properties. It shows promise in the creating layered metallic structures, with similar and dissimilar material combinations. The macroscopic temperature rise at the interface has been measured to be less than 200°C for welding Al [67]. However the actual temperature that the interface experiences due to adiabatic heating effects from severe plastic deformation is debated in the literature [93].

Limited feasibility studies have been performed on Al-Steel using ultrasonic spot welding. One study where Al-Steel was joined using ultrasonic welding showed that the process involves using three times more power than what had to be used to fabricate Al-Al similar welds [115]. Under higher weld power, the material is subjected to increased plastic deformation, which is important for weld quality [118]. The strength levels of solid state welds increase with deformation and reach a plateau, governed by the strength of the weaker metal [41]. The aim of this work is to explore the feasibility of joining 4130 steel and Al-6061 using UAM and formulate a bond formation mechanism for dissimilar metal welds.

5.2. Experimental Procedure:

5.2.1. Sample Manufacturing:

Joining of Al-Steel combinations was investigated using a 9 kW UAM machine at The Ohio State University. The substrate (steel) used was machined flat prior to welding to remove oxide scales from the surface and ensure flatness. Welds onto steel utilized an annealed 4130 baseplate. For each case, the first foil layer in contact with the baseplate constituted a dissimilar weld. Subsequent welds, for the case of aluminum onto steel were similar Al-Al joints. The weld parameters for the Al onto steel joining were 5000 N normal force, 23 μm weld amplitude, and a welding speed of 100"/minute, all conducted on a substrate preheated to 300°F. The similar Al-

Al bonds were performed using a 5000 N normal force, 32.5 μm weld amplitude, and 200"/minute weld speed.

5.2.2. Joint Characterization:

After fabrication mechanical testing of the joints was performed on the Al-steel builds using pushpin testing. Pushpin testing is a testing method introduced by Zhang et al. to evaluate the mechanical performance of the laminated structures [110]. The advantage of pushpin testing over other tests such as a peel test is due to the fact that the failure always occurs within the weld, thus providing a measure of weld strength. Peel tests, for example, can fail in the foil material itself, therefore limiting the information gained from the test [119]. Pushpin tests were performed on 10 layer samples using a Gleeble 3800 thermo-mechanical test frame at room temperature. During the test, a pin is pressed through the sample at 0.2 mm s^{-1} with the load and displacement being recorded. The maximum force of the push out as well as the area under the curve, are the two metrics used to analyze the results of the test. More information on the test can be found in [110].

After mechanical testing multi scale characterization was performed to rationalize the differences in mechanical strengths. Fractography was performed on the samples to investigate the fractured regions. Analysis was performed using optical microscopy, scanning electron microscopy (SEM), and electron backscattered diffraction (EBSD) to investigate the effects of the processing. To facilitate the microstructural analysis, samples were sectioned using a low speed diamond saw and cold mounted in epoxy to prevent any changes to the dislocation substructure introduced during the UAM process. Following mounting, the samples were polished using SiC papers with a water lubricant, followed by polishing with in a diamond suspension, and a final polish using 0.05 μm colloidal silica solution. Optical microscopy was

performed using a Leica optical microscope. SEM and EBSD were performed on a JEOL 6500S electron microscope with an accelerating voltage of 20 kV and a probe current of 4 nA. In addition, energy dispersive spectroscopy (EDS) was performed to determine material compositions. To minimize the interaction volume, EDS was performed at 10 kV and 2 nA.

After characterization using SEM samples for atom probe tomography were prepared using FIB technique. Local Electron Atom Probe tomography was performed on a CAMECA LEAP 4000 in the laser atom probe mode. The analysis was performed on a sample that had been cryogenically cooled down to 40K. The sample was analyzed using the Laser atom probe. The laser energy of 30pJ and a pulsing rate of 250 KHz were used for data collection. A total 32 million ions were analyzed. Visualization and data analysis was performed using IVAS 3.6.8, commercially available software from CAMECA. The tip was reconstructed using the tip profile mode. The quantitative analysis at the interface was performed using a proximity histogram or a Proxigram, which results in a composition profile from the surface of the particle/precipitate (in this case oxide) to the matrix.

5.3. Results and discussions:

The samples were characterized using optical microscopy and scanning electron microscopy to check for voids along the interfaces. The results are shown in figure 5.1(a) (b). Both show a continuous bond line meaning that the welds fabricated has close to a 100% linear weld density. Following preliminary characterization mechanical tests were done on the builds using push pin tests. The results are shown in figure 5.2(a). The results show that the builds failed by a shear deformation failure rather than delamination. This mode of failure is evidence for the formation of a solid state bond. The EDS measurements of the builds showed transfer of Al and Fe across the interface. A true solid state bond between Al and steel would mean that the

bond strength should exceed that of Al and Al. Hence to confirm if we had a true metallurgical bond Al-6061-Al-6061 welds were tested using exactly the same technique. The results from the push pin tests are shown in figure 5.2(b). The Al-Steel builds exhibited an average maximum load of 2.85 kN, and an area under the curve, or integral, of 5.15 kN-mm. Al-Al builds resulted in an average maximum push out force of 1.67 kN and an integral of 1.53 kN-mm. The data shows that the Al-Steel weld did absorb more energy than the Al-Al welds. This suggests that the bonding between Al-Steel is stronger than the bond in the Al-Al welds. This is indicative of metallurgical bonding occurring in the case of Al-Steel.

As pointed out in the previous chapters a true solid state weld forms by oxide removal and asperity collapse. In order to rationalize this multiscale characterization was performed at the interfaces. To understand if deformation occurs at the interfaces electron backscattered diffraction was performed. For a brief description of the capabilities of EBSD interested readers are directed to [100]. The results from electron backscatter diffraction are shown in figure 5.4. Figure 5.4(a) shows the results of EBSD performed across the first 3 layers of Al-6061 deposited on the 4130 steel substrate. Note the dark line along the interface. This dark black region is a consequence of the shadowing effects at the interface. The reason for the shadowing arises from the difference in the polishing rates between Al and steel. Steel polishes slower than Al resulting in the formation of a step, which causes the observed shadowing in the EBSD.

On examining the interfaces closer it is clear that in this case also the deformation is concentrated in the Al side of the interface. The steel side of the interface does not deform. Plastic deformation is always associated with the change in crystal orientation resulting in a distinct crystallographic texture. By analyzing the texture it is possible to understand microstructure evolution. Here on analysis of the micro texture at the interface of the welds the

texture shows the presence of a rotated cube texture $\{100\}\langle 110\rangle$ at the interface. This means that the $\{100\}$ plane is parallel to the normal direction and the $\langle 110\rangle$ direction is aligned along the vibration direction. The texture obtained after welding Al-6061-to-Al-6061 similar metal combination was analyzed and this shown a very similar rotated cube texture. Figure 5.5 (a) and (b) show the texture obtained after welding Al-6061 to steel and Al-Al welds respectively. Note that although the texture is identical the texture strengths are different. The interface where the Al-Steel weld is present shows much stronger texture strength compared to the similar Al-Al microstructure. This is direct evidence of the deformation concentrating in the Al side of the interface leading to enhanced bonding at the interface. However for bonding to occur it is necessary for oxide removal as well. In order to investigate the oxide removal step atom probe tomography was performed at the interfaces.

Figure 5.6 shows the regions where samples for APT analysis were obtained and the final tip used for analysis. From the SEM micrograph shown in figure 5.6 it is clear that the region analyzed is bonded and the interface from where sample extractions were done is marked using red arrows. The reconstructed tips showing the spatial distribution of each element is shown in figure-5.7. Figure 5.7(a) and figure 5.7(b) show the spatial distribution of Al and Fe in the tip. While interpreting figure 5.7(a) where we see Al atoms inside the steel section of the interface, it is important to keep in mind that Al has an isotope at 27 and that would essentially have the same mass to charge ratio as that of a Fe^{2+} (54) and hence would get ranged as an Al atom. Figure 5.7(d) through (f) shows the spatial variation of the oxygen. Figures 5.7(c) through (f) shows the variation of O, Mg and C atoms respectively. The figure clearly shows Oxygen atoms present at the interface of bonded regions. The atom probe mass to charge spectrum is also presented in Figure 5.8. The spectrum clearly indicates a peak at 16 and 32, which correspond to O^+ and O_2^+

respectively. These peaks indicate the possibility of oxygen being forced into the system due to the excessive deformation.

Numerous studies on mechanical alloying and ball milling of oxide dispersion strengthened materials seem to indicate the possibility of oxygen segregating to defect structures and grain boundaries and extensive atom probe analysis seemed to indicate that oxygen rich nano clusters form with diameters of 2-4 nm [120-122]. Miller et.al reported that nano clusters rich in Y, Ti and oxygen form in oxide dispersion steels [120, 121, 123, 124]. Atom probe tomography analysis of the composition of such oxides showed that the oxygen stoichiometry did not correspond to oxides. The nano cluster formation was attributed to the oxide decomposition and oxygen segregation to the vacancies [125]. First principle calculations also suggest that the vacancies and oxygen atom interactions showed the possibility of oxygen segregating to preexisting vacancies in iron [126]. In the case of UAM since the steel did not undergo deformation it is improbable that the steel is supersaturated in oxygen. Hence the oxygen should either be oxides or dissolved in Al. However in the case of Al the solid solubility of oxygen is near 0 wt %. The composition analysis at the interface showed oxygen super saturation of upto 20 at %. This increase in oxygen could only be attributed to solubility of oxygen in the Al matrix since the oxygen concentration is too lean to be an oxide.

Figure 5.9(a) shows a 6 at% oxygen iso surface. This was chosen since this was the maximum oxygen concentration for which the iso surface marked a continuous film of oxygen at the interface. Proxigram analysis was performed on several locations and the locations where the maximum and minimum oxygen concentrations were detected are shown in figure 5.9(b) and (c). Figure 5.9(b) shows the oxygen and magnesium concentrations corresponding to the region marked with a red arrow. This corresponds to the location of the interface where the maximum

concentration of oxygen was detected at the interface. This region was detected by performing proxigram analysis on various locations at the interface. A total of 15 proxigram analyses were performed on the interface. The maximum oxygen concentration at the interface was to 20 atom%. The corresponding Mg concentration was 5 atom%. The Mg concentration was constant throughout the length of the interface with only minor fluctuations (typically less than 2 atom percent). This enrichment of Mg at the interface has been previously documented in friction stir welding of Al alloys and was hypothesized as Mg oxide. However Al_2O_3 is thermodynamically more stable than MgO. The rationale provided by the authors was that under low oxygen activity ($<10^{-34}$) MgO could form [127]. Another explanation for the Mg enrichment could be the formation of MgAl_3O_4 at the interface, which is thermodynamically possible. However in this case the oxygen concentrations measured is \sim less than 20 at% Al_2O_3 is expected to contain approximately 60 at% oxygen. Also the transformation from Al_2O_3 to the spinel involves a change in the crystal structure, which may not be possible in the UAM regime. The oxygen super saturation is also low to form any oxide at the interface. This suggests that the oxide decomposes and due to the extensive plastic deformation into metal and oxygen [128]. The oxygen atoms are then supersaturated probably at the defects and grain boundaries.

Though the oxygen solid solubility in Al is close to 0%, it has been shown that super saturation at grain boundaries can reduce the surface energy of grain boundaries and defects [129-131]. The reduction in free energy associated with the segregation of oxygen to the dislocations and grain boundaries can be described based on the Gibb's adsorption equation

$$d\gamma = -\Gamma d\mu_{\text{solute}} \text{-----}(1)$$

Where μ_{solute} is the chemical potential of the solute and Γ is the Gibbsian interfacial excess [130]. We can now rewrite the above equation in terms of solute concentration and the enthalpy of segregation as

$$\gamma = \gamma_o - \Gamma(RT \ln c + \Delta H_{\text{seg}}) \text{ -----}(2)$$

where c is the concentration of oxygen atoms and ΔH_{seg} is the enthalpy of segregation. This shows that the energy of the defect decreases if the solute has a positive enthalpy of mixing, in other words when the solute segregates to the defect. This can lead to two different interpretations

- i. Decrease in defect formation energy
- ii. Decrease in the energy of the solute atoms when segregating to the defects.

The implication of this would be that it is possible for a metastable equilibrium to exist for a large concentration of oxygen and large Gibbs interfacial excess values. By setting the value of γ to zero one can evaluate the critical interfacial excesses required for microstructural stability [132]. While it has been established that oxygen can enter into solid solution in Al if the grain boundary area or defect density is significant, the thermodynamics of the breakdown of the oxide is not clear and needs to be looked into and is beyond the scope of the current work.

5.4. Conclusions:

Steel and aluminum have been successfully fabricated using UAM. Multi scale characterization showed that deformation is concentrated on the softer Al side. This lack of deformation in steel is the main reason why further deposition of steel foils was not possible on the Al substrate. Texture analysis showed the retention of the strong deformation texture $\{100\}<110>$, which is very similar, to what was observed with Al-Ti, and in Al-Al similar welds. Mechanical testing showed that the bond strength of the Al-Steel side is higher than the

bond strength in Al-Al welds. The failure analysis of the builds indicates that localized regions exhibit metallurgical bonding despite the fact that plastic deformation occurs in only one metal similar to what was observed in Al-Ti welds. However the fracture mode predominantly is brittle.

Atom probe tomography investigations showed the presence of oxygen at the interface. The oxygen super saturation was close to 12 at%, which is insufficient to form an oxide. Hence it is concluded that the oxygen is supersaturated in the defect locations in the Al lattice due to the enhanced plastic deformation. A direct implication of oxygen dissolution would be the fact that the interfaces during post weld heat treatment does not show grain refinement at the interface. The consequence of this on mechanical properties of the builds needs to be investigated.

Chapter-6

Rationalization of bond formation mechanism in FCC-HCP dissimilar metal combination

6.1. Introduction:

From the previous chapter it has been established that a solid state bond can be obtained by extensive plastic deformation in one of the two metals. In this chapter the generality of the conclusions obtained from the previous chapter would be evaluated. To this effect attempts would be made to weld aluminum to titanium and evaluate the bonding between them. Al and Ti were chosen primarily for the difference in hardness. In the previous chapter it was concluded that a solid state bond could exist with deformation concentrated in the softer metal. If the conclusions are general a metallurgical bond should exist despite the fact that the deformation would concentrate primarily in Al. In addition to the above objective aluminum and titanium were chosen due to their industrial relevance. Solid state welds are necessary to fabricate Al-Ti welds due to the formation of intermetallic compounds at the interface during fusion welding [9]. In the past, UAM has been used to successfully join Al 3003 and CP Ti and post weld heat treatment techniques have been used to improve the mechanical strength of these bonds [79]. The effect of process parameters on the strength of Ti-Al composite structures has been evaluated using statistical analysis techniques such as analysis of variance (ANOVA) [104]. However Al and Ti have a significant difference in mechanical properties; Ti being the harder material and Al being the softer material. It is hypothesized that Al would deform extensively. However solid state welding literature suggests that deformation in both the metals is required to initiate the formation of a solid state bond through asperity collapse and dispersing the titanium oxide. Hence this warrants detailed multiscale characterization coupled with mechanical testing

to understand if a solid state bond could actually occur with deformation concentrated only on one material.

6.2. Experimental Procedure:

Bilayers of Al-1100 and CP-Ti both 0.005" thick were welded onto an Al-6061-T6 substrate. The builds were made using a Fabrisonic Sonic layer 4000 9 kW system equipped with subtractive milling capabilities located at The Ohio State University. The parameters used for fabrication were a weld force of 3500 N, weld speed of 25.4mm/sec, and vibration amplitude of 41.55 μm . During deposition, the substrate preheated to 93.3°C as this has been shown to enhance plastic flow, improving bonding. The process parameters were developed based on iterative weld trials, which are discussed in [6]. The parameters do not represent a globally optimal set; though provide viable welds using these materials. The samples were then sectioned for metallographic analysis along the plane of vibration of the sonotrode and mounted. During sectioning, care was taken to ensure adequate coolant flow to maintain interface microstructures. Samples were mounted in epoxy at room temperature and polished using emery paper down to 1200 grit followed by diamond polishing using 6, 3, and 1 micron diamond slurries. A final surface polish using a 0.05-micron colloidal silica suspension was done using a Buehler Vibromet for 4.5 hours to remove the deformation zone from previous polishing steps. Optical microscopy was performed in a Leica DM 750P microscope. EBSD was performed on a JEOL 6500 FEG Scanning Electron Microscope (SEM). The analysis used an accelerating voltage of 20 kV, probe current of 4.0 nA, step size of 0.5 micron, and working distance of 17 mm. Data analysis was done using EDAX TSL software.

Following multiscale characterization mechanical testing was performed using the pushpin test [110]. The fractured surfaces were investigated using scanning electron microscopy

and energy dispersive spectroscopy to study if metallurgical bonding did occur. Furthermore post processing was techniques were developed to improve the mechanical strengths. The strength of dissimilar metal welds made in the solid state has always been correlated to the thickness in the intermetallic layer; where an intermetallic layer with a thickness less than $1\text{-}5\mu\text{m}$ has shown to improve the bond strength. This could be attributed to the lowering of the total surface energy of the interface due to the formation of intermetallic layer at the interface [39]. Hence post weld heat treatments have shown significant enhancements of bond strengths at the interface by promoting a thin intermetallic layer at the interface. Hence for this work to promote intermetallic formation heat treatments were performed at 600°C for 1 hour. This was based on the friction welding literature where increased strengths were recorded after post weld heat treatment at this temperature and time [9, 12].

6.3. Results and Discussions:

6.3.1. Optical microscopy:

A schematic of the bilayer arrangement is shown in Figure 6.1 (a). In the bilayer arrangement, the Al-1100 foil is in contact with the Al substrate as illustrated in Figure 6.1 (b) and marked in the micrograph. Plastic flow is more evident on the top surface of the Ti layer where there are more crests and troughs, as shown in Figure 5.1 (b). As shown previously no intermetallic formation was observed as the interface [111]. This occurs due to the contact between the sonotrode and the top surface of the build leading to local “trough” and “crest” formations as shown. Al being the softer of the two materials flows around these contours and hence the interface experiences significant plastic flow. For the remaining sections in this paper, the Ti layer in contact with the sonotrode will be referred to as the sonotrode affected region and the opposite side will be referred to as the smooth surface. The effect of the deformation on the

crystallographic grain structure needs to be examined to gain a fundamental understanding of the bond formation mechanism. This was realized using EBSD. A detailed description of this technique and the various methods of analysis can be found elsewhere [100].

6.3.2. Electron Back Scatter Diffraction:

6.3.2.1. *Characterization of original foil microstructure:*

The microstructure of the original Al-1100 substrate, foils and the CP-Ti foils prior to fabrication were characterized using EBSD. This data will be used to understand how UAM altered the microstructure at the interface of the bonded zone. The microstructure is presented in Figure 6.2. Detailed texture analysis was performed to understand the interfacial phenomena occurring in the builds. Characterization of the Al-1100 foils revealed they were supplied in the cold rolled condition, while the Al 6061 substrate material was supplied in the T6 condition. The initial CP-Ti microstructure shows an equiaxed alpha microstructure. The initial grain sizes before UAM were 17.27 μm and 5.45 μm for the Al-1100 tape and the CP-Ti tape, respectively.

6.3.2.2. *Microstructure evolution at the interfaces:*

The data from the EBSD measurements were analyzed and is shown in Figure 5.3. Figure 5.3(a) shows the inverse pole figure (IPF) overlaid over the image quality index (IQI). The color coded key for the IPF shows the respective plane normal parallel to the build normal direction. The image quality index (IQI) provides qualitative information about the extent of deformation at the interfaces. Darker regions correspond to heavy deformation and brighter regions correspond to un-deformed or recrystallized regions. The sonotrode-affected regions appear dark in the IQI maps due to the heavy deformation caused by the sonotrode. The titanium side, which is not affected by the sonotrode, on the other hand shows excellent image quality due to the lack of plastic deformation.

It is well known that plastic deformation will lead to an increase in dislocation density contributing to an increase in misorientation within a grain [100]. To quantify this misorientation, the grain orientation spread (GOS) of the grains was analyzed which is shown in Figure 3(c). It has been reported in the literature that a GOS of $<3^\circ$ corresponds to a completely recrystallized structure [100]. The GOS shows very high misorientations close to 7° in the Al-1100 foils in the middle sections after the UAM processing. However the GOS of the Al-1100 at the interface is less than 3° indicating a recrystallized structure. Thus for all the Al-1100 layers we observe a deformed region sandwiched between the dynamically recrystallized regions as shown in the GOS map. However on analyzing the GOS in the CP-Ti it is observed that there is no appreciable deformation increase except near the sonotrode-affected regions.

6.3.2.3. *Misorientation and grain size distribution:*

In addition to the GOS, the average grain size and misorientation at each layer was analyzed and the data is presented in Tables 1 through 4. The increase in average misorientation in layer-3 is due to the decrease in the low angle grain boundaries (LABS), which could be an effect of dynamic recrystallization [105]. Previous work on Al-3003 alloys showed that the fraction of HAB's in the bottom layers is higher than the top layers. Experiments where builds were fabricated using embedded thermocouples showed that when the bonding is incomplete in the $(n-1)^{\text{th}}$ layer, then on deposition of the n^{th} layer the $(n-1)^{\text{th}}$ layer experiences a spontaneous rise in temperature [90]. This temperature rise is due to the adiabatic heating at the interfaces due to the high strain rate deformation of the tapes at locations where bonding is incomplete. This rise in temperature results in an increase in the fraction of high angle grain boundaries (HAB's) in the $(n-1)^{\text{th}}$ layer and has been observed in Al-3003 [67]. However we don't observe such changes in the fraction of HAB's between the $n-1^{\text{th}}$ and the n^{th} Al-1100 layer. This could be

interpreted as complete bonding between the Al-1100-CP-Ti and consequently no temperature rise resulting from the relative motion of the foils. The reason for the increased HAB fraction in layer-3 could be attributed to the additional deformation that the layer-3 underwent. The surface of the Ti in the previous bilayer was roughened due to the pressure created by the sonotrode and had significant surface roughness. Al while flowing around these rough contours had to undergo enhanced plastic deformation due to the roughness of the previous Ti foil that one can see in the figure-3. This enhanced plastic deformation could have caused a rise in the high angle grain boundary in the Al-1100 in layer 3.

6.3.2.4. *On the evolution of micro texture at the interface:*

To analyze the nature of the deformation and dynamic recrystallization process, the crystallographic texture was analyzed. For cubic crystals, the texture is represented by $\{hkl\}\langle uvw \rangle$ where $\{hkl\}$ represent the plane parallel to the normal direction of the build and the $\langle uvw \rangle$ represents the crystal direction parallel to the direction of vibration of the build. The crystallographic texture of three layers of Al-1100 is presented in the form of a pole figure in figure 6.4. The rolling texture present in the original aluminum foils changed to the rotated cube texture where $\{100\} \parallel \text{ND}$ and $\langle 110 \rangle \parallel \text{RD}$. This is the most dominant component at the interface of all these three layers. However there is distinct spread in the orientation in layer-3 as shown in figure 6.4(c). This spread indicates the possibility of developing other texture components during the process. Hence the distribution of various orientations is plotted on the image quality map in figure 3(b). From the map it is clear that apart from the rotated cube component which is the major component present, other components such as copper $\{112\} \langle 111 \rangle$ and Dillamore $\{4\ 4\ 11\} \langle 11\ 11\ 8 \rangle$ were also present at the interfaces. However, these were concentrated only in the region where the Al-1100 came in contact with the relatively smooth surface of the CP-Ti.

There is large spread in the orientation where the Al that flowed around the hard Ti asperities. This is indeed a well-known effect where hard particles lead to the development of random orientations at the interface [112].

The copper component is also observed during plane strain rolling of Al alloys to heavy deformation and also during accumulative roll bonding of various Al alloys [74], [113]. The strength of the copper texture has been noticed to increase with the number of rolling passes during accumulative roll bonding (ARB), corresponding to an increase in deformation. Apart from the copper texture, the other common texture that has been identified with the accumulative roll bonded Al is the Dillamore texture $\langle 4\ 4\ 11 \rangle \langle 11\ 11\ 8 \rangle$ which is just 8° from the copper texture [74]. There are studies that indicate the possibility of forming a strong rotated cube texture $\{001\} \langle 110 \rangle$ type texture at the surface due to the shearing action of the Al sheets when ARB is performed without lubrication [113]. The rotated cube can also rotate to the copper type texture or vice versa by a simple 35° rotation along the transverse direction. The presence of the rotated cube, copper, and Dillamore orientations in the Al foil after UAM shows a similarity with textures developed after ARB. It is also pertinent to point out that the textures obtained after welding Al-Ti is identical to those obtained after welding Al-Steel. This similarity in texture between UAM and ARB has not been reported earlier. Due to this similarity in the texture it can be concluded that the underlying mechanism of bond formation is similar. As stated previously, there are two criteria to initiate a solid state weld.

- i. Removal of surface oxide
- ii. Asperity collapse to bring the metals into intimate contact

In the case of ARB (accumulative roll bonding), bonding is achieved by the plastic deformation alone and no macroscopic rise in temperature. The plastic deformation serves to remove the

oxide layers and bring nascent metals in intimate contact to achieve a solid-state bond [51]. Since in the case of ARB the mechanical strength increases with the increase in number of passes, it is hypothesized that by increasing the deformation of the foils we may increase the bond strength in UAM also.

6.4. Characterization of the heat treated samples:

Heat treated samples were also investigated for their microstructure. The main aim to perform such studies was to study the thickness of the intermetallic compounds at the interface. The SEM image of a smooth interface of a heat treated Ti–Al sample is shown in figure 6.5, where a transition zone exists between the aluminium and titanium. To investigate the chemistry within this zone, a diffusion profile was measured, shown in figure 6.5. Since EBSD shown in figure 6.3(a) showed significant defect density in the sonotrode affected regions it may result in enhanced diffusion rates causing significantly higher inter diffusion and intermetallic formation compared to the flat interfaces. To compare this an energy dispersive spectrum scan of an interface that was roughened by the sonotrode during welding is presented in figure 6.6. This roughened interface shows $\sim 5\mu\text{m}$ of diffusion across the interface, slightly more than the smooth interface, indicating that response of the interfaces to post weld heat treatment is heterogeneous across the interface. EBSD was performed at the interfaces to observe changes in the morphology of the grains at the interface. The results are shown in figure 6.7. The reason as to why EBSD was performed was to investigate if grain growth occurs at the interface during post weld heat treatment. Though it would be natural to expect significant grain growth previous work on Al-3003 similar welds shows that absence of grain growth at the interface during post weld heat treatment [64, 70]. The reason for such behavior has not yet been rationalized and is the subject of research. However surprisingly the grains at the interface showed significant

growth after post weld heat treatment in this case. This could be attributed to two reasons

- i. The significantly higher temperature and time that the Al-Ti interfaces were heat treated at
- ii. Due to the fact that the inherent mechanisms of the bond formation is different for the similar and dissimilar metals resulting in completely different behavior of the interfaces.

This could be a potential area for future research.

6.5. Mechanical testing and fractography of builds:

Mechanical testing was performed on a Gleeble ® the results from mechanical testing are presented in figure 6.8. The area under the curves shows a drastic rise for the heat treated material on comparison to the as welded material. This rise could be attributed to the formation of intermetallic layers. The formation of a thin layer of intermetallic helps to constrain the deformation at the interface and helps to increase the bond strength at the interface as noted by Troug. The alternate hypothesis is that intermetallic formation decreases the surface energy of the interface making the metallurgical bonding more complete [3]. This effect has been observed and documented in friction stir welding [4, 5, 9, 12, 15, 19, 22, 114]. The morphology of the difference in fracture of the surfaces is shown in figure 6.9(a) and (b). The figures show a transition from a brittle fracture to a more ductile failure mode arising as a result of the intermetallic formation. Fractography of the as welded specimen is shown in figure 5.10. The area examined shows a predominantly brittle region but localized ductile regions are observable. EDS maps were performed to understand if the ductility in those regions are associated due to the localized formation of solid state bond. If a solid-state bond had formed between the Al and Ti then the examined region should be not show any Ti signal since the Al should be bonded to the Ti and hence peeled away. The EDS

maps are shown in figure 5.10 (b) and (c) showing the Al and Ti distributions respectively. The regions where the ductile failure occurred correspond to an absence of Ti. This confirms that the ductile regions are indeed the result of a solid-state weld between Al and Ti where the strength of the interface exceeded the strength of the weld metal.

6.6. Summary and Conclusions:

Using electron backscatter diffraction, microstructure and texture evolution of the dissimilar Al-Ti builds fabricated using 9 kW UAM has been investigated. A hypothesis for the bond formation mechanism has been proposed. The results obtained are summarized below:

- i. Bond formation occurred without any intermetallic formation
- ii. As a consequence of the heavy plastic deformation in the Al, the crystallographic texture shows a strong $\{100\} \langle 110 \rangle$ (rotated cube component) with $\{112\} \langle 111 \rangle$ (copper component) and $\{4\ 4\ 11\} \langle 11\ 11\ 8 \rangle$ (Dillamore component). These texture components also form in Al alloys during ARB.
- iii. Mechanical testing and fractography indicated that metallurgical bonding occurred with plastic deformation concentrated on a single metal alone.
- iv. Heat treatment showed significant enhancement in mechanical properties and could be attributed to the formation of thin layer of intermetallic at the interface similar to observations made while using friction stir welding.

Based on the very similar texture evolution mechanism in ARB it is proposed that the bonding mechanisms in ARB and UAM rely only on severe plastic deformation. Since both the processes rely on extensive plastic deformation occurring at the interface future work can concentrate on engineering the crystallographic texture of the foils to maximize plastic deformation at the interface.

Chapter-7

Rationalization of bond formation mechanism in BCC-BCC metal combination

7.1. Introduction:

Microstructural evolution is the key to understand the extent of metallurgical bonding. Work on VHP UAM has been concentrated mostly on FCC metals. Recent publications indicate that the bond formation occurs due to complex interactions of many phenomena including mechanical interlocking due to plastic deformation [49], frictional heating, deformation heating, recrystallization, diffusion and contact between nascent surfaces [61, 67]. Extensive microscopy conducted on the Aluminum builds using dual beam FIB in conjunction with TEM revealed that the microstructure at the interfaces are affected by severe plastic deformation (SPD) of bulk (5 μm) resulting in the grain refinement (0.5 μm to few nanometers) [49]. The above observation confirms that the UAM process affects only the grains at the interface and does not have any major long-range effects into the bulk of materials. David Schick calculated the strain rate at the interface during deformation to be close to 10^5s^{-1} [62]. In order to understand the microstructure and texture evolution at the interface was measured using EBSD [49, 62] [57, 61, 67, 69, 70] and these results indicate large misorientation of the grains at the interface indicative of newly formed grains. Sriraman et al in their work on Cu [57] observed softening at the interface along with the presence of equiaxed grains with high angle grain boundaries, similar to observations in Al-3003 [57], and attributed these changes to dynamic recrystallization. This hypothesis was based on calculations that showed that the temperature rise due to adiabatic deformation exceeded $0.5T_m$ [57]. Micro texture data of Al-3003 build interfaces, obtained using EBSD, indicated a prominent shear texture $\{111\} \langle 110 \rangle$ in comparison to the rolling texture of the bulk [61, 67, 69]. Thermocouple measurements of the temperature rise at the Al-Al interface showed

only a moderate rise in the temperature around 220°C [62, 64, 90]. The above phenomenon was attributed to the extensive deformation and collapse of the micro asperities at the interface followed by dynamic recrystallization brought about by the heat generated during deformation [61, 67]. Similar observations have been made during friction stir welding of Al alloys. In friction stir welds, the {111} plane was roughly parallel to the direction of the pin and a <110> direction to the transverse direction of the plate. Since this orientation correlates well with critically resolved shear stress for slip, the correlation between texture development and plastic deformation was confirmed.

The motivation behind this work is to answer the question whether BCC materials also undergo similar dynamic recrystallization at the interface driven by the heat generated by the adiabatic plastic deformation process. Due to lack of any previous work with UAM, we embarked on a literature review with reference to deformation textures in BCC during severe plastic deformation (SPD) at high-strain rate deformations. During friction stir welding, which relies on high strain rate deformation, shear textures was observed by Mironov et.al [91]. Shear texture was also observed during friction stir processing of pure Iron [91]. These authors observed a fine grain structure with a low aspect ratio along with significant dislocation density [91]. Similarly nano structured grains were also obtained after severe plastic deformation (e.g., high pressure torsion) processes at high strain rate at ambient temperatures [66, 92-94], [95, 96]. The above grain structure evolution during high strain rate was correlated to grain sub division mechanism. Based on the above SPD literature, because of the similar shear strain rate magnitudes, the hypothesis is that grain sub-division may be an alternative mechanism for bond formation in BCC metals, instead of dynamic recrystallization. This hypothesis was explored in an industrially relevant dissimilar metal combination viz. steel and tantalum.

There has been significant interest in Ta over steel dissimilar metal joints, which finds applications as clads, in corrosive environments. Due to the high differences in the melting points of these metals (Ta: 3020°C and Fe: 1538°C), solid state welding techniques (e.g., explosive welding) is preferred instead of fusion welding. However, there is interest in using alternative solid state joining techniques, because of the possibility of intermetallic formation at the interface during explosive welding [97] as well as complex geometries. Goals of the current work are two folds (i) evaluate the feasibility of UAM using small samples and (ii) obtain fundamental knowledge of microstructural evolution for aiding future scaling up of UAM to make large-scale structures.

7.2. Experimental Work:

The material used for this study was 99.5% pure Ta sheet 50 μ m thick and 1010 steel substrate 2.5mm thick. The tape was placed over the substrate and ultrasonic vibrations were applied through a rotating sonotrode, which was made of Ti-6Al-4V. In this work, the welding parameters were developed using trial and error and were not optimized for bond strength. The welds used for characterization were the ones where the foils could not be detached from the substrate. The parameters used for the fabrication of the builds were a normal load of 7000N vibration amplitude of 36 μ m and a travel speed of 15 mm/s. The total length of the weld was 4 inches and the width of the foil used was 1". The build was cut parallel the Normal Direction (ND) using a low cutting speed with a coolant to avoid heating so as to preserve the substructures developed during plastic deformation. The naming convention used for the presentation of the microstructural data is shown in figure 4.1, i.e., ND, TD, and VD represent normal direction, transverse direction and vibration direction, respectively. The samples were mounted using conductive Bakelite and prior to polishing, the samples were ground with

abrasive paper using water as a lubricant and mechanically polished with a final polishing step comprising of a $1\mu\text{m}$ diamond paste. A suitable finish for EBSD was obtained by chemical-mechanical polishing on the Buehler Vibromet vibratory polisher with a non-crystalline colloidal silica suspension.

Characterization was performed using Optical microscopy, SEM with EDS, Electron Backscatter Diffraction and Nano indentation. The center of the builds were then analyzed using Scanning Electron microscopy and EBSD analysis was performed using a PHILIPS XL-30 FEG scanning electron microscope equipped with the TSL OIM EBSD system under 20kV accelerating voltage and a 17-mm working distance. The electron beam was scanned with a step size of $0.05\mu\text{m}$ in order to pick up small variations of misorientation within the grains. Hardness measurements were performed using a MTS Nano indenter XP was used to measure the hardness at selected locations using load vs. depth sensing techniques and a continuous stiffness measurement described elsewhere [89]. The indentation was carried out using a 3-faced Berkovich indenter and to a depth of 500 nm at a strain rate of 0.05s^{-1} and a dwell time of 20s to remove the time dependent plasticity effects. The adjacent indents were placed at a distance of $10\mu\text{m}$.

7.3. Results:

7.3.1. Scanning Electron Microscopy and EDS of VHP-UAM builds:

As stated in the previous chapters, standard technique used to estimate the effectiveness of bonding is a linear weld density (LWD), which is the ratio of the length of the interface that appears to be bonded to the total length of the interface. Due to the inhomogeneity of the bonding process the LWD for this case was measured from a 6 different SEM images taken from random locations at a low magnification 50X and the average LWD value was calculated. The

LWD was 0.76 or 76% of the total area was bonded. The reason for the low LWD in this case is due to the fact that no detailed design of experiments was performed to maximize the linear weld density. The figure 7.2(a)-(b) shows the interface characterized by SEM. The direction of the vibration of the sonotrode is marked on the images. There were regions where contact between the substrate and the foil has not occurred and regions where extensive plastic deformation had occurred. These features indicate heterogeneous bonding across the interfaces. The interface also had several wave like features similar marked in figure 7.2(b) similar to the features observed in samples joined by explosive welding [27]. The dark regions marked by arrows in figure 7.2(a) are voids indicating absence of contact between the substrate and foil. Across the interface are randomly dispersed voids in between bonded regions as shown in figure 7.2(a). Several unbonded regions correlate well with lack of metal-to-metal contact. The above phenomenon has been correlated to the heterogeneity of plastic deformation along the contact area of the sonotrode with the foil due to the differences in contact pressure [98, 99]. Several wave like features were characterized and Figure 7.2(b) shows a wavy interface (marked with arrows) associated with extensive plastic flow of the upper region of the foil. It also appears from figure 7.2(b) that the tantalum has flowed around the “hills” and “valleys” of the steel asperities (marked by arrows). This phenomenon has also been observed on the upper region of the foils and has been hypothesized to form as a result of the imprint of sonotrode on the top region of the foil. Adjacent to the wave features “micro porosity” had also been observed at a distance of $\sim 8\mu\text{m}$ from the interface and the size of these micro pores were around $\sim 3\text{--}5\mu\text{m}$. Similar “micro porosity” formation has also been previously observed in ultrasonic spot welds in areas made with higher energy. However, the micro-porosity observed in literature are due to excessive material flow, rather than lack of bonding. An EDS spectrum (figure 3(b)) reveals oxygen peaks

with strong iron and Ta peaks suggesting that the wear particles predominantly are broken off from the rubbing surfaces. The size of the wear debris was estimated to be from 2-10 micrometers based on optical microscopy.

In order to investigate the possibility of inter diffusion between the Ta and steel and to understand the breaking and dispersion of the oxides at the interface due to plastic flow, EDS maps were obtained from following locations: bonded region, wavy regions and incomplete bonding area [see marked in figure 7.4 (a)]. The maps show oxygen concentration at the unbonded interfaces. It is pertinent to mention that oxides were also observed in the aluminum UAM samples at Al-Al interfaces. Dehoff et.al, [49] hypothesized that these oxide layers formed as a result of melting of the Al layers due to adiabatic heating at the interfaces. Although our micrographic images appear to indicate extensive mixing between the Ta and steel at the interface [see figure 4.4 (a)], EDS analyses did not shown any inter diffusion of Ta and Fe across the interfaces. Furthermore, interdiffusion of Fe into Ta is highly improbable due to the low solid solubility of Fe in Ta, i.e., less than 2 at% at temperatures higher than 800°C.

7.3.2. Orientation Imaging Microscopy (OIM) using Electron Back Scattered diffraction:

EBSD was performed to examine the detailed micro-texture and rationalize the deformation processes at three regions, i.e., bonded region, wavy regions and incomplete bonding area. The microstructural characteristics of the non-bonded regions are shown in figure 7.5 (a) and (b). The image does not show any evidence for grain refinement or deformation. Grain orientation spread maps also confirm this observation. The GOS is the average deviation between the orientation of each point in the grain and the average orientation of the grain. GOS analyses are usually performed to rationalize the extent and mechanisms of plastic deformation at the interfaces [100]. GOS is sensitive to dislocation cells created during plastic deformation

compared to inverse pole figures (IPF) of grain images. The dislocation cells within a parent grain will have small misorientation with the matrix and thereby will not be indexed as new grains. This is expected since the EBSD grain-grouping algorithm simply enforces that any two points which differ in orientation less than a specific tolerance levels are part of the parent grain surrounding them. In a deformed grain with dislocation cells, the point-to-point misorientation may not exceed the tolerance angle to be indexed as a new grain. In contrast, the GOS is even small misorientations arising due to geometrically necessary dislocations (GND's). In addition to GOS, image quality indicator (IQI) maps can also be used to understand the amount of stored energy due to deformation in the sample qualitatively. Larger deformation results in a lower image quality due to lattice distortion. In figure 7.5(c), the image quality of the microstructure indicates minimal lattice deformations. The figure 7.5(c) shows a decrease in the IQI at the steel side of the interface indicating some amount of deformation (which is marked) and corresponding increase in the grain orientation spread in the region shown in figure 4.5(b).

The characteristics of the bonded regions are shown in figure 7.6. Figure 7.6 (c & d) correspond to the marked region in figure 7.6(a) at a higher magnification and obtained using a finer step size (5 nm) to detect small mis-orientations at the interface. The grains in the interface were equiaxed in nature with high angle grain boundaries as shown in figure 7.6(c). The black regions marked in figure 7.6(c) were present even in regions where it appeared to have physical continuity. However, EBSD patterns obtained from these regions could not be indexed. Figure 7.6(b) and 7.6(d) shows a gradual increase in the amount of grain orientation spread at the interface indicating high concentrations of geometrically necessary dislocations. It is pertinent to note that in the fine grained interface several grains are elongated with a comparatively high Grain orientation spread while several grains have a GOS close to 0° . There are some grains that

have a GOS close to 4° showing that these grains with larger GOS have residual geometrically necessary dislocations (GND's). Geometrically necessary dislocations form due the activation of different slip systems on each side of the grain, which is strongly correlated to the initial orientation of the grain itself [71].

The misorientation profiles of an equiaxed grain (marked grain-2 in figure 7.6(c)) and a grain at the sub surface (marked grain-1 in figure 7.6(c)) of the interface are extracted for comparison. The plot shows the misorientation changes as a function of the normalized distance. The grain at the interface (grain-2) showed a very low misorientation distribution. In contrast, the data from grain-1 indicates several peaks and the spacing between the peaks are of the order of the grain size of the equiaxed zone of the interface. A detailed account of this mechanism is presented in the discussions section. The grain size was calculated and the average grain size of the equiaxed grains at the interface was 125 nm showing the presence of nano crystalline grains at the interface.

Another region where there was excessive deformation and the formation of a “wavy interface” was characterized using EBSD and the IPF and the GOS analyses (see Fig. 7.7). The interface showed a fine-grained structure similar to bonded regions. The GOS maps confirmed the onset of intense deformation close to the interface. The dark un-indexed regions could not be indexed. The misorientation profiles of individual grains were also extracted for analysis from the Ta grain close to the interface (grain-3), steel grain close to the interface (grain-1) and a steel grain in the substrate (grain-2) for analysis (see figure 7.7b). The grain sizes here are much finer than those in the bonded regions.

The misorientation distribution of the grains showed peaks and the distance between certain peaks with high misorientations is of the order of the grain sizes at the interface. This is

similar to what had been observed in the bonded region, which supports similar deformation mechanisms for grain refinement on both cases. The misorientation distribution of the Ta and the steel grain at the interface reveals that the average misorientation is much higher in the Ta grain than the steel grain. This suggests higher extent of plastic strain in the Ta foil. This is expected considering the high purity of Ta foil used in this study. Often the reduction interstitial concentration is resorted to make soft tantalum. Confirmation of the relative differences in plastic deformation will be presented during the discussion of nano indentation data. Further analyses of the grain size, at the interfaces of both broken and bonded regions (shown in figure and figure 7.6), are presented in figure 7.8. The data clearly shows that the grains at the wavy region were much finer than bonded region.

The pole figures show the micro textures obtained from the bonded (see figure 7.9a) and the region where there is excess deformation (see figure 7.9b). The micro texture of the bonded region showed a Goss texture [see figure 7.8(a)], where the $\{110\}$ planes are aligned with the Normal Direction, and the $\langle 100 \rangle$ directions are aligned with the rolling (here vibration) direction. The ideal positions of a Goss Texture are also shown in figure 7.9(a). In the case of the sample with broken bond region, the presence of a strong shear component $\{111\} \parallel \text{ND}$ and $\langle 112 \rangle \parallel \text{RD}$ rotated about the normal direction was confirmed. These components are also present in the figure 7.9(a) in the bonded region and are highlighted with open triangles. This rotation could have occurred as a result of unstable nature Goss texture, which tends to rotate away with increased plastic deformation. The texture developed due to the excessive plastic deformation is also slightly stronger (i.e. 14 times than random) than the one was developed at the interface as shown in figure 7.9.

The gradual rise in the grain orientation spread from the base metal to the interface shows that lattice rotation is key feature driving the formation of the observed microstructure at the interface. The misorientation data of the selected grains also indicate significant orientation gradients developing within the grain. It is has been reported that the rotation of different portions of the original grain towards different stable texture components leads to refinement [101]. The OIM and the IQI maps in the non-bonded regions did not show any evidence for plastic deformation. The above EBSD analyses confirmed the role of plastic deformation in the bond formation mechanism.

7.3.3. Hardness measurements using Nano-Indentation:

The load vs. Indentation plots show the hardness data obtained through nano indentation near the bonded interface, sonotrode affected region and unbonded regions (see Fig. 7.10). Elastic recovery of less than 50 nm shows that the indentation was well beyond the plastic regime of the underlying material. The amount of elastic recovery for the steel at the interface is very high [figure 7.10(c)] which could be attributed to high yield strength. For a detailed understanding of the load versus indentation curve the reader is directed to a reference [89] paper. The data shows higher hardness values near the interface and the Sonotrode affected regions. Figure 7.10(a) shows that the hardness values for Ta at the interface are higher than the bulk equivalent to that of the sonotrode-affected regions. Interestingly, the EBSD analyses also showed significant grain refinement in similar regions. Based on the above, we hypothesize that the Hall - Petch effect leads to an increase in the hardness. The grain size was estimated using the Hall Petch relation for tantalum that is reported [95, 96]

$$H=780+690 d^{-1/2} \text{-----}(6)$$

Where H is the hardness in MPa and d is the grain size in μm . The hardness for Ta near the interface is 3.41 GPa and that of sonotrode affected region is 3.28 GPa. The grain sizes, which were calculated as per the Hall-Petch relationship was close to 68 and 76 nm at the interface and the sonotrode affected regions, respectively. This is less than those observed using EBSD. This indicates that the rise in hardness is not exactly driven by grain refinement but dislocation strengthening could also play a role. The grains with a high grain orientation spread at the interfaces suggest that dislocation strengthening could also contribute to the higher hardness rise. This analyses and microstructure data from previous sections confirm that similar deformation and grain refinement mechanisms occur at the interface and sonotrode affected regions. The regions between the sonotrode affected region and the interface has similar hardness value irrespective of condition of the interface (i.e. bonded or un bonded). Interestingly, the hardness at the sonotrode affected regions stays almost constant irrespective of the bond formation. At the same time, abetting interfaces at the un bonded regions show a drop in the hardness, confirming again lack of plastic deformation, thereby proving the significance of plastic deformation at the interfaces. On the steel side, we can see a significant increase in the hardness at the interface regions where the hardness is 5.6GPa and leveling off at 3.6GPa as a function of depth from the interface. This confirms the deformation in steel side is concentrated only close to the interface.

The initial region of the load vs. displacement curves for Ta shows that curves of the harder regions is identical to that of the softer regions up to a depth of 120nm and then later on the harder material shows very high rise in the slope. Also at the un bonded regions, both in the case of steel and Ta, the hardness values were lower and match with the hardness of the bulk. The inhomogeneity of the hardness values across the build, at the interface and sonotrode-

affected regions suggest that contact stress of the sonotrode across the build surface is indeed not uniform.

7.4. Discussions:

7.4.1. Bond formation mechanism during VHP UAM:

From the above results we observe that bonded interfaces have high hardness and refined grain structure with substantial defect density in certain grains (high GOS). To understand the above changes, let us restate three conditions required for solid state welding; (i) Atomistically clean surfaces; (ii) Intimate contact between nascent surfaces; and (iii) collapse of surface asperities. In order to induce the above conditions, the oxide layers have to be removed completely. In UAM, oxides layers and contaminants are removed as a result of the severe cyclic plastic deformation at the faying surfaces [45]. The second condition is to bring the surfaces into intimate contact. When a load is applied on the surfaces, the contact points yield allowing for the asperities to flow and induce micro welds. These micro-welds grow as a result of the transverse stresses due to ultrasonic vibrations. Since initial bonding occurs only at the local regions of contact, continued plastic deformation is necessary for the bond to grow by locally extruding the metal into the un bonded regions. We observe islands of micro welds in between bonded and un bonded regions fig 2. Similar localized micro welds have been observed previously [82]. This is a result of insufficient plastic deformation. The lack of sufficient deformation adjacent to these micro welds is supported by no change grain structure in the adjoining region. This has been reported elsewhere in Al-Al bonds [82]. Though the interface is sharp, we observe interpenetration of both Ta and steel near the wavy regions of the interface (fig 7.2). These features have been previously reported and hypothesized to be just mechanical intermixing. This mechanical intermixing is not similar to mechanical alloying that is observed in ball milling,

rather due to burying action of wear particles into sub-surface region due to complex asperity collapse and shear deformation. Nevertheless, recent reviews on sliding wear postulate atomic level mechanical mixing of atoms [102, 103]. As mentioned earlier, the non-homogeneity of bond formation can be attributed to the non-uniform contact pressure distribution and plastic deformation observed both along welding path and across foil width, in agreement with published results from ultrasonic welding [98, 99]. It is also pertinent to mention that despite the severe plastic deformation occurring in the Ta foil the foil does not bond with the sonotrode due to the following reason. For bond formation in UAM it is imperative that there be a relative motion between the foils. This occurs between the Ta and steel foil but not between the sonotrode and the Ta foil. However recent experiments using photon Doppler velocimetry has shown that after the bonding between the foil and substrate is complete then a relative motion between the top foil and the sonotrode was observed. Thus when the travel speed is slow and when the energy levels are high we may observe sticking of the foils to the sonotrode [45].

However as stated above a more detailed characterization is necessary to conclude experimentally about the nature of this mechanical mixing that occurs at the interfaces. Wave features (see figure 2) were observed during ultrasonic spot-welding also [82] and were attributed to excessive plastic deformation. However, in our case the formation of waves can be understood using the following mechanism outlined by Hopkins et al [46, 104] with dissimilar Al-Ti welds. In their work, softer Al flowed around the contours of the harder Ti during and therefore no deformation induced was expected. Nano indentation measurements show that Ta had hardened at the interface possibly due to grain refinement at the interface. EBSD data also seems to indicate that the bulk of deformation was concentrated on the softer Ta. This may have led to poor oxide removal on the steel surface due to the lack of asperity collapse which brings

atomistically clean surfaces which are hypothesized to be required for initiating a solid state weld where metallurgical bonding can occur.

There are a numerous regions where bonding had not occurred despite extensive plastic deformation observed (fig 7.2(b)). One possible reason could be attributed to breaking of the pre-existing bonds. This has been previously observed and reported [38] where, an increase in amplitude did not correspond to increased strength and linear weld density. This phenomenon was attributed to excessive strain hardening resulting in the bond degradation and rationalized as following. As soon as a weld is established it will be subjected to high frequency ultrasonic vibrations. During each cycle a balance between increase in adhesion and the degradation of the pre-existing bond due the high frequency ultrasonic vibrations may occur. As a result, there is an optimum energy window within which the continued bond formation may occur without breaking the pre-existing or bonds that formed in previous vibration cycles. A less ultrasonic power would result in the lack of metal-to-metal contact and an increase in the energy would lead to the fracture of the pre-existing bond (see figure 7.7a). The above hypothesis is supported by OIM data, where the interface shows clear signs of excess plastic deformation by an increased misorientation and associated increase in GOS at the interface grains. Furthermore, the grain size in the broken bond region is much finer than that of bonded interface.

7.4.2. On the evolution of grain structure at the interface:

OIM results shown in figure 7.6 and 7.7 do not indicate a uniform equiaxed structure as observed by previous researchers. EBSD of UAM builds carried out by Fuji et al and several others [49, 57-59, 61, 62, 64, 67, 70] seem to indicate dynamic recrystallization at the bond interface. They attribute the frictional heating during deformation and the high temperature rise due to adiabatic heating to be the driving force for dynamic recrystallization by grain boundary

migration to occur. In order to explore the possibility of dynamic recrystallization by grain boundary migration in this case it is essential to measure the temperature rise at the interface due to adiabatic heating, which would then be used to understand the kinetics of grain boundary migration at the interface. The rise in temperature is calculated as follows

$$\Delta T = \frac{0.9}{\rho C_p} \int_0^{\varepsilon_f} \sigma d\varepsilon \text{ -----(7)}$$

Where T is the rise in temperature, ρ is the density of Ta (16.53 g/cm³) and C_p of 0.153 Jg⁻¹K⁻¹, σ is the flow stress which in this case is calculated based on the Zerilli Armstrong Equation [95].

$$\sigma = C_o + B_o e^{-\beta T} + K \varepsilon^n \text{ ----(8)}$$

$$\beta = \beta_o - \beta_1 \ln \varepsilon' \text{ -----(9)}$$

Where C_o is the contribution due to lattice friction the second term is the contribution due to strain rate and the third term is the Holloman equation for strain hardening. The values for these constants taken from [95, 96] are $C_o=30$ MPa, B_o 1110MPa, β_o 0.005K⁻¹, β_1 0.000327K⁻¹, K 310MPa, and n 0.44. The flow stress obtained from this calculation is integrated over the total strain ε_f . The strain was calculated based on the approach outlined by Sriraman et.al [57]. The asperity height 15 μ m, which was measured based on SEM measurements near regions where the asperity had not collapsed. The shear strain due to lateral displacement of asperities during ultrasonic processing was obtained by using the equation (strain =2 x amplitude/asperity height). Based on these strain values, we arrive at a temperature rise of 700K with shear strain equal to 5 and with a shear strain of 10 the temperature can reach 1000K.

These calculations also show that the temperature rise during adiabatic heating is lower than 0.5T_m. The calculated temperature rise is indeed very sensitive to the strain rate and therefore at regions where the shear strain exceeds a critical value it is possible to promote

recrystallization by grain boundary migration and inter diffusion similar to that of Al-Al bonds. The shear strain is also dependent on the asperity height. It was reported that bonds made on dissimilar metal welds using Al-Cu combinations showed an increase in strength with increase in the surface roughness of the layers. Dynamic recrystallization followed by large grain boundary migration across the faying interfaces cannot occur when the temperature is only 700K. Therefore, we need a different mechanism to explain the observed microstructural features in BCC-BCC dissimilar joints.

Dynamic recrystallization of grains can occur by a continuous and rotational process occurring concomitantly with plastic deformation that leads to sub grain formation which is followed by gradual increase in their misorientation, finally leading to an equiaxed microstructure with high angle grain boundaries. The above process occurs at interfaces with no long-range diffusion. In contrast, migrational dynamic recrystallization occurs by the movement pre-existing high angle grain boundaries of strain free grains through the deformed microstructure resulting in the overall growth of strain free grains [71, 105]. In the current work, the presence of geometrically necessary dislocations that is evident from a GOS value of close to 4° at the interface region suggests that migrational dynamic recrystallization may not be operative here, rather rotational dynamic recrystallization might be occurring. Such a mechanism has been observed in adiabatic shear bands of Ta alloys[66]. Rotational recrystallization is also stated as continuous dynamic recrystallization, which can generate fine-grained structures requires continuous plastic deformation. The dislocations generated during the plastic deformation after reaching a critical level will forms elongated sub grains, which occur to minimize the strain energy in the lattice. With continuing deformation the sub grains eventually break up into equiaxed grains at the interface and continued rotation increases the misorientation

between the grains leading to the HAB's observed at the interface. Continued deformation causes the further refinement of these grains and thus very fine grain distribution, which has resulted in the finer grain structure in the figure 7.7.

7.4.3. On the texture evolution at the interfaces:

On close examination of the OIM IPF maps there are certain grains that have a well-developed sub grain structure (and have a high GOS value) at the interface while other grains have a low GOS and no substructure development. This means that the deformation has not resulted in any orientation gradients within the grain itself. This could be rationalized as follows. It has been reported in the literature that the orientation gradient in the grains depends strongly on the “Taylor Factor” which in turn depends initial orientation of the individual crystals [106] Taylor Factor corresponds to the ease with which a grain deforms homogeneously. A grain with a low Taylor factor such as the ‘rotated cube orientation’ $\{001\} \langle 110 \rangle$ deforms homogeneously and doesn't develop sub grains whereas the $\{111\} \langle uvw \rangle$ and $\{112\} \langle 110 \rangle$ (α fiber grains) develop a large orientation gradient since different regions within the grain deforms by different slip systems [107]

The formation of Goss texture where the $\{110\}$ parallel to the ND and the $\langle 100 \rangle$ parallel to the RD normally occurs during recrystallization of the heavily deformed 3% Silicon steels or in grains with $\{111\} \langle 112 \rangle$ orientations. The rationale was that of oriented nucleation where the $\{111\} \langle 112 \rangle$ orientation with a high Taylor factor that had formed as a result of severe shear banding had served as a nucleation site where the Goss grains had nucleated [108]. However it had been shown that the Goss texture is a result of static recrystallization. The Goss texture has also been previously observed as a surface texture in steels when rolling is carried out without any lubrication and the temperature is close to 700°F where the $\{100\} \langle 110 \rangle$ texture transforms

to a $\{110\} \langle 100 \rangle$ texture primarily due to shear at the surface. But other observations have also reported the formation of Goss texture at room temperatures when subjected to a combination of plane strain and shear deformation. The shear deformation tends to stabilize the Goss texture which is unstable under a plane strain condition and rotates to a $\{001\} \langle 110 \rangle$ and $\{111\} \langle 112 \rangle$ texture [109]. The intense shear deformation at the interfaces in the case of VHP UAM could have resulted in the formation of a stable Goss texture at the interface. From the adiabatic heating rate calculations it is also clear that the temperatures developed are insufficient to promote static recrystallization at the interface due to short time involved and hence the Goss texture that has developed at the interface is clearly due the imposed plastic deformation alone. However in the case of the region where the bonds were hypothesized to be broken the further increased deformation could rotate the Goss texture to a $\{111\} \langle 112 \rangle$ texture as shown previously which is confirmed by the texture shown in the figure 9(b).

Based on the above discussions, we can state that the degree of grain refinement in BCC-BCC UAM joints is predominantly dictated by the amount of plastic deformation alone and not due to the adiabatic heating alone, as previously hypothesized [67]. The initial crystal orientation dictates the degree of sub division necessary. And on reaching certain stable orientations, the grains do not sub divide further [as seen in EBSD (figure 7.6 (a), 7.6(c))]. Thus it is concluded that the grains at the interface had formed by a continuous dynamic recrystallization process which involves grain rotation driven by plastic deformation resulting the in the formation of the fine grain structure at the interface.

7.5. Conclusions:

The present study examined the feasibility of Fe-Ta dissimilar metal combinations using UAM and details of microstructure evolution. Although, success welds were obtained, the microstructural characterization showed three distinct regions:

- i. No mechanical contact: Voids due to lack of any interaction between faying surfaces, as well as low grain orientation spread; the unbonded interface regions are softer than bulk regions
- ii. Optimum deformation and intimate metal to metal contact: Good solid-state bonding, fine interface grains with large misorientation and with Goss texture, that are harder than matrix
- iii. Excessive deformation: leads to breakage of pre-existing bonds, but still shows fine interface grains with large misorientation spread formed during bonding. These broken regions also exhibit shear texture and are harder than matrix

The above heterogeneity in deformation, changes in crystal texture, and hardness is attributed to the differences in the contact pressure of the sonotrode along these regions, as well as, initial orientation of the grains. Based on the observed observations, we conclude that the good bonded interface regions evolve by continuous plastic deformation, adiabatic heating to temperatures below $0.5T_m$, subdivision of original matrix grains, followed by grain rotation through a continuous dynamic recrystallization process. The above hypothesis was supported through detailed characterization of textures at the faying interfaces and the calculations of adiabatic heating during high strain rate processing.

Chapter-8

Summary and conclusions

8.1. Summary:

The driving force for solid state welding is the total reduction of the surface energy at the interface. This can occur by a wide range of processes such as interdiffusion, recrystallization, plastic deformation or a combination of everything. However for any of these processes to occur it is essential to remove the oxide layer and collapse the asperities. Hence irrespective of the welding process used all solid state welds rely on plastic deformation with or without the generation of heat. The role of plastic deformation is considered crucial for bond formation to occur since plastic deformation serves to collapse asperities and remove the oxide layer. Ultrasonic additive manufacturing is a solid state additive manufacturing technique with the ability to fabricate complex geometries. However some of the underlying aspects of UAM are still unknown. The fundamental question that this thesis aimed to address was if the dissimilar metals with significant differences in deformation characteristics could be joined using UAM by deforming only the softer metal in a dissimilar metal combination. This question was answered by using multi scale characterization techniques to characterize aluminum and steel welds fabricated using ultrasonic additive manufacturing. The generality of these conclusions were then evaluated by welding aluminum to titanium and steel to tantalum and characterizing those using similar techniques.

8.2. Aluminum to steel:

Steel and aluminum were successfully fabricated using UAM. The mechanical strengths of the dissimilar aluminum to steel builds were compared to the similar aluminum to aluminum builds using push pin testing. Mechanical testing shows a transition in the failure mode from delamination to a ductile failure in the dissimilar metal combination. This transition resulted in

increased strength levels of the dissimilar metal joint compared to the similar joint. Based on the morphology of the failure the region where the transition occurred was characterized using Multi scale characterization. Optical microscopy and scanning electron microscopy showed the absence of intermetallic layers at the interface proving that bonding during UAM does not rely on long range diffusion. Characterization using electron back scattered diffraction and transmission electron microscopy showed that the interface had significant grain refinement. This refinement is hypothesized to be a result of a dynamic recrystallization process. Analysis of the texture showed that the interface had a rotated cube texture where the $\{100\}$ aligned with the normal direction and the $\langle 110 \rangle$ is aligned with the rolling direction. This texture has been reported to occur during accumulative roll bonding of Al-5XXX alloys and is associated with severe shear deformation. This proves beyond doubt that plastic deformation is the primary mechanism of bond formation in dissimilar metals using UAM. Atom probe tomography was performed to rationalize the mechanism of oxide dispersion. The atom probe data provided evidence for an aluminum matrix with supersaturated oxygen (~ 20 at.%) near interface. This level of segregation is indeed extraordinary in comparison to equilibrium levels of 3×10^{-8} at %. Based on these results, it is proposed that the oxide dispersion mechanism involves severe high-strain rate (10^5s^{-1}) plastic deformation at the interfaces rendering the oxide unstable. This unstable oxide later decomposes by dissolution of oxygen within the matrix leading to a driven alloy with non-equilibrium supersaturation. The mechanism is proposed to be very similar to what occurs in driven alloys. However to elucidate the structure of the matrix at such high levels of supersaturation extensive analysis using electron energy loss spectroscopy needs to be performed.

8.3. Aluminum to titanium welds:

To evaluate the generality of the above mentioned conclusions similar techniques were used to characterize the interface of aluminum-titanium welds. Using electron backscatter diffraction, microstructure and texture evolution of the dissimilar Al-Ti builds fabricated using 9 kW UAM has been investigated. A hypothesis for the bond formation mechanism has been proposed. The results obtained are summarized below:

- i. Bond formation occurred without any intermetallic formation
- ii. As a consequence of the heavy plastic deformation in the Al, the crystallographic texture shows a strong $\{100\} \langle 110 \rangle$ (rotated cube component) with $\{112\} \langle 111 \rangle$ (copper component) and $\{4 4 11\} \langle 11 11 8 \rangle$ (Dillamore component). These texture components also form in Al alloys during ARB and were also observed while welding aluminum to steel. Based on the very similar texture evolution mechanism in ARB it is proposed that the bonding mechanisms in ARB and UAM rely only on severe plastic deformation. Since both the processes rely on extensive plastic deformation occurring at the interface future work can concentrate on engineering the crystallographic texture of the foils to maximize plastic deformation at the interface.
- iii. Mechanical testing and fractography indicated that metallurgical bonding occurred with plastic deformation concentrated on a single metal alone thus validating that the conclusions from welding aluminum and steel can be applied to a wide range of dissimilar metal combinations.

In addition to characterization to understand the bond formation mechanism the efficacy of post weld heat treatments on the bond strengths were also evaluated. Samples were post processed by heat treating at 600°C for one hour. Heat treated samples show two fold increases in mechanical

strength compared to the as-built samples for both push-pin and shear strength tests, achieving ultimate shear strengths over 100 MPa. Microstructural evaluations showed no indications of voids or intermetallic formations in as-built samples and that the deformation and grain refinement is restricted to the aluminum layers. Diffusion of 5 μm and a small intermetallic layer is formed between the titanium and aluminum layers with significant grain growth occurring only on the aluminum side of the interface. This intermetallic layer is hypothesized as responsible for the increases in mechanical strength of the samples

8.4. Steel to tantalum welds:

To evaluate the bond formation mechanism with metals with a huge difference in recrystallization temperatures steel to tantalum welds were fabricated and characterized. Microstructural characterization showed three distinct regions:

- i. No mechanical contact: Voids due to lack of any interaction between faying surfaces, as well as low grain orientation spread; the unbonded interface regions are softer than bulk regions
- ii. Optimum deformation and intimate metal to metal contact: Good solid-state bonding, fine interface grains with large misorientation and with Goss texture, that are harder than matrix
- iii. Excessive deformation: leads to breakage of pre-existing bonds, but still shows fine interface grains with large misorientation spread formed during bonding. These broken regions also exhibit shear texture and are harder than matrix

Chapter-9

Future directions

9.0 Future directions:

The knowledge gained from this work can be used to join harder and high strength materials. The major problem limiting the application of ultrasonic additive manufacturing from being used to fabricate hard materials is the limited deformation that the hard materials undergo. It has been proven in this thesis that with sufficient plastic deformation it is possible to promote the formation of a metallurgical bond with deformation localized in one metal alone. Hence a soft interlayer can be used to weld the harder metal combinations together. The interlayer should be selected such that the interlayer displays unlimited solid solubility with the harder material. The interlayer could then be dissolved into the metal substrate by a long term anneal. Some preliminary results by using Ni interlayers to weld steel and later dissolve the nickel into the steel has been successful.

UAM is uniquely poised to fabricate metal ceramic composites. These materials could potentially be fabricated by mixing a ceramic and a soft metal and rolling the mixture into sheets and then consolidating the same using ultrasonic additive manufacturing. Preliminary experiments have shown reasonable success in development of such materials.

Apart from the limited deformation capability of the hard material the other major reason preventing the use of much harder materials would be the limitation of the sonotrode itself. Though modern UAM machines can deliver up to 9kW in theory such high powers are not being used currently. One problem limiting to going to such high powers is that the foil starts to nugget to the sonotrode. This “nuggeting” arises primarily due to a fundamental wear mechanism called galling. Galling is a phenomena where prolonged sliding of a material A on the surface of material

B cases material B to adhere to material A. In the case of UAM the material A would be the sonotrode and material B would be the foil that is being consolidated. To prevent galling a galling resistant hard facing coating needs to be developed on the sonotrode. Typical candidates would be cobalt based alloys such as stellite-6 or cobalt chrome alloys. Coating could be achieved using laser based directed energy deposition techniques and then evaluated by welding titanium alloys. The exact mechanism by which a dissimilar metal interface deforms is not yet well understood. For instance ideally the interface/weld has to be stronger than the base metal. In the case of a dissimilar metal weld (a hard and soft combination) the interface will be stronger than the weaker metal in theory if a metallurgical bond exists. It would be interesting to use digital image correlation along with in situ neutron or synchrotron diffraction to study how the load partitions across these interfaces. Such studies will throw light on more fundamental mechanisms as to how a lamellar structure would deform when loaded.

References

- [1] J. DuPont. Microstructural evolution and high temperature failure of ferritic to austenitic dissimilar welds, *International Materials Reviews* 57 (2012) 208-234.
- [2] T. DebRoy, H. Bhadeshia. Friction stir welding of dissimilar alloys—a perspective, *Science and Technology of Welding & Joining* 15 (2010) 266-270.
- [3] R. Dixon, S. Chen. Fundamentals of Metal and, *ASM handbook: Welding, brazing, and soldering* 6 (1993) 143.
- [4] M. Uday, M. Ahmad Fauzi, H. Zuhailawati, A. Ismail. Advances in friction welding process: a review, *Science and Technology of Welding & Joining* 15 (2010) 534-558.
- [5] M. Maalekian. Friction welding—critical assessment of literature, *Science and Technology of Welding & Joining* 12 (2007) 738-759.
- [6] W. Lucas. Process parameters and friction welds, *Metal Construction and British Welding Journal* 5 (1973) 293-297.
- [7] P. Li, J. Li, X. Li, J. Xiong, F. Zhang, L. Liang. A study of the mechanisms involved in initial friction process of continuous drive friction welding, *Journal of Adhesion Science and Technology* 29 (2015) 1246-1257.
- [8] S. Fukumoto, T. Inoue, S. Mizuno, K. Okita, T. Tomita, A. Yamamoto. Friction welding of TiNi alloy to stainless steel using Ni interlayer, *Science and Technology of Welding & Joining* 15 (2010) 124-130.
- [9] Y.-C. Kim, A. Fuji. Factors dominating joint characteristics in Ti–Al friction welds, *Science and Technology of Welding & Joining* 7 (2002) 149-154.
- [10] M. Aritoshi, K. Okita. Friction welding of dissimilar metals, *Welding international* 17 (2003) 271-275.

- [11] B.S. Yilbaş, A.Z. Şahin, N. Kahraman, A.Z. Al-Garni. Friction welding of St~~508~~ Al and Al~~7075~~ Cu materials, *Journal of Materials Processing Technology* 49 (1995) 431-443.
- [12] A. Fuji. In situ observation of interlayer growth during heat treatment of friction weld joint between pure titanium and pure aluminium, *Science and Technology of Welding & Joining* 7 (2002) 413-416.
- [13] R. Nandan, T. DebRoy, H. Bhadeshia. Recent advances in friction-stir welding—process, weldment structure and properties, *Progress in Materials Science* 53 (2008) 980-1023.
- [14] D.-H. Choi, C.-Y. Lee, B.-W. Ahn, Y.-M. Yeon, S.-H. Park, Y.-S. Sato, H. Kokawa, S.-B. Jung. Effect of fixed location variation in friction stir welding of steels with different carbon contents, *Science and Technology of Welding & Joining* 15 (2010) 299-304.
- [15] T. Watanabe, H. Takayama, A. Yanagisawa. Joining of aluminum alloy to steel by friction stir welding, *Journal of Materials Processing Technology* 178 (2006) 342-349.
- [16] R. Ayer, H. Jin, R. Mueller, S. Ling, S. Ford. Interface structure in a Fe–Ni friction stir welded joint, *Scripta Materialia* 53 (2005) 1383-1387.
- [17] Y. Chen, K. Nakata. Effect of the surface state of steel on the microstructure and mechanical properties of dissimilar metal lap joints of aluminum and steel by friction stir welding, *Metallurgical and Materials Transactions A* 39 (2008) 1985-1992.
- [18] N. Yamamoto, J. Liao, S. Watanabe, K. Nakata. Effect of intermetallic compound layer on tensile strength of dissimilar friction-stir weld of a high strength Mg alloy and Al alloy, *Materials transactions* 50 (2009) 2833-2838.
- [19] P. Xue, B. Xiao, D. Ni, Z. Ma. Enhanced mechanical properties of friction stir welded dissimilar Al–Cu joint by intermetallic compounds, *Materials science and engineering: A* 527 (2010) 5723-5727.

- [20] T. Tanaka, T. Morishige, T. Hirata. Comprehensive analysis of joint strength for dissimilar friction stir welds of mild steel to aluminum alloys, *Scripta Materialia* 61 (2009) 756-759.
- [21] R.S. Mishra, Z. Ma. Friction stir welding and processing, *Materials Science and Engineering: R: Reports* 50 (2005) 1-78.
- [22] Y. Chen, K. Nakata. Microstructural characterization and mechanical properties in friction stir welding of aluminum and titanium dissimilar alloys, *Materials & Design* 30 (2009) 469-474.
- [23] A. Shirzadi, H. Assadi, E. Wallach. Interface evolution and bond strength when diffusion bonding materials with stable oxide films, *Surface and interface analysis* 31 (2001) 609-618.
- [24] X. Wu, J. Shang. An investigation of magnetic pulse welding of Al/Cu and interface characterization, *Journal of Manufacturing Science and Engineering* 136 (2014) 051002.
- [25] A.A. Mousavi, S. Al-Hassani. Numerical and experimental studies of the mechanism of the wavy interface formations in explosive/impact welding, *Journal of the Mechanics and Physics of Solids* 53 (2005) 2501-2528.
- [26] B. Crossland, J. Williams. Explosive welding, *Metallurgical Reviews* 15 (1970) 79-100.
- [27] M. Hammerschmidt, H. Kreye. Microstructure and bonding mechanism in explosive welding. *Shock Waves and High-Strain-Rate Phenomena in Metals*. Springer, 1981. pp. 961-973.
- [28] Y. Zhang, S. Babu, P. Zhang, E.A. Kenik, G. Daehn. Microstructure characterisation of magnetic pulse welded AA6061-T6 by electron backscattered diffraction, *Science and Technology of Welding & Joining* 13 (2008) 467-471.

- [29] Y. Zhang, S.S. Babu, G.S. Daehn. Interfacial ultrafine-grained structures on aluminum alloy 6061 joint and copper alloy 110 joint fabricated by magnetic pulse welding, *Journal of materials science* 45 (2010) 4645-4651.
- [30] G.S. Daehn, J. Lippold, D. Liu, G. Taber, H. Wang. Laser impact welding. 5th International Conference on High Speed Forming 2012, 2012.
- [31] M. Marya, S. Marya. Interfacial microstructures and temperatures in aluminium–copper electromagnetic pulse welds, *Science and Technology of Welding & Joining* 9 (2004) 541-547.
- [32] N. Kahraman, B. Gülenç, F. Findik. Joining of titanium/stainless steel by explosive welding and effect on interface, *Journal of Materials Processing Technology* 169 (2005) 127-133.
- [33] N. Kahraman, B. Gülenç. Microstructural and mechanical properties of Cu–Ti plates bonded through explosive welding process, *Journal of Materials Processing Technology* 169 (2005) 67-71.
- [34] M. Acarer, B. Demir. An investigation of mechanical and metallurgical properties of explosive welded aluminum–dual phase steel, *Materials letters* 62 (2008) 4158-4160.
- [35] M. Acarer, B. Gülenç, F. Findik. Investigation of explosive welding parameters and their effects on microhardness and shear strength, *Materials & design* 24 (2003) 659-664.
- [36] D. Gu, W. Meiners, K. Wissenbach, R. Poprawe. Laser additive manufacturing of metallic components: materials, processes and mechanisms, *International materials reviews* 57 (2012) 133-164.
- [37] Y. Yang, G.J. Ram, B. Stucker. Bond formation and fiber embedment during ultrasonic consolidation, *Journal of Materials Processing Technology* 209 (2009) 4915-4924.

- [38] G.J. Ram, Y. Yang, B. Stucker. Effect of process parameters on bond formation during ultrasonic consolidation of aluminum alloy 3003, *Journal of Manufacturing Systems* 25 (2006) 221-238.
- [39] A.G. Truog. Bond improvement of Al/Cu joints created by very high power ultrasonic additive manufacturing. The Ohio State University, 2012.
- [40] D. Tabor. Junction growth in metallic friction: the role of combined stresses and surface contamination. *Proceedings of the Royal Society of London A: Mathematical, Physical and Engineering Sciences*, vol. 251: The Royal Society, 1959. p.378-393.
- [41] D. Milner, G. Rowe. Fundamentals of solid-phase welding, *Metallurgical Reviews* 7 (1962) 433-480.
- [42] B. Bethune, R. Waterhouse. Adhesion of metal surfaces under fretting conditions II. Unlike metals in contact, *Wear* 12 (1968) 369-374.
- [43] C. Kong, R. Soar, P. Dickens. Optimum process parameters for ultrasonic consolidation of 3003 aluminium, *Journal of materials processing technology* 146 (2004) 181-187.
- [44] C. Kong, R. Soar, P. Dickens. Characterisation of aluminium alloy 6061 for the ultrasonic consolidation process, *Materials Science and Engineering: A* 363 (2003) 99-106.
- [45] D. Foster, G. Taber, S. Babu, G. Daehn. In situ velocity measurements of very high power ultrasonic additive manufacturing using a photonic Doppler velocimeter, *Science and Technology of Welding and Joining* 19 (2014) 157-163.
- [46] C. Hopkins, P. Wolcott, M. Dapino, A. Truog, S. Babu, S. Fernandez. Optimizing ultrasonic additive manufactured Al 3003 properties with statistical modeling, *Journal of Engineering Materials and Technology* 134 (2012) 011004.

- [47] I.E. Gunduz, T. Ando, E. Shattuck, P.Y. Wong, C.C. Doumanidis. Enhanced diffusion and phase transformations during ultrasonic welding of zinc and aluminum, *Scripta materialia* 52 (2005) 939-943.
- [48] H. Kreye. Melting phenomena in solid state welding processes, *Weld. J* 56 (1977) 154-158.
- [49] R. Dehoff, S. Babu. Characterization of interfacial microstructures in 3003 aluminum alloy blocks fabricated by ultrasonic additive manufacturing, *Acta Materialia* 58 (2010) 4305-4315.
- [50] H. Mohamed, J. Washburn. Mechanism of solid state pressure welding, *Welding J* 55 (1975) 302s-310s.
- [51] L. Li, K. Nagai, F. Yin. Progress in cold roll bonding of metals, *Science and Technology of Advanced Materials* 9 (2008) 023001.
- [52] R. Tylecote. Pressure welding in practice, *Welding Technology-British Welding Journal* 4 (1957) 113-119.
- [53] L. Vaidyanath, M. Nicholas, D. Milner. Pressure welding by rolling, *BRITISH WELDING JOUR* 6 (1959) 13-28.
- [54] Y. Lu, J.Y. Huang, C. Wang, S. Sun, J. Lou. Cold welding of ultrathin gold nanowires, *Nature nanotechnology* 5 (2010) 218-224.
- [55] J.M. Parks. Recrystallization welding, *Welding J* 32 (1953) 209s-222s.
- [56] R. Tylecote. *The Solid State Welding of Materials*. New York: St. Martin's Press, 1968.
- [57] M. Sriraman, S. Babu, M. Short. Bonding characteristics during very high power ultrasonic additive manufacturing of copper, *Scripta Materialia* 62 (2010) 560-563.

- [58] K. Johnson, H. Edmonds, R. Higginson, R. Harris. New discoveries in ultrasonic consolidation nano-structures using emerging analysis techniques, Proceedings of the Institution of Mechanical Engineers, Part L: Journal of Materials Design and Applications (2011) 0954420711413656.
- [59] K.E. Johnson. Interlaminar subgrain refinement in ultrasonic consolidation, (2008).
- [60] T. Watanabe, A. Yanagisawa, S. Sunaga. Auger electron spectroscopy analysis at the ultrasonically welded interface between alumina and aluminum, Metallurgical and Materials Transactions A 34 (2003) 1107-1111.
- [61] S. Shimizu, H. Fujii, Y. Sato, H. Kokawa, M. Sriraman, S. Babu. Mechanism of weld formation during very-high-power ultrasonic additive manufacturing of Al alloy 6061, Acta Materialia 74 (2014) 234-243.
- [62] D. Schick, R. Hahnlen, R. Dehoff, P. Collins, S. Babu, M. Dapino, J. Lippold. Microstructural Characterization of Bonding Interfaces in Aluminum 3003 Blocks Fabricated by Ultrasonic Additive Manufacturing-Methods were examined to link microstructure and linear weld density to the mechanical properties of ultrasonic additive manufacturing, Welding Journal 89 (2010) 105S.
- [63] G.T. Gray III. High-strain-rate deformation: mechanical behavior and deformation substructures induced, Annual Review of Materials Research 42 (2012) 285-303.
- [64] D.E. Schick. Characterization of aluminum 3003 ultrasonic additive manufacturing. The Ohio State University, 2009.
- [65] M. Wonjoo, S. Songwon, L. Jaeyoung, M. Oakkey. Dynamic shear stress of tough-pitch copper at high strain and high strain-rate, KSME international journal 16 (2002) 1412-1419.

- [66] M.A. Meyers, V.F. Nesterenko, J.C. LaSalvia, Q. Xue. Shear localization in dynamic deformation of materials: microstructural evolution and self-organization, *Materials Science and Engineering: A* 317 (2001) 204-225.
- [67] H.T. Fujii, M. Sriraman, S. Babu. Quantitative evaluation of bulk and interface microstructures in Al-3003 alloy builds made by very high power ultrasonic additive manufacturing, *Metallurgical and Materials Transactions A* 42 (2011) 4045-4055.
- [68] R. Armstrong, W. Arnold, F. Zerilli. Dislocation mechanics of shock-induced plasticity, *Metallurgical and materials transactions A* 38 (2007) 2605-2610.
- [69] E. Mariani, E. Ghassemieh. Microstructure evolution of 6061 O Al alloy during ultrasonic consolidation: an insight from electron backscatter diffraction, *Acta Materialia* 58 (2010) 2492-2503.
- [70] K. Sojiphan. Effects of Very High Power Ultrasonic Additive Manufacturing Process Parameters on Hardness, Microstructure, and Texture of Aluminum 3003-H18 Alloy. The Ohio State University, 2015.
- [71] R. Doherty, D. Hughes, F. Humphreys, J. Jonas, D.J. Jensen, M. Kassner, W. King, T. McNelley, H. McQueen, A. Rollett. Current issues in recrystallization: a review, *Materials Science and Engineering: A* 238 (1997) 219-274.
- [72] R. Fonda, K. Knipling. Texture development in friction stir welds, *Science and Technology of Welding and Joining* 16 (2011) 288-294.
- [73] S. Roy, B. Nataraj, S. Suwas, S. Kumar, K. Chattopadhyay. Accumulative roll bonding of aluminum alloys 2219/5086 laminates: Microstructural evolution and tensile properties, *Materials & Design* 36 (2012) 529-539.

- [74] S. Roy, S. Singh, S. Suwas, S. Kumar, K. Chattopadhyay. Microstructure and texture evolution during accumulative roll bonding of aluminium alloy AA5086, *Materials Science and Engineering: A* 528 (2011) 8469-8478.
- [75] J. Hirsch, K. Lücke. Overview no. 76: Mechanism of deformation and development of rolling textures in polycrystalline fcc metals—I. Description of rolling texture development in homogeneous CuZn alloys, *Acta Metallurgica* 36 (1988) 2863-2882.
- [76] J. Hirsch, K. Lücke, M. Hatherly. Overview No. 76: Mechanism of deformation and development of rolling textures in polycrystalline fcc Metals—III. The influence of slip inhomogeneities and twinning, *Acta Metallurgica* 36 (1988) 2905-2927.
- [77] E. Neppiras. Ultrasonic welding of metals, *Ultrasonics* 3 (1965) 128-135.
- [78] D. Bourell, B. Stucker, J. Obielodan, A. Ceylan, L. Murr, B. Stucker. Multi-material bonding in ultrasonic consolidation, *Rapid prototyping journal* 16 (2010) 180-188.
- [79] J. Obielodan, B. Stucker, E. Martinez, J. Martinez, D. Hernandez, D. Ramirez, L. Murr. Optimization of the shear strengths of ultrasonically consolidated Ti/Al 3003 dual-material structures, *Journal of Materials Processing Technology* 211 (2011) 988-995.
- [80] M. Sikorski. The adhesion of metals and factors that influence it, *Wear* 7 (1964) 144-162.
- [81] M. Sikorski. Correlation of the coefficient of adhesion with various physical and mechanical properties of metals, *Journal of Fluids Engineering* 85 (1963) 279-285.
- [82] R. Jahn, R. Cooper, D. Wilkosz. The effect of anvil geometry and welding energy on microstructures in ultrasonic spot welds of AA6111-T4, *Metallurgical and Materials Transactions A* 38 (2007) 570-583.

- [83] J. Goldstein, D.E. Newbury, P. Echlin, D.C. Joy, A.D. Romig Jr, C.E. Lyman, C. Fiori, E. Lifshin. Scanning electron microscopy and X-ray microanalysis: a text for biologists, materials scientists, and geologists, Springer Science & Business Media, 2012.
- [84] K. Kanaya, S. Okayama. Penetration and energy-loss theory of electrons in solid targets, *Journal of Physics D: Applied Physics* 5 (1972) 43.
- [85] J.E. Mueller, J.W. Gillespie, S.G. Advani. Effects of interaction volume on X-ray line-scans across an ultrasonically consolidated aluminum/copper interface, *Scanning* 35 (2013) 327-335.
- [86] A. Rollett, F. Humphreys, G.S. Rohrer, M. Hatherly. Recrystallization and related annealing phenomena, Elsevier, 2004.
- [87] F. Humphreys, Y. Huang, I. Brough, C. Harris. Electron backscatter diffraction of grain and subgrain structures—resolution considerations, *Journal of Microscopy* 195 (1999) 212-216.
- [88] D. Li, R.C. Soar. Plastic flow and work hardening of Al alloy matrices during ultrasonic consolidation fibre embedding process, *Materials Science and Engineering: A* 498 (2008) 421-429.
- [89] W.C. Oliver, G.M. Pharr. An improved technique for determining hardness and elastic modulus using load and displacement sensing indentation experiments, *Journal of materials research* 7 (1992) 1564-1583.
- [90] D. Schick, S. Suresh Babu, D.R. Foster, M. Dapino, M. Short, J.C. Lippold. Transient thermal response in ultrasonic additive manufacturing of aluminum 3003, *Rapid Prototyping Journal* 17 (2011) 369-379.
- [91] S. Mironov, Y. Sato, H. Kokawa. Microstructural evolution during friction stir-processing of pure iron, *Acta Materialia* 56 (2008) 2602-2614.

- [92] V. Nesterenko, M. Meyers, J. LaSalvia, M. Bondar, Y. Chen, Y. Lukyanov. Shear localization and recrystallization in high-strain, high-strain-rate deformation of tantalum, *Materials Science and Engineering: A* 229 (1997) 23-41.
- [93] Y. Xu, J. Zhang, Y. Bai, M.A. Meyers. Shear localization in dynamic deformation: microstructural evolution, *Metallurgical and materials transactions A* 39 (2008) 811-843.
- [94] Y. Xu, W. Zhong, Y. Chen, L. Shen, Q. Liu, Y. Bai, M. Meyers. Shear localization and recrystallization in dynamic deformation of 8090 Al–Li alloy, *Materials Science and Engineering: A* 299 (2001) 287-295.
- [95] Q. Wei, Z. Pan, X. Wu, B. Schuster, L. Kecskes, R. Valiev. Microstructure and mechanical properties at different length scales and strain rates of nanocrystalline tantalum produced by high-pressure torsion, *Acta Materialia* 59 (2011) 2423-2436.
- [96] Q. Wei, H. Zhang, B. Schuster, K. Ramesh, R. Valiev, L. Kecskes, R. Dowding, L. Magness, K. Cho. Microstructure and mechanical properties of super-strong nanocrystalline tungsten processed by high-pressure torsion, *Acta Materialia* 54 (2006) 4079-4089.
- [97] L.F. Trueb. Microstructural effects of heat treatment on the bond interface of explosively welded metals, *Metallurgical Transactions* 2 (1971) 145-153.
- [98] M. Kulakov, H.J. Rack. Surface damage during ultrasonic consolidation of 3003-H18 aluminum, *Rapid Prototyping Journal* 16 (2010) 12-19.
- [99] M. Kulakov, H.J. Rack. Control of 3003-H18 aluminum ultrasonic consolidation, *Journal of Engineering Materials and Technology* 131 (2009) 021006.
- [100] A.J. Schwartz, M. Kumar, B.L. Adams, D.P. Field. *Electron backscatter diffraction in materials science*, Springer, 2009.

- [101] D. Hughes, N. Hansen. High angle boundaries formed by grain subdivision mechanisms, *Acta materialia* 45 (1997) 3871-3886.
- [102] D. Rigney. Transfer, mixing and associated chemical and mechanical processes during the sliding of ductile materials, *Wear* 245 (2000) 1-9.
- [103] D. Rigney, L. Chen, M.G. Naylor, A. Rosenfield. Wear processes in sliding systems, *Wear* 100 (1984) 195-219.
- [104] C. Hopkins, M. Dapino, S. Fernandez. Statistical characterization of ultrasonic additive manufacturing Ti/Al composites, *Journal of Engineering Materials and Technology* 132 (2010) 041006.
- [105] T. Sakai, A. Belyakov, R. Kaibyshev, H. Miura, J.J. Jonas. Dynamic and post-dynamic recrystallization under hot, cold and severe plastic deformation conditions, *Progress in materials science* 60 (2014) 130-207.
- [106] D. Raabe, Z. Zhao, S.-J. Park, F. Roters. Theory of orientation gradients in plastically strained crystals, *Acta Materialia* 50 (2002) 421-440.
- [107] B. Hutchinson. Deformation microstructures and textures in steels, *Philosophical Transactions of the Royal Society of London A: Mathematical, Physical and Engineering Sciences* 357 (1999) 1471-1485.
- [108] J.-T. Park, J.A. Szpunar. Evolution of recrystallization texture in nonoriented electrical steels, *Acta Materialia* 51 (2003) 3037-3051.
- [109] S.H. Lee, D.N. Lee. Shear rolling and recrystallization textures of interstitial-free steel sheet, *Materials Science and Engineering: A* 249 (1998) 84-90.

- [110] C.S. Zhang, A. Deceuster, L. Li. A method for bond strength evaluation for laminated structures with application to ultrasonic consolidation, *Journal of materials engineering and performance* 18 (2009) 1124-1132.
- [111] P. Wolcott, N. Sridharan, S. Babu, A. Miriyev, N. Frage, M. Dapino. Characterisation of Al-Ti dissimilar material joints fabricated using ultrasonic additive manufacturing, *Science and Technology of Welding and Joining* (2015) 1362171815Y. 0000000072.
- [112] K. Lücke, O. Engler. Effects of particles on development of microstructure and texture during rolling and recrystallisation in fcc alloys, *Materials Science and Technology* 6 (1990) 1113-1130.
- [113] H.W. Kim, S.B. Kang, N. Tsuji, Y.M. Amino. Deformation textures of AA8011 aluminum alloy sheets severely deformed by accumulative roll bonding, *Metallurgical and Materials Transactions A* 36 (2005) 3151-3163.
- [114] W.-B. Lee, M. Schmuecker, U.A. Mercardo, G. Biallas, S.-B. Jung. Interfacial reaction in steel–aluminum joints made by friction stir welding, *Scripta Materialia* 55 (2006) 355-358.
- [115] P. Prangnell, F. Haddadi, Y. Chen. Ultrasonic spot welding of aluminium to steel for automotive applications-microstructure and optimisation, *Materials Science and Technology* 27 (2011) 617-624.
- [116] E. Taban, J.E. Gould, J.C. Lippold. Dissimilar friction welding of 6061-T6 aluminum and AISI 1018 steel: Properties and microstructural characterization, *Materials & design* 31 (2010) 2305-2311.
- [117] Y. Zhang. Investigation of magnetic pulse welding on lap joint of similar and dissimilar materials. The Ohio State University, 2010.

- [118] H. Danesh Manesh, A. Karimi Taheri. Study of mechanisms of cold roll welding of aluminium alloy to steel strip, *Materials science and technology* 20 (2004) 1064-1068.
- [119] T. Monaghan, A.J. Capel, S. Christie, R. Harris, R.J. Friel. Solid-state additive manufacturing for metallized optical fiber integration, *Composites Part A: Applied Science and Manufacturing* 76 (2015) 181-193.
- [120] M. Miller, D. Hoelzer, E. Kenik, K. Russell. Stability of ferritic MA/ODS alloys at high temperatures, *Intermetallics* 13 (2005) 387-392.
- [121] M. Miller, K. Russell, D. Hoelzer. Characterization of precipitates in MA/ODS ferritic alloys, *Journal of nuclear Materials* 351 (2006) 261-268.
- [122] D. Larson, P. Maziasz, I. Kim, K. Miyahara. Three-dimensional atom probe observation of nanoscale titanium-oxygen clustering in an oxide-dispersion-strengthened Fe-12Cr-3W-0.4 Ti+ Y 2 O 3 ferritic alloy, *Scripta Materialia* 44 (2001) 359-364.
- [123] M. Miller, E. Kenik, K. Russell, L. Heatherly, D. Hoelzer, P. Maziasz. Atom probe tomography of nanoscale particles in ODS ferritic alloys, *Materials Science and Engineering: A* 353 (2003) 140-145.
- [124] M.K. Miller. Atom probe tomography: analysis at the atomic level, Springer Science & Business Media, 2012.
- [125] A. Hirata, T. Fujita, Y. Wen, J. Schneibel, C.T. Liu, M. Chen. Atomic structure of nanoclusters in oxide-dispersion-strengthened steels, *Nature materials* 10 (2011) 922-926.
- [126] C.L. Fu, M. Krčmar, G.S. Painter, X.-Q. Chen. Vacancy mechanism of high oxygen solubility and nucleation of stable oxygen-enriched clusters in Fe, *Physical review letters* 99 (2007) 225502.

- [127] G. Cantin, S. David, W. Thomas, E. Lara-Curzio, S. Babu. Friction Skew-stir welding of lap joints in 5083–0 aluminium, *Science and Technology of Welding & Joining* 10 (2005) 268-280.
- [128] A.Y. Yermakov, V. Gapontzev, V. Kondratyev, Y.N. Gornostyrev, M.A. Uimin, A.Y. Korobeinikov. Phase instability of nanocrystalline driven alloys. *Journal of Metastable and Nanocrystalline Materials*, vol. 8: Trans Tech Publ, 2000. p.577-584.
- [129] R. Kirchheim. Reducing grain boundary, dislocation line and vacancy formation energies by solute segregation: II. Experimental evidence and consequences, *acta materialia* 55 (2007) 5139-5148.
- [130] R. Kirchheim. Reducing grain boundary, dislocation line and vacancy formation energies by solute segregation. I. Theoretical background, *Acta Materialia* 55 (2007) 5129-5138.
- [131] R. Kirchheim. Grain coarsening inhibited by solute segregation, *Acta Materialia* 50 (2002) 413-419.
- [132] F. Tang, D. Gianola, M. Moody, K. Hemker, J. Cairney. Observations of grain boundary impurities in nanocrystalline Al and their influence on microstructural stability and mechanical behaviour, *Acta Materialia* 60 (2012) 1038-1047.

Appendix

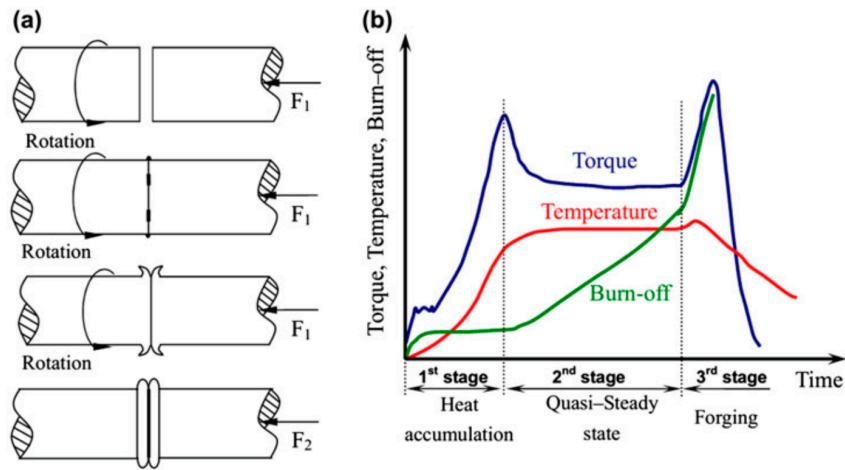


Figure 1.1 Typical continuous drive friction welding process (a) schematic showing fundamental steps and (b) plot of selected parameters versus time

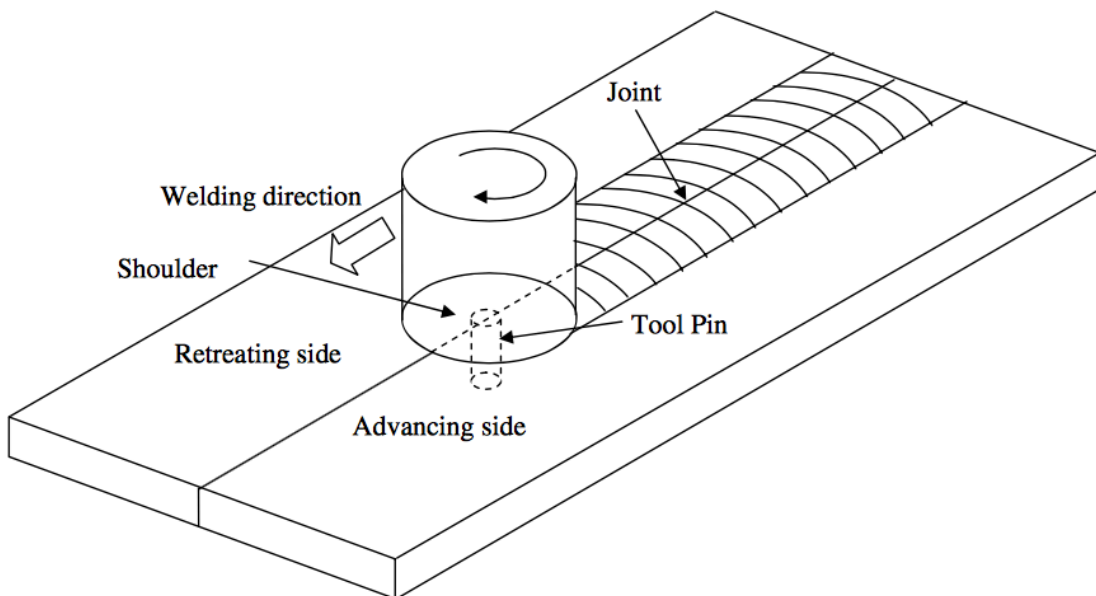


Figure 1.2 Schematic of friction stir welding process showing advancing and retreating side

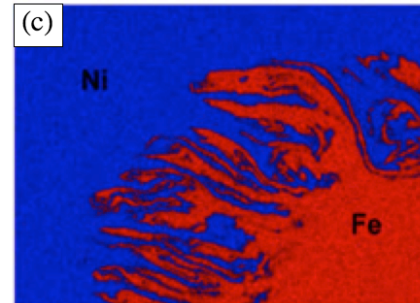
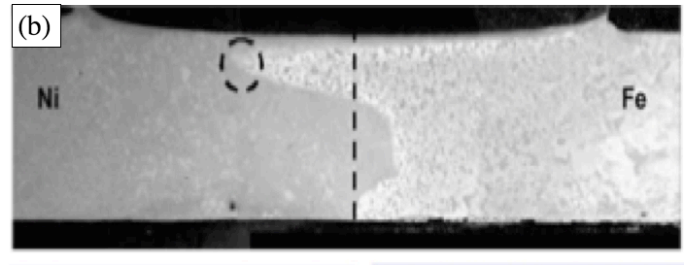
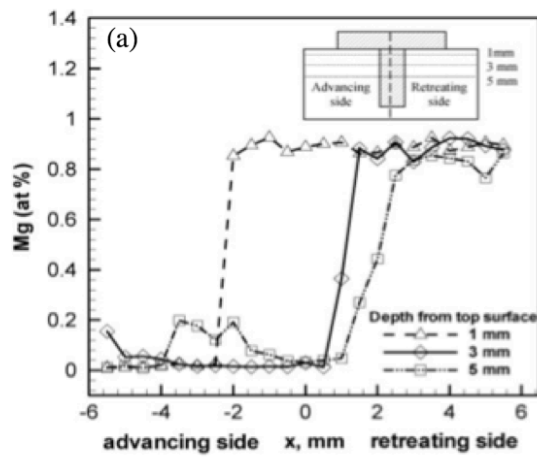


Figure 1.3 Experimentally determined concentration profiles of Mg at various depths across the weld center line for AA 1200 (advancing) and AA 6061 (retreating side) (b) Macrograph shows Fe and Ni in a transverse section illustrating the similar observation noted in (a) (c) Show the EDS data in the marked region in figure (b)

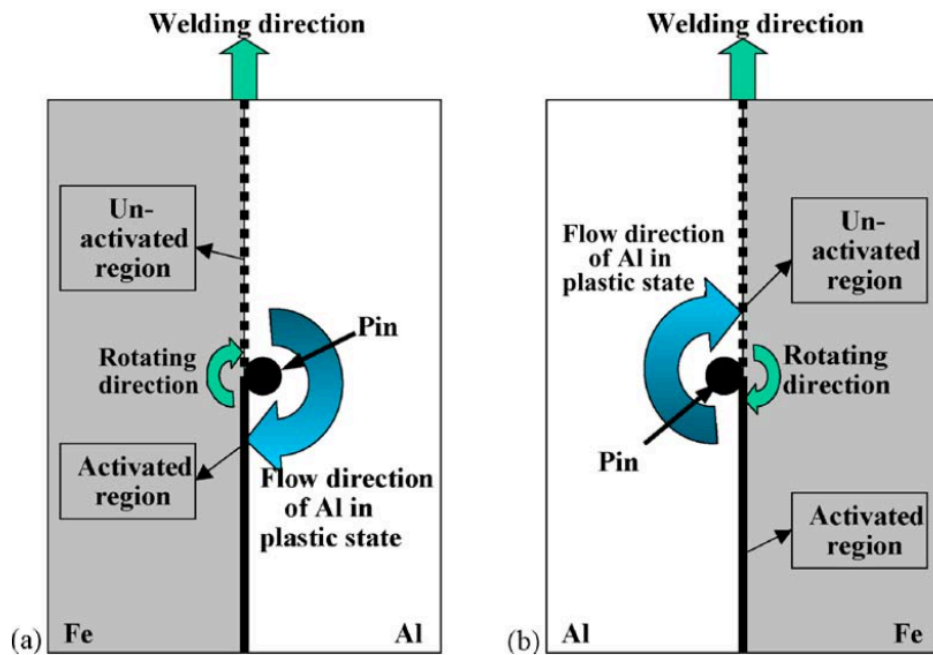


Figure 1.4 Schematic illustration explaining the reason why the counterclockwise rotation of a pin cannot weld aluminum to steel: (a) clockwise rotation of a pin where the Al is transferred to the steel surface where the oxide has been removed resulting in a complete weld and (b) counterclockwise rotation of a pin where the Al is deposited on the side of the steel where the oxide layer is not removed by the action of the tool and hence welding is not complete. Note that in both the cases the steel is in the advancing side and the Al is in the retreating side but the direction of rotation plays a major role in determining if bonding occurs

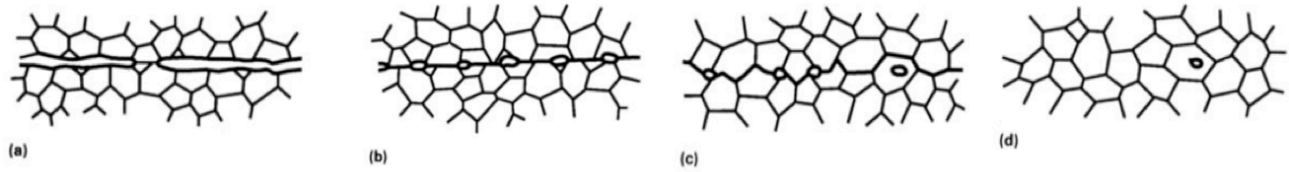


Figure 1.5 Sequence of metallurgical stages in diffusion bonding process (a) initial contact: limited to a few asperities (room temperature) (b) First stage deformation of surface asperities by plastic flow and creep (c) Second stage: grain boundary diffusion of atoms to voids and grain boundary migration (d) Third stage Volume diffusion of atoms to the voids

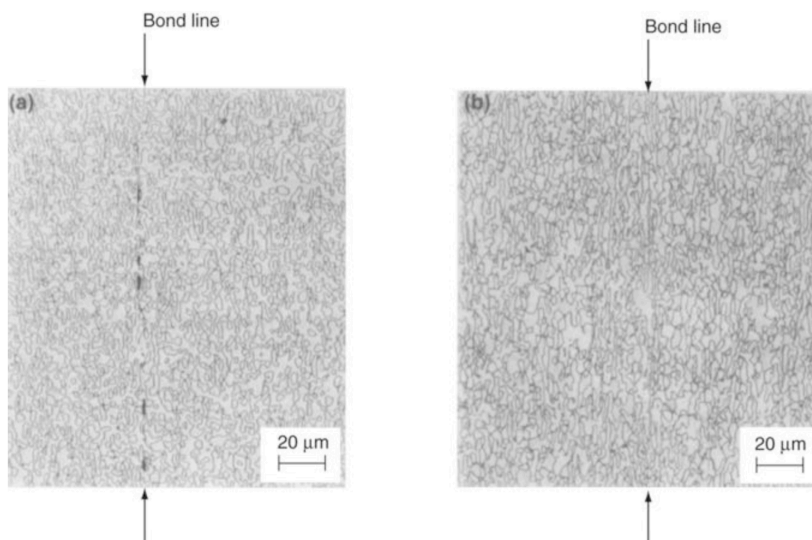


Figure 1.6 Effect of pressure on void formation of a titanium alloy diffusion bonded at temperatures of 980°C for 2 hours (a) Incomplete bond at 7.0 MPa (b) Complete bond at 10.0 MPa

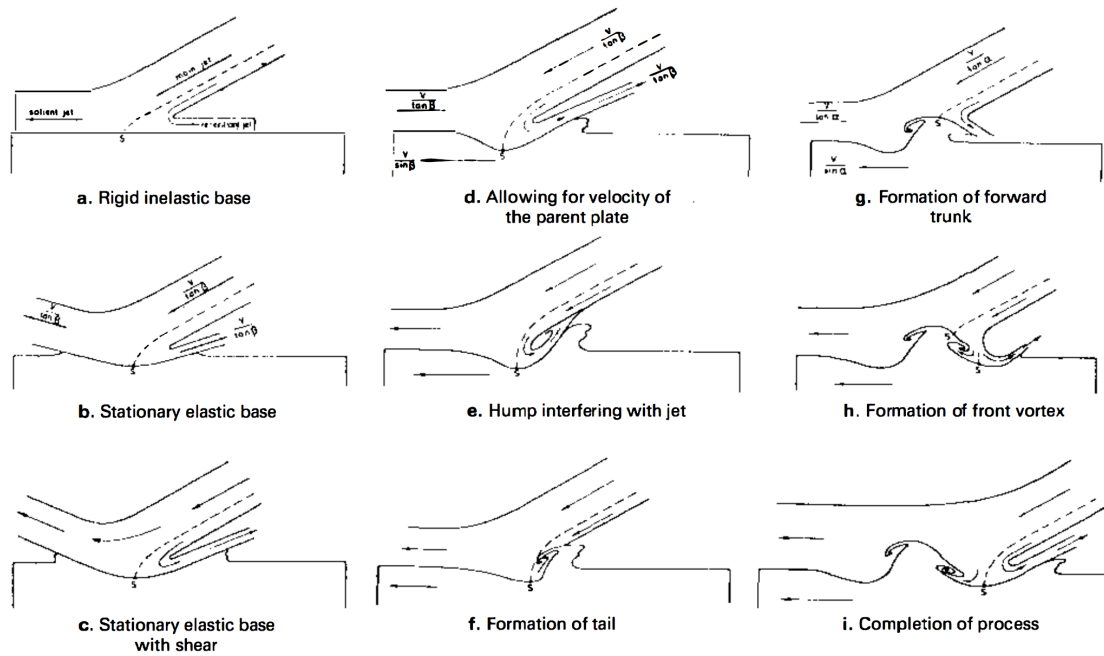


Figure 1.7 Illustration of the wave formation process in explosion welding but can be applied to any high impact welding. The jetting process illustrated is key to the bond formation mechanism in explosively welded components



Figure 1.8 Shows the bright filed image on dislocation interaction and the cellular structure in AA6061 joint. The beam is along the [001]. The dislocation interaction at the grain interior where the grains were ~1micon away from the interface

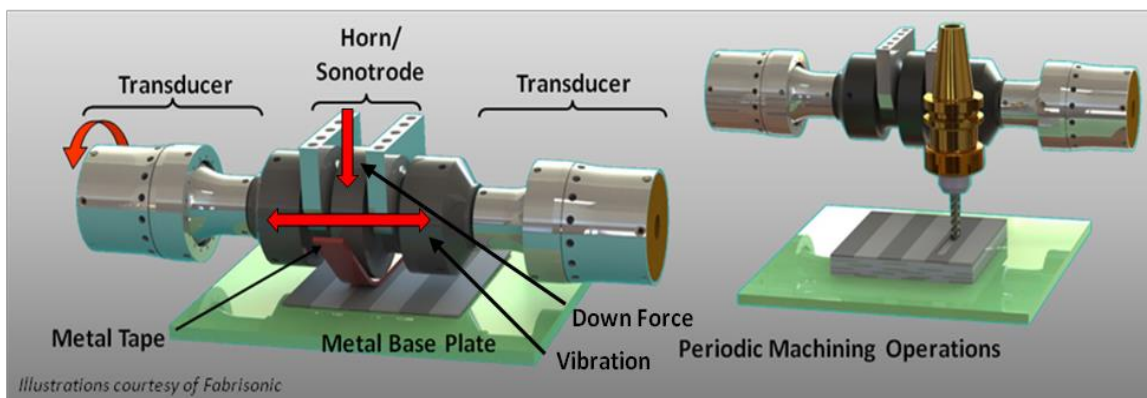


Figure 2.1 Showing the UAM process

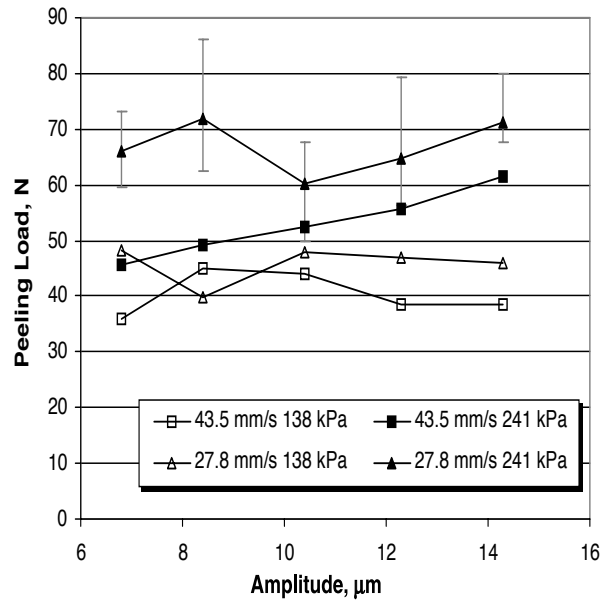


Figure 2.2 Peel test data showing the effect of process parameters. Note that decreasing travel speed and increasing the amplitude has the same effect

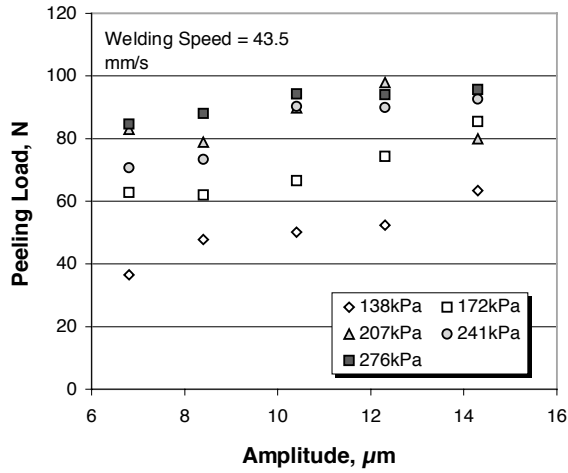
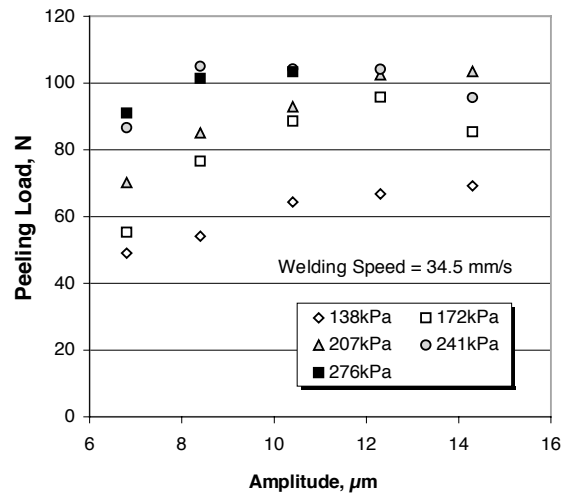


Figure 2.3 Effect of process parameters on bond strength for Al3003 note the influence of travel speed

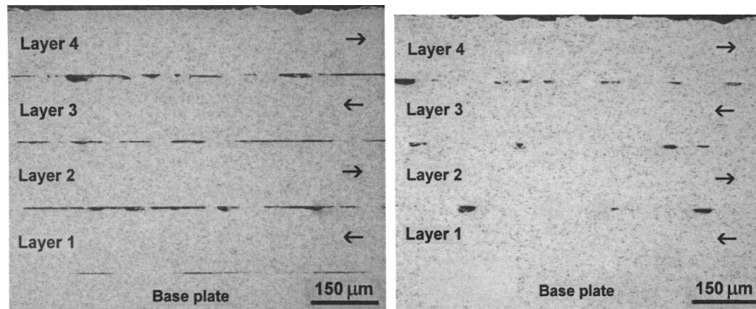


Figure 2.4 Increase in the vibration amplitude from 10 to 16 and increasing the preheat to ~150°C helped increase the LWD significantly

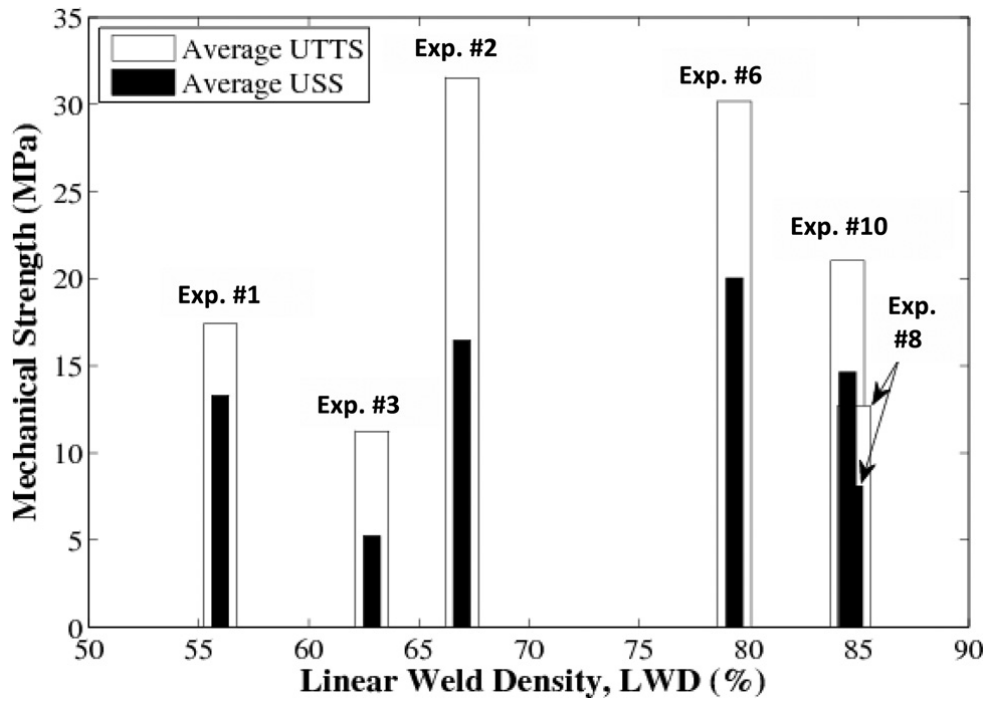


Figure 2.5 Results from the shear test showing no correlation between LWD and mechanical properties

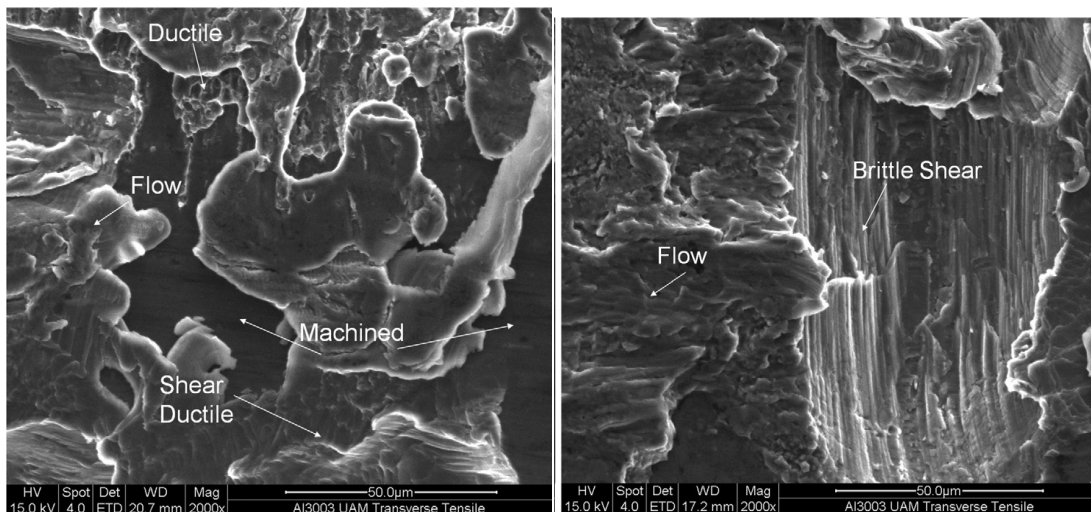


Figure 2.6 Fractographs of both the specimens (a) High LWD and low strength showing no metallurgical bonding (b) Lower LWD and higher strength with metallurgical bonding

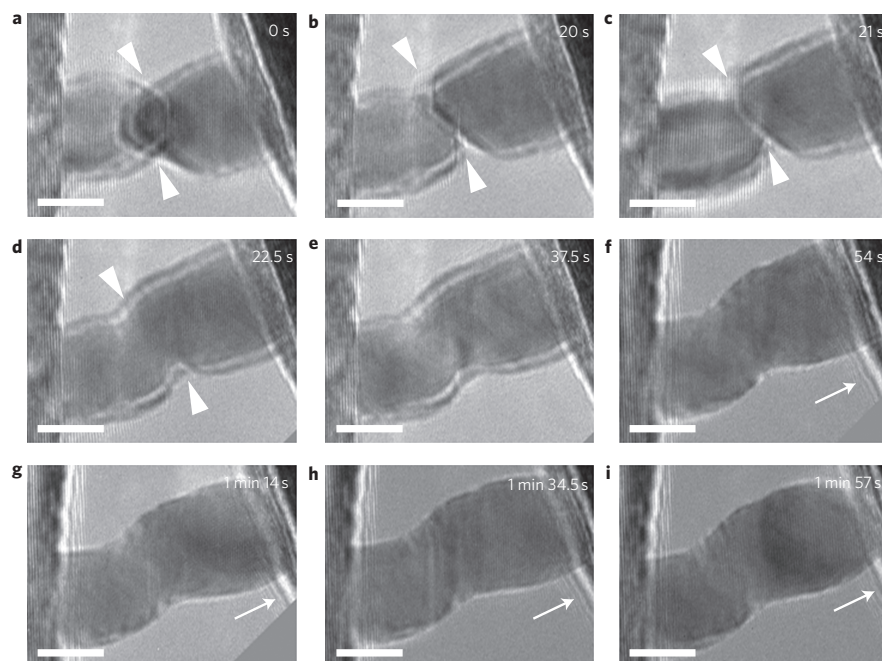


Figure 2.7 Welding of two gold Nano rods (a,b) One Nano rod (right) is caused to approach another (left) until their front surfaces come into contact. c–e, The welding process is completed within $\square 1.5$ s (c-d) followed by structure relaxation (d-e). (f–i) After withdrawal of the STM probe (f–i), the as-welded nanowire is left in the free-standing state (i). Triangles indicate the front edges of the two Nano rods. Arrows indicate the withdrawing direction of the STM probe. Scale bars, 5 nm.

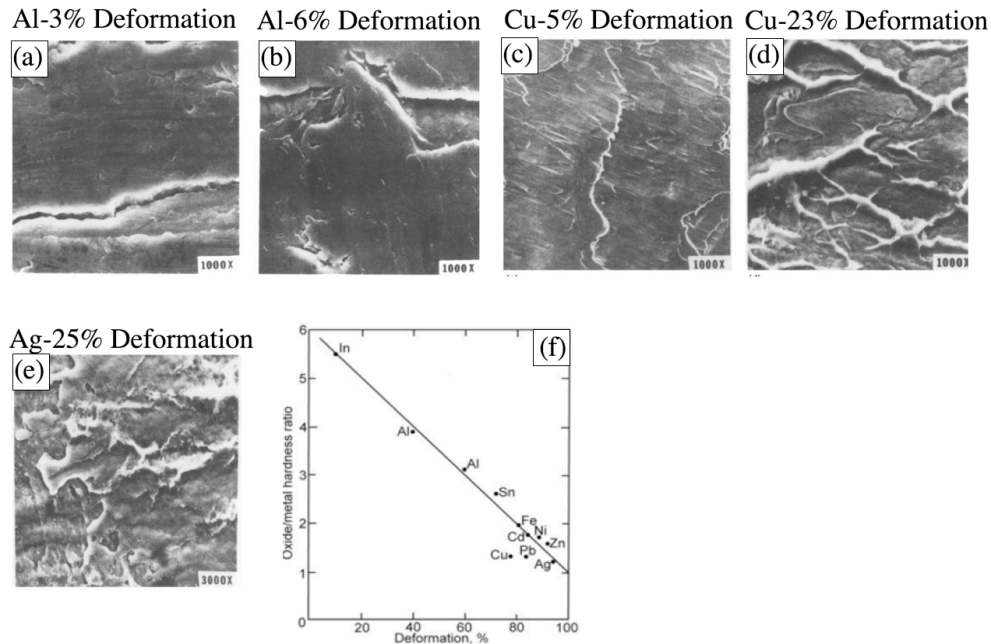


Figure 2.8 This indicates the fact that a threshold needs to be overcome to bond surfaces together. Fractographs of the faying surfaces of cold pressure welded Al, Cu and Ag at sub bonding strains. The strain was sufficient to cause oxide film rupture. The percentage deformations for various metals and the ratio of the oxide to metal is shown in figure 2.8(d)

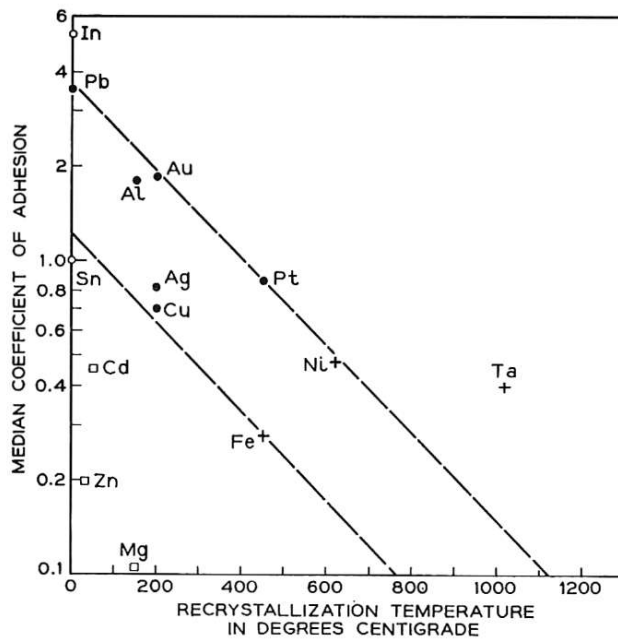


Figure 2.9 Adhesion between metals increase with decrease in the recrystallization temperature. It was also observed that at higher temperatures the metals could be joined at lower deformations

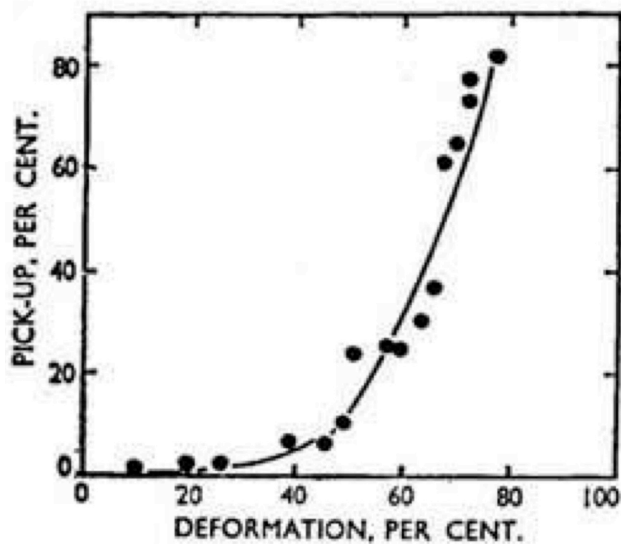


Figure 2.10 Adhesion increases with plastic deformation

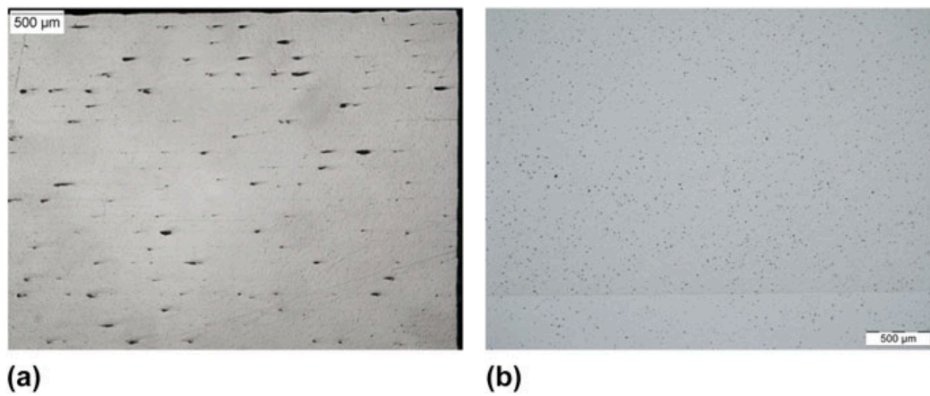


Figure 2.11 Comparison of builds fabricated with the (a) low power UAM (b) High power 9kW UAM processes

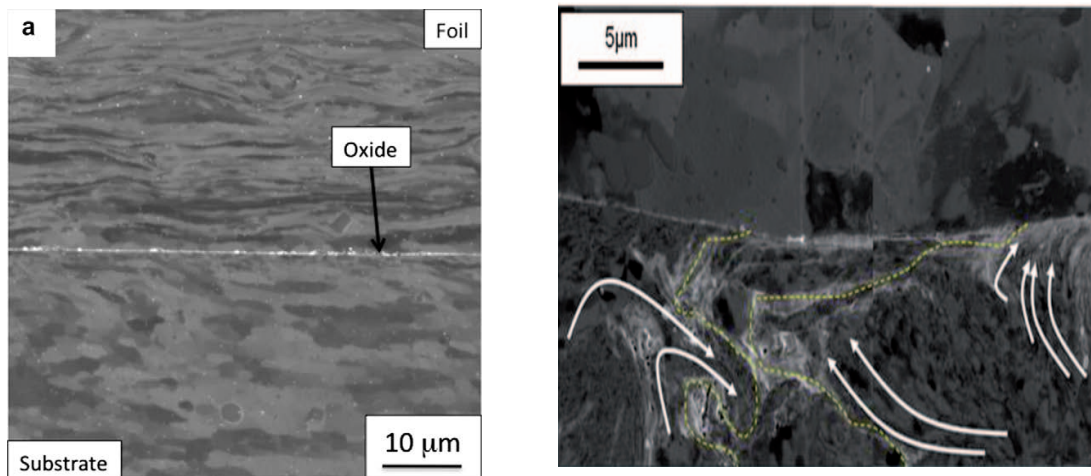


Figure 2.12 (a) Bonded interface shows continuous oxide layers. Dashed lines show possible interfaces of a pre-process asperity. White 'flow' lines indicate the possible directionality of the plastic deformation

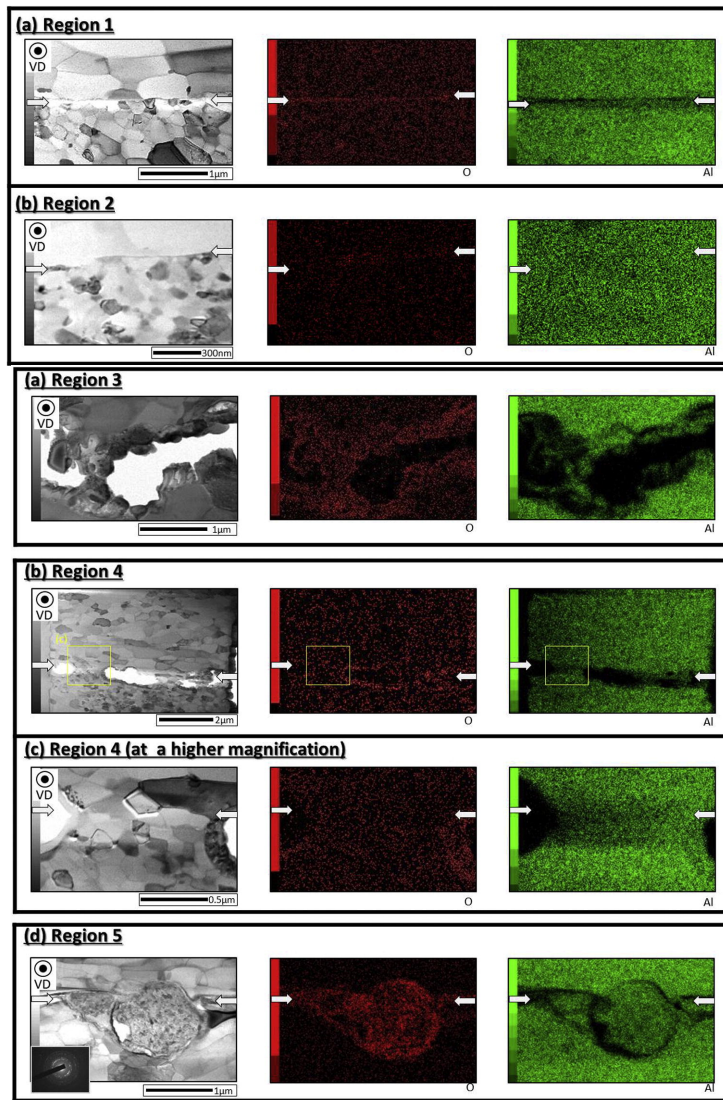


Figure 2.13 Shows the ‘dumping’ of the oxide layers in the voids (Shimzu et.al,2014)

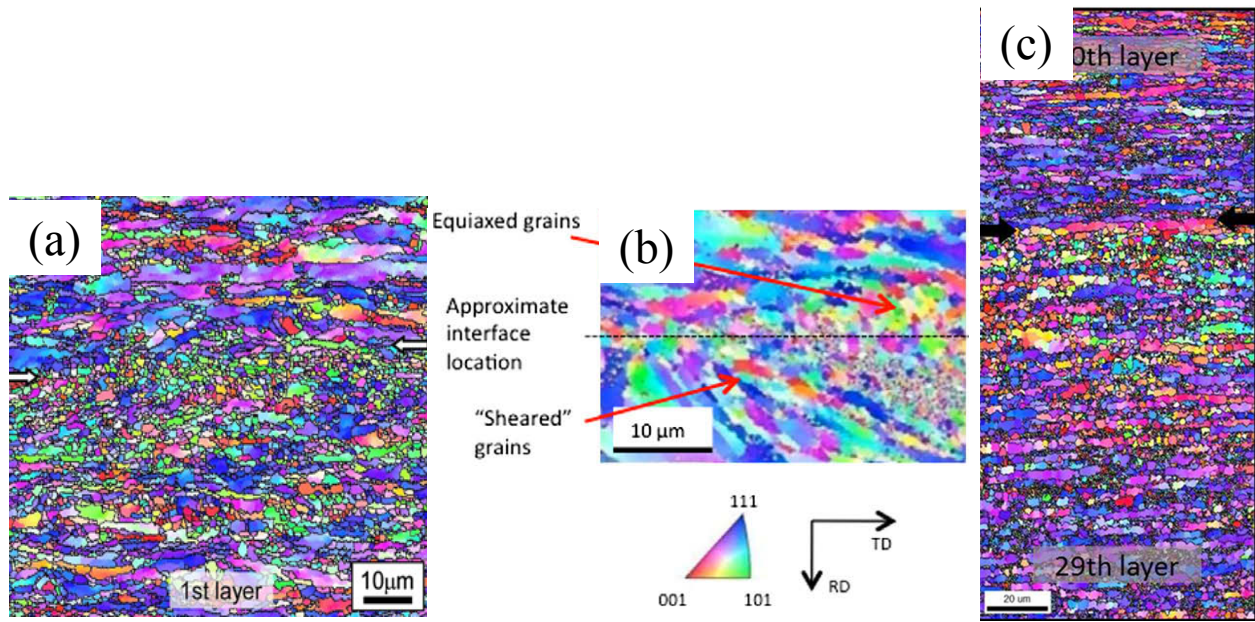


Figure 2.14 Interface showing grain refinement in Al-3003 (b)Interface showing grain refinement in Cu alloys (c) Interface showing grain refinement in Al-6061

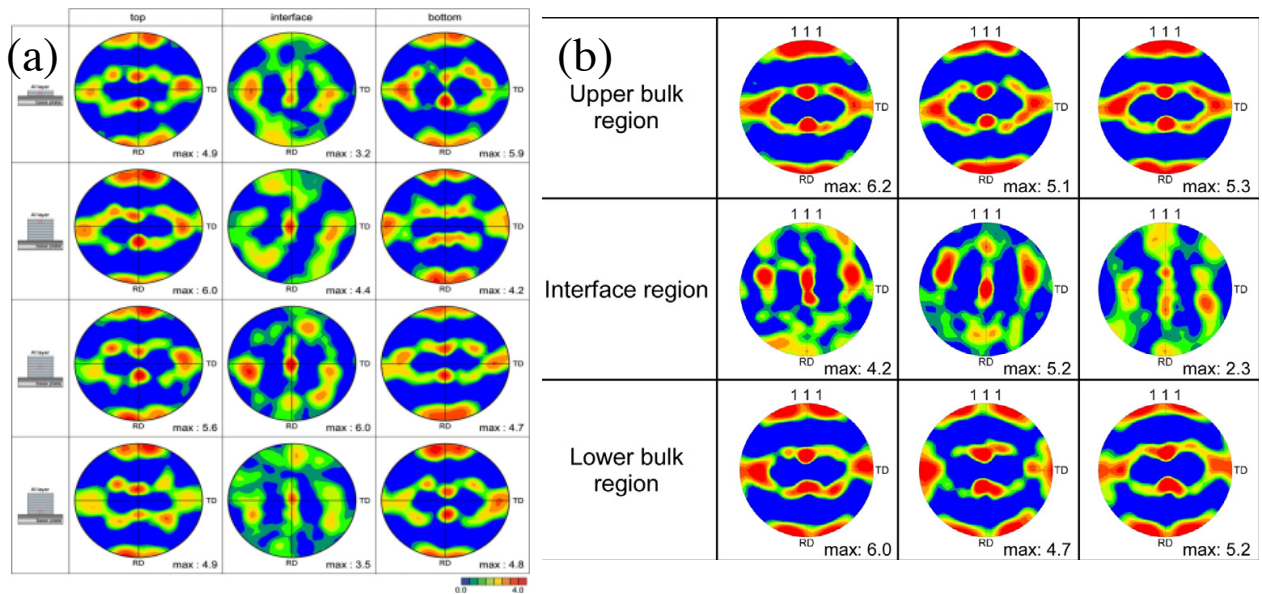


Figure 2.15 (a) Comparing textures at different regions of the build (b)Comparing textures at different regions of the build in Al-6061

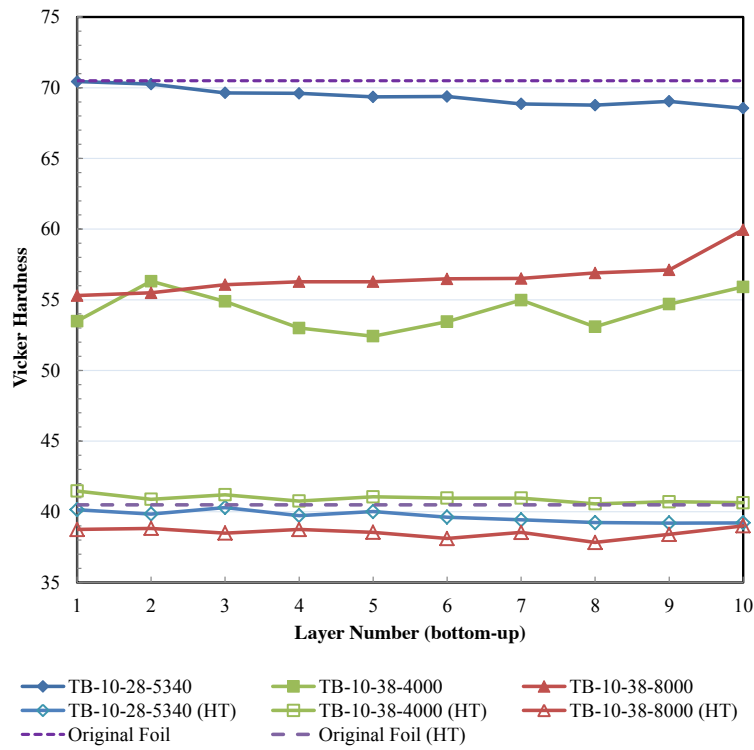


Figure 2.16 Variation of hardness across the interfaces. The drop in hardness while welding at higher amplitudes was attributed to softening due to adiabatic heating. Note that there is no significant change in hardness when the normal load is increased.

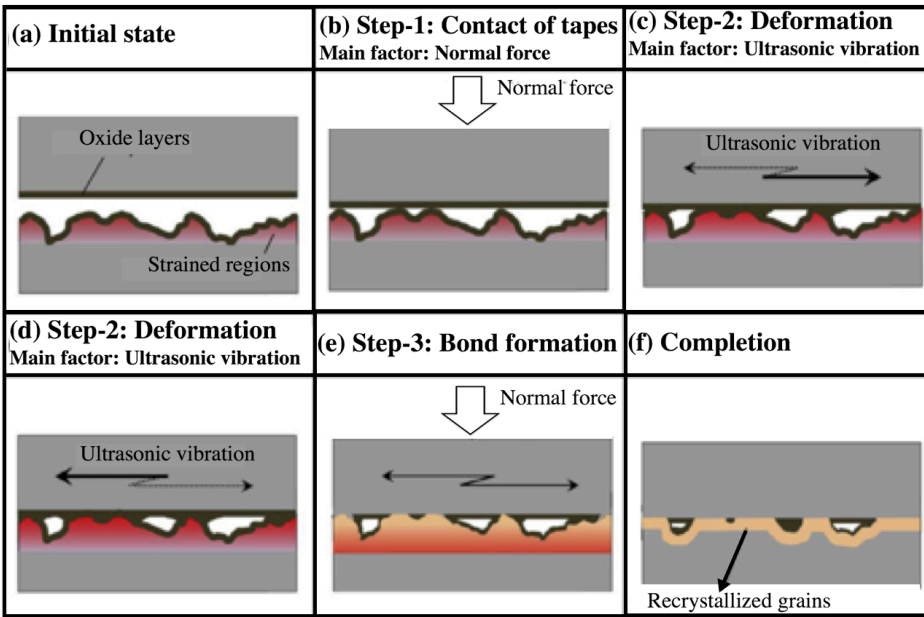


Figure 2.17 illustrating the bond formation steps involved in ultrasonic additive manufacturing

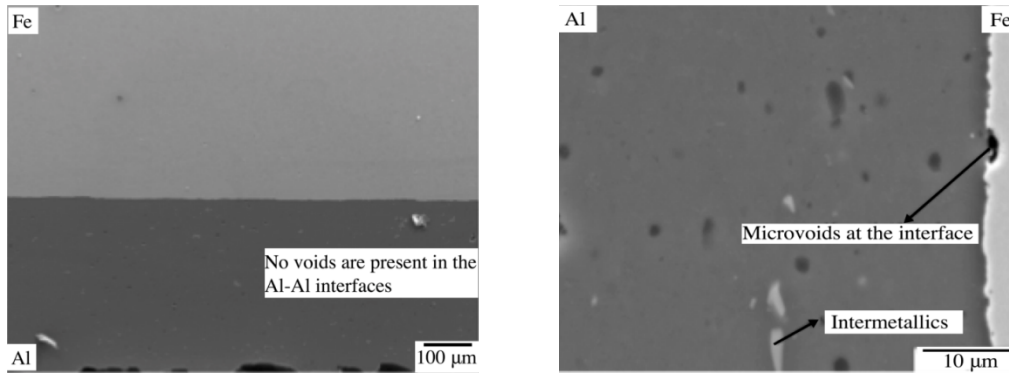


Figure 5.1 (a) (b) shows the SEM image of the interface showing continuous bond formation at the interface

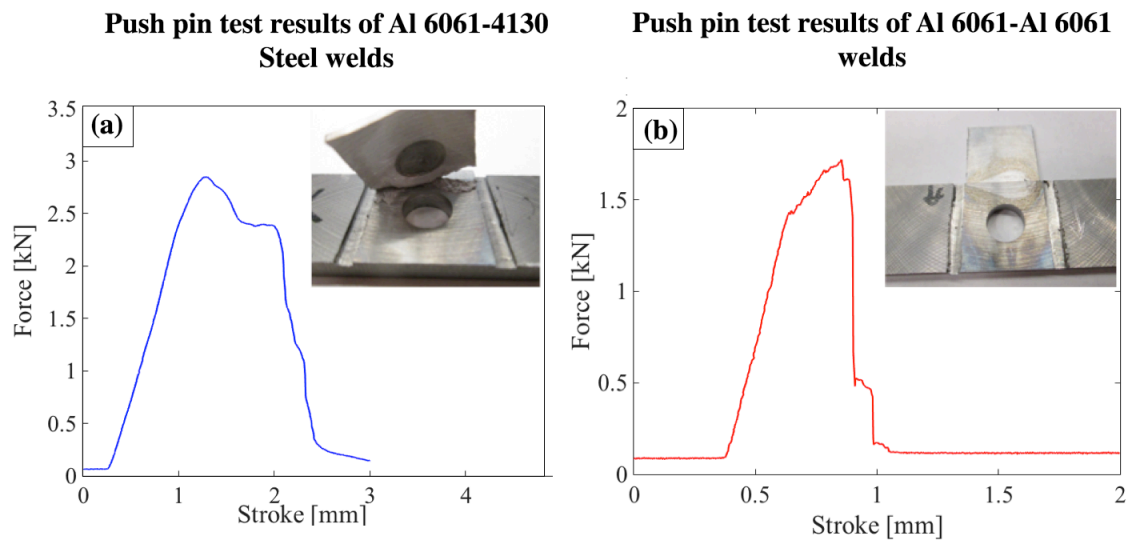


Figure 5.2 Shows the results from the push pin tests (a) The push pin cure for the Al-Steel sample (b) Push pin test on the Al-Al weld Note the difference in the failure morphology. The Al-Steel weld fails by a shear while the Al-Al fails by de-bonding

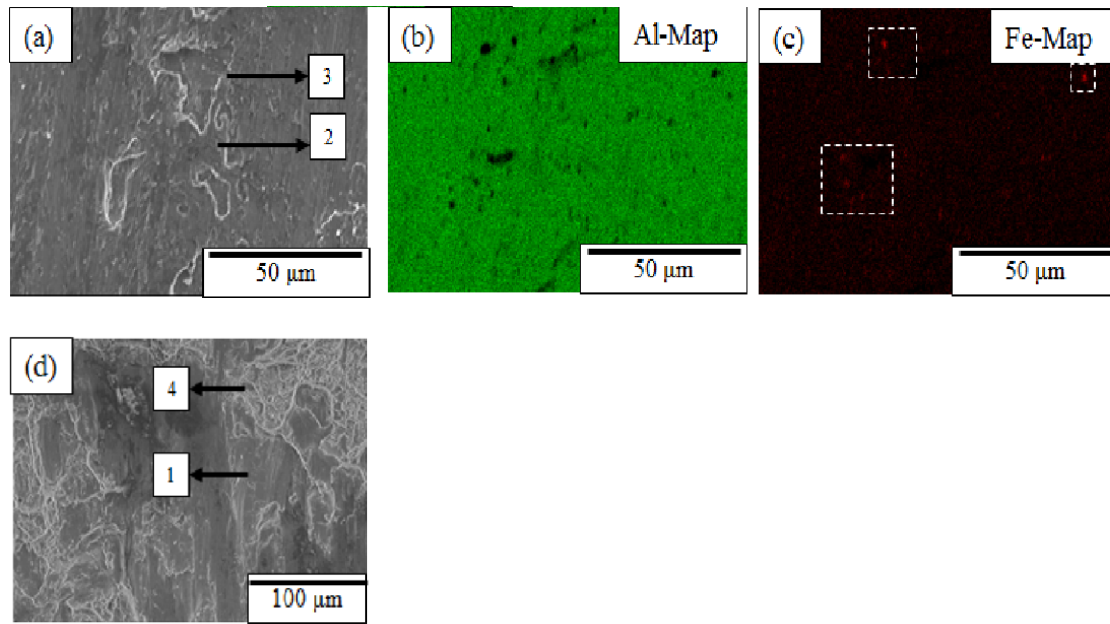


Figure 5.3 Shows the SEM image of the fracture surfaces. (a) and (d) Shows the fractography of the failed surfaces. Where 1-4 corresponds to machined, shear, shear brittle, shear ductile, and ductile respectively. Details on the nomenclature of these terms are found in [refer] (b) and (c) Show the EDS maps of the fracture surfaces. Note the localized regions showing concentration of Fe indicative of material transfer

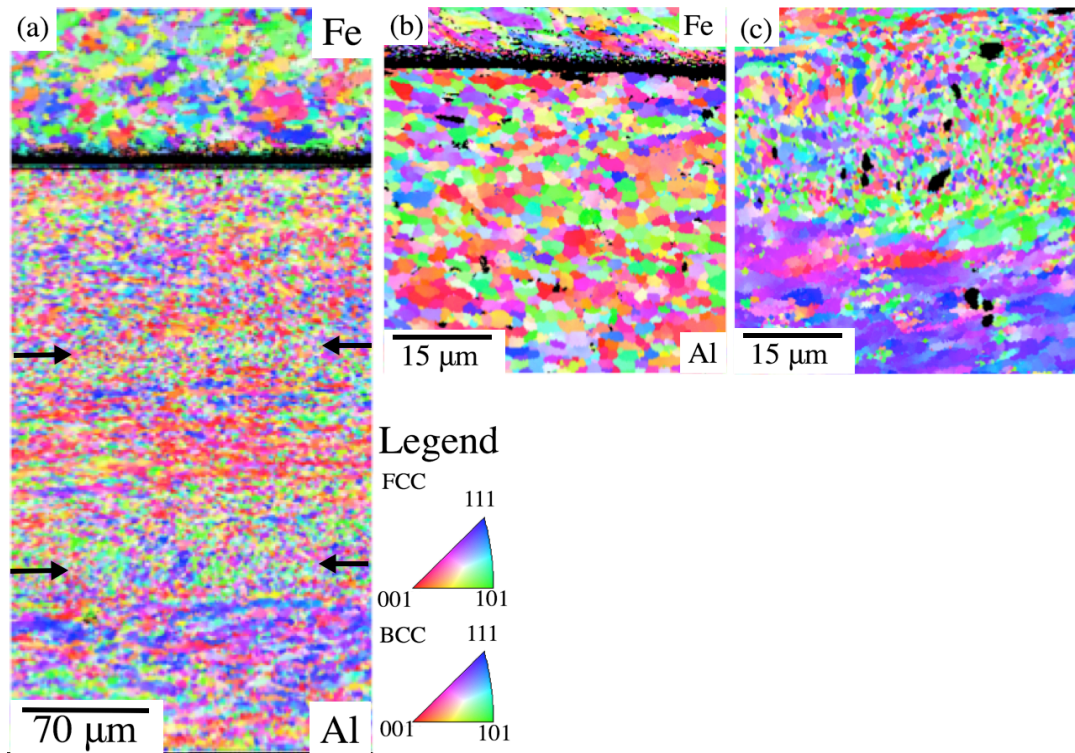


Figure 5.4 Shows the electron backscatter diffraction (a) Al-Steel build across 3 Al layers (b) Al-Steel interface at high magnification showing extensive deformation only in the Al (c) Al-Al interface showing deformation on both the sides of the interface

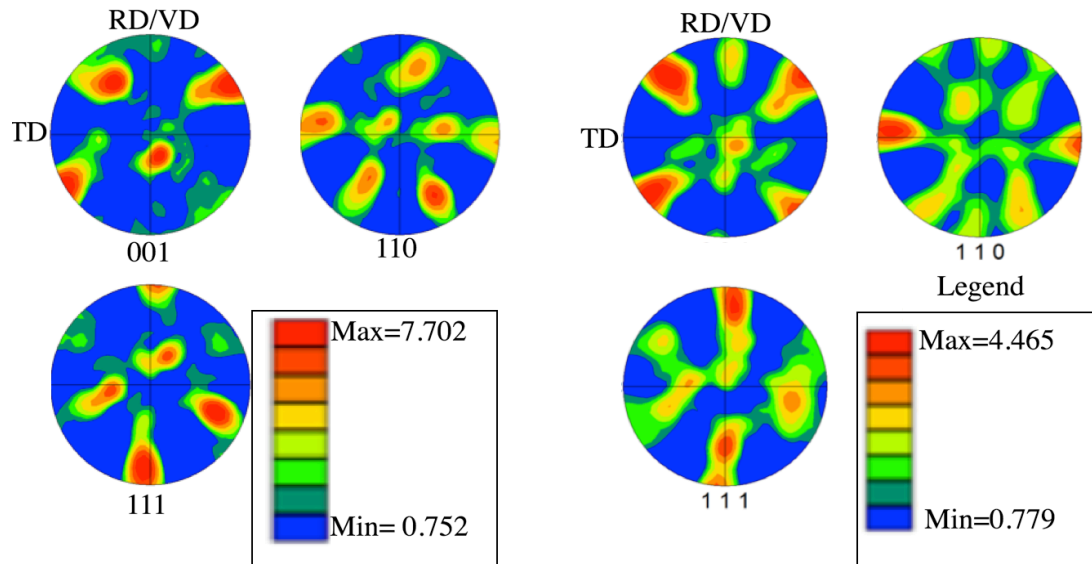


Figure 5.5 Shows the pole figures obtained from (a) Al-Steel dissimilar interface (b) Al-Al Similar interface. Note that in both the cases the Al shows a rotated cube texture. Also note that the texture strengths are different with the Al-Al showing a weaker texture while the Al-Steel interface shows a stronger texture

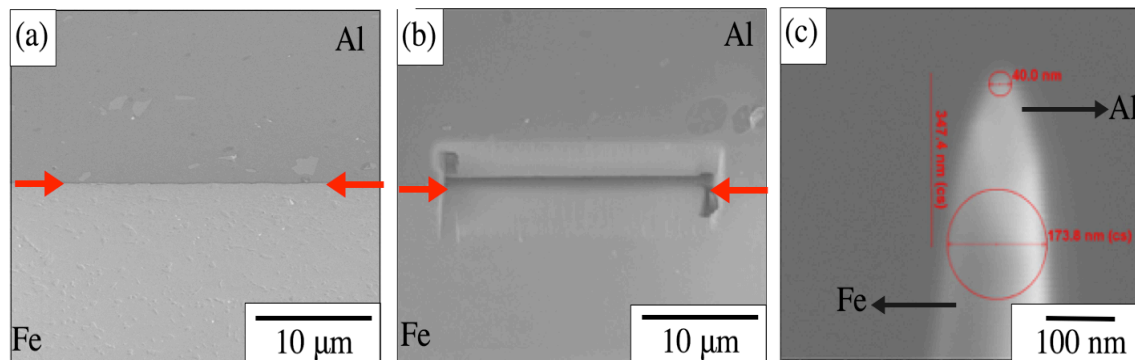


Figure 5.6 Shows the (a) Interface where bonding was complete (b) Region where sample extraction was performed (c) Tip after sharpening and polishing used for the analysis

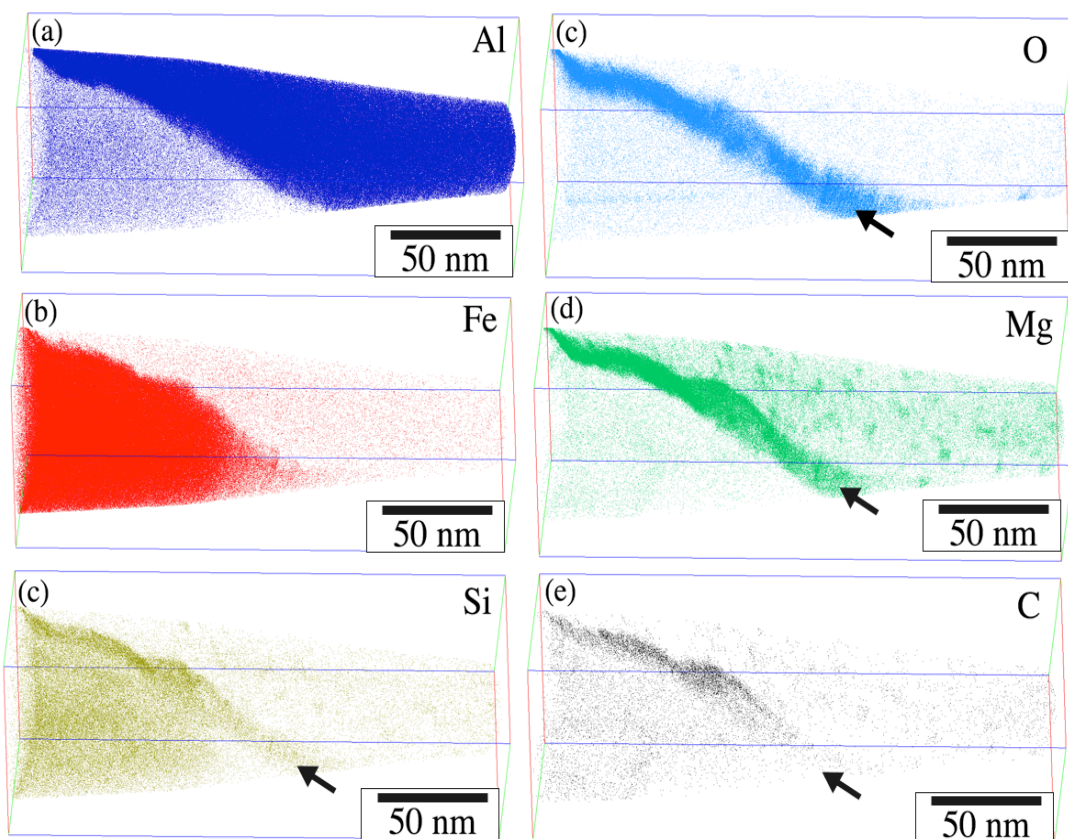


Figure 5.7 Shows the reconstructed tips showing (a) Distribution of Al (b) distribution of Fe (c) Si distribution (d) O distribution (e) Mg distribution (f) C distribution. The respective interfaces are marked using arrows

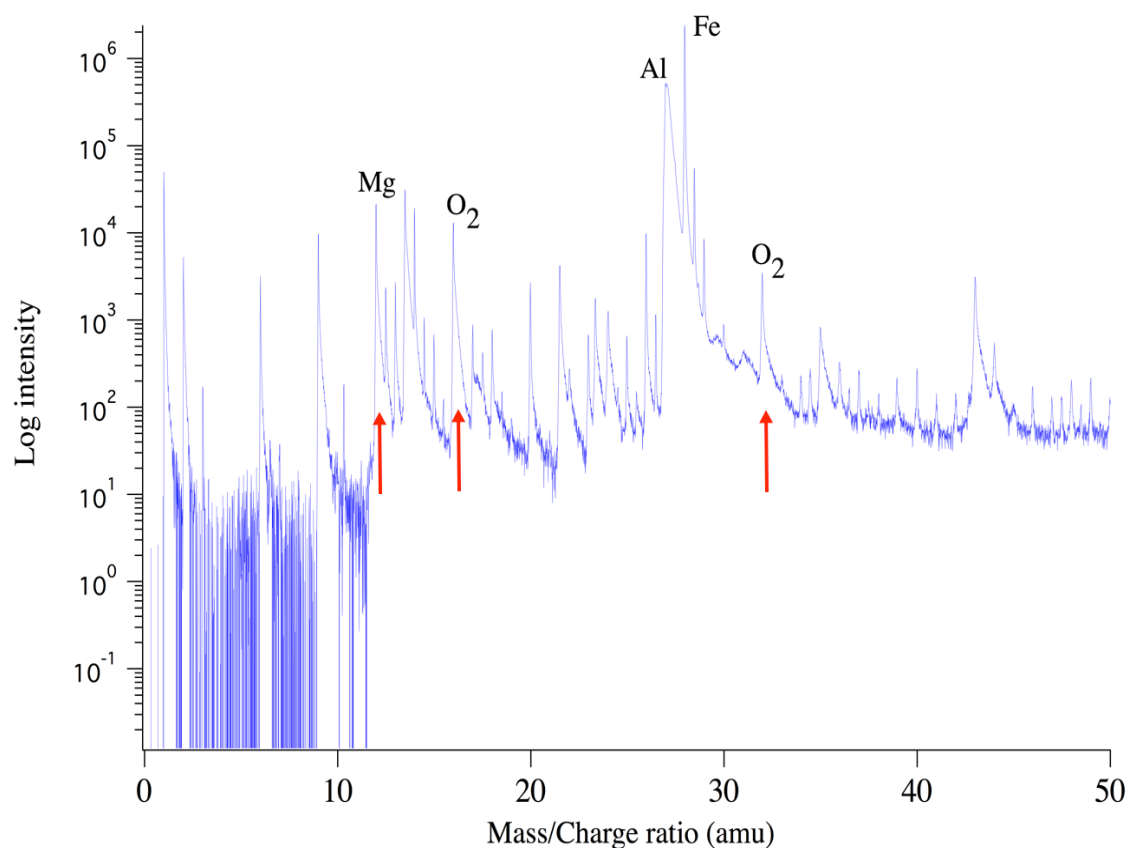


Figure 5.8 Shows the presence of Oxygen peaks at 16 and 32 respectively confirming the presence of elemental oxygen at the interface

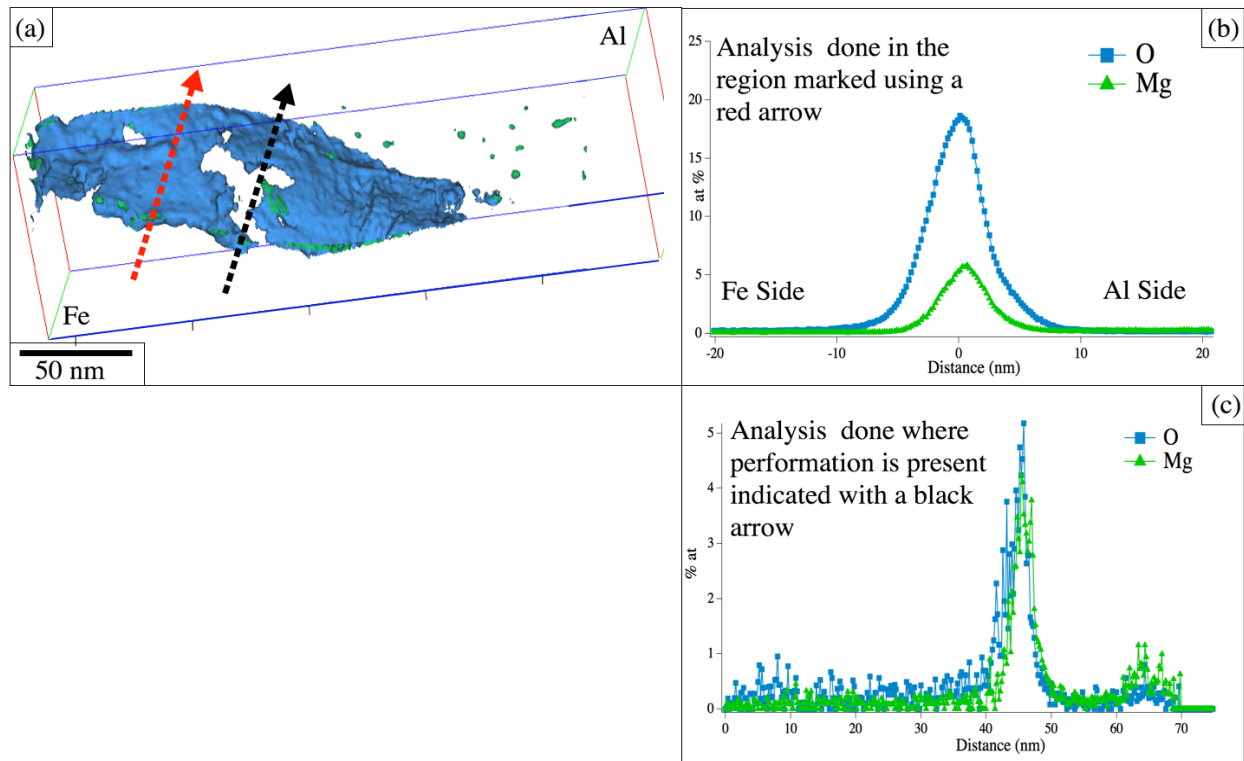


Figure 5.9 (a) shows the 6% Mg and Oxygen iso surface. Note the region marked using the black arrow indicating a region where there appears to be a local perforation in the oxide film (b) Shows Proxigram analysis performed along the direction marked using the red arrow (c) Shows the Proxigram analysis performed along the direction marked using the black arrow. Note that there is still considerable ~ 5 at% oxygen present in the region

Table-5.1 Average grain size in the CP-Ti

| Layer | Grain size (μm) |
|-------------|------------------------------|
| As received | 17.27 microns |
| Layer-1 | 7.24 microns |
| Layer-2 | 8.2 microns |
| Layer-3 | 7.3 microns |

Table-5.2 Average grain size in the CP-Ti

| Layer | Grain Size (μm) |
|-------------|------------------------------|
| As received | 5.4526 |
| Layer-1 | 5.3921 |
| Layer-2 | 5.3214 |
| Layer-3 | 5.27059 |

Table-5.3: Average misorientation in Al-1100

| Layer | Misorientation |
|---------|----------------|
| Layer-1 | 23.14 degree |
| Layer-2 | 22.98 degree |
| Layer-3 | 26.45 degree |

Table-5.4: Average misorientation in CP-Ti

| Layer | Misorientation |
|---------|----------------|
| Layer-1 | 49.8589 |
| Layer-2 | 44.9578 |
| Layer-3 | 41.6656 |

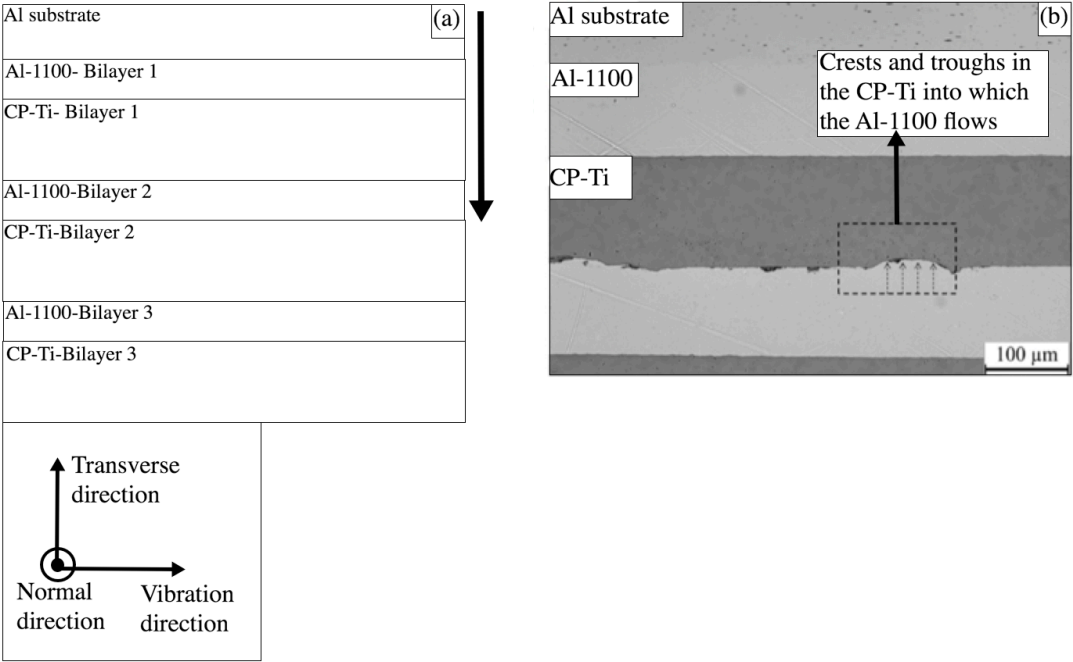


Figure 6.1 (a) showing the schematic of the bilayer arrangement used to fabricate the build (b) Showing the optical micrograph of the build. The Substrate and the first bilayer. Note the regions where the Al-1100 flowed into the asperities created in the CP-Ti by the sonotrode

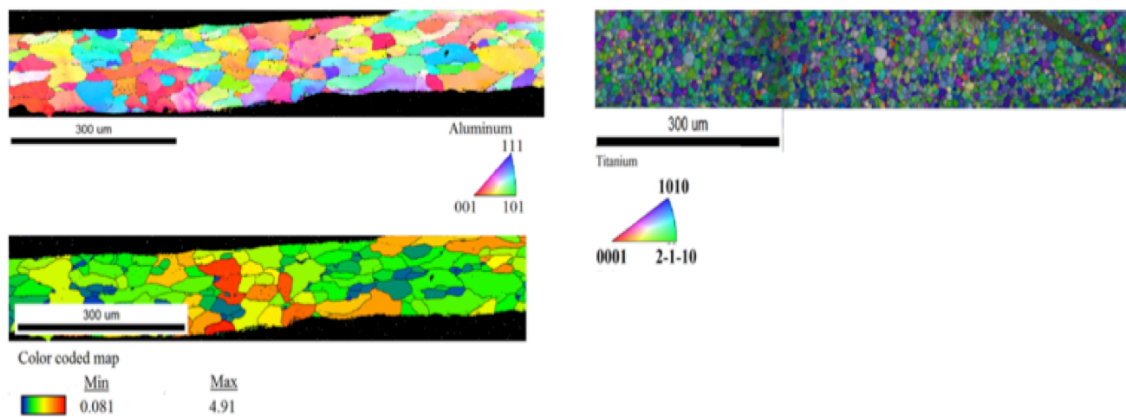


Figure 6.2 (a) IPF of as received Al-1100 (b) grain orientation spread of the Al-1100 sample (c) IPF of the as received titanium foil

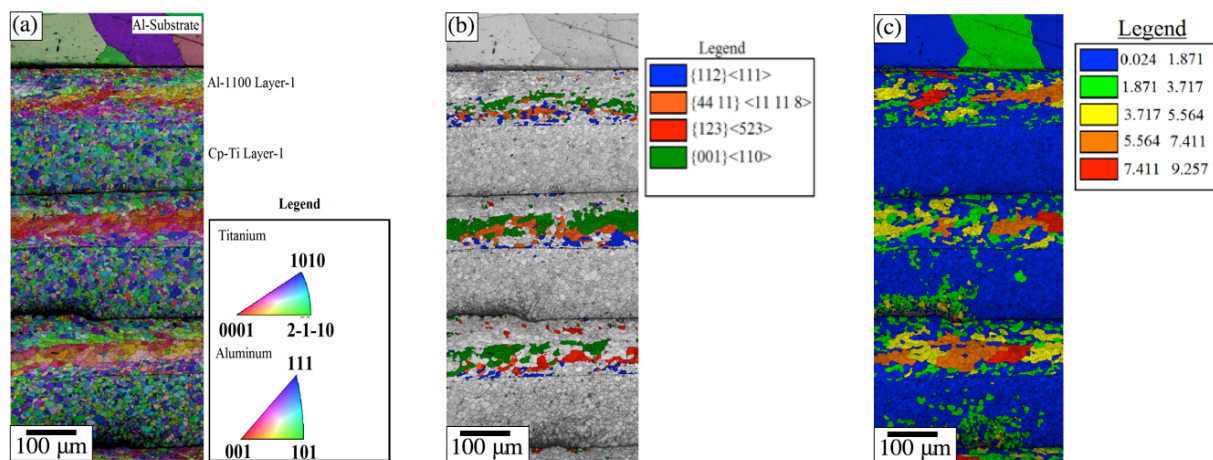


Figure 6.3 (a) IPF overlaid with image quality maps showing (b) Showing the crystal orientations overlaid on an image quality map (c) Shows the grain orientation spread

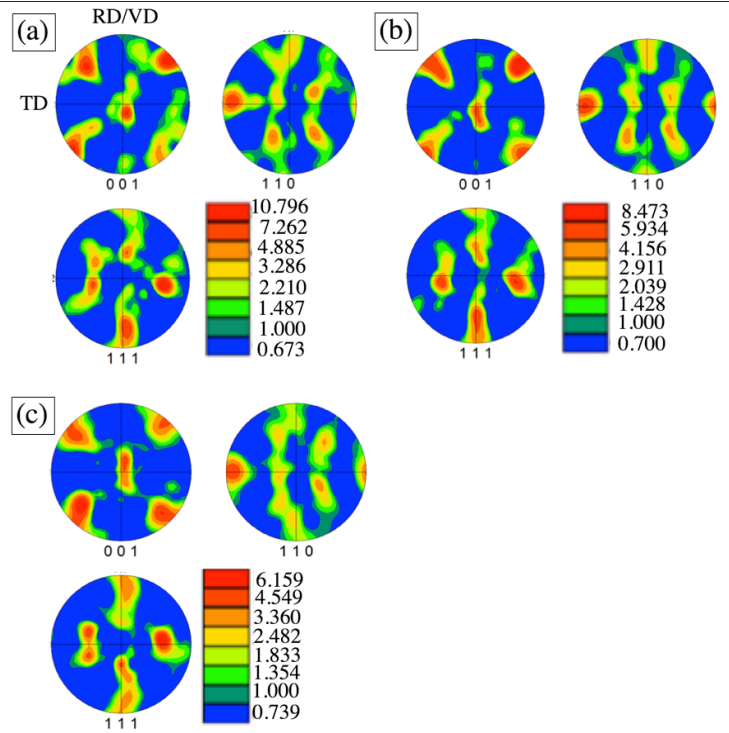


Figure 6.4 Texture maps of Al-1100 (a) Layer-1 (b) Layer-2 (c) layer3 showing the presence of a strong $\{001\}\langle 110 \rangle$ rotated cube texture

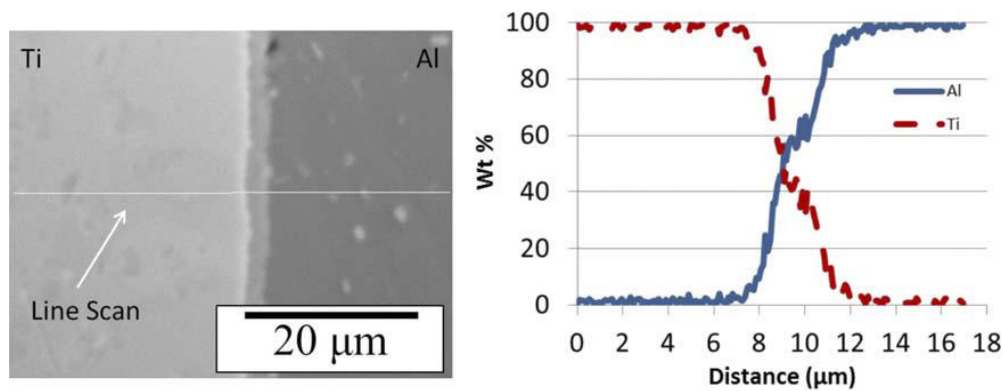


Figure 6.5 Showing the region of the interface where surface roughness is minimum. The diffusion distance and the thickness of the intermetallic layer is about 2-3 microns

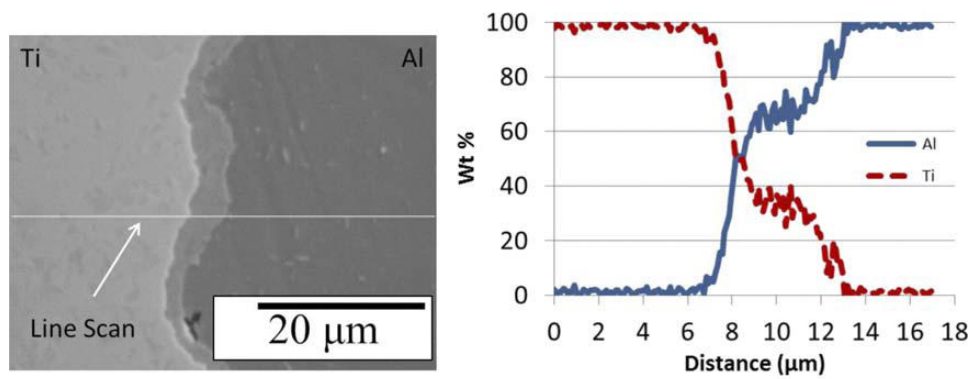


Figure 6.6 Showing the region of the interface near the sonotrode affected region showing significant interdiffusion of alloying elements. The diffusion distance and the thickness of the intermetallic layer is about 5 microns which is larger than that observed in figure 5.5

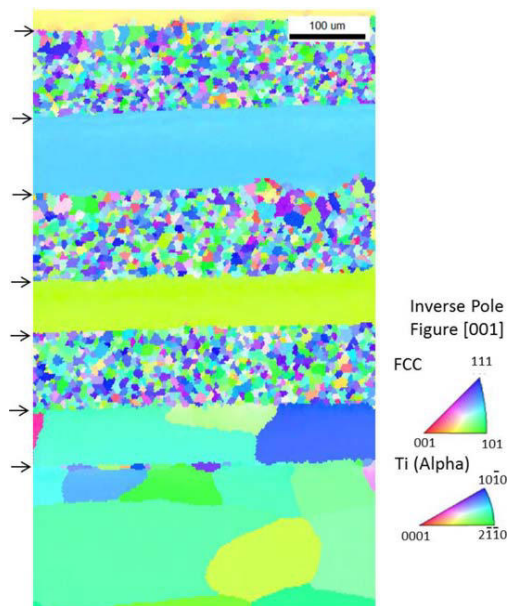


Figure 6.7 Shows the electron backscatter diffraction from the heat treated specimen. Note the grain growth at the Al interfaces while Cp-Ti does not show much difference.

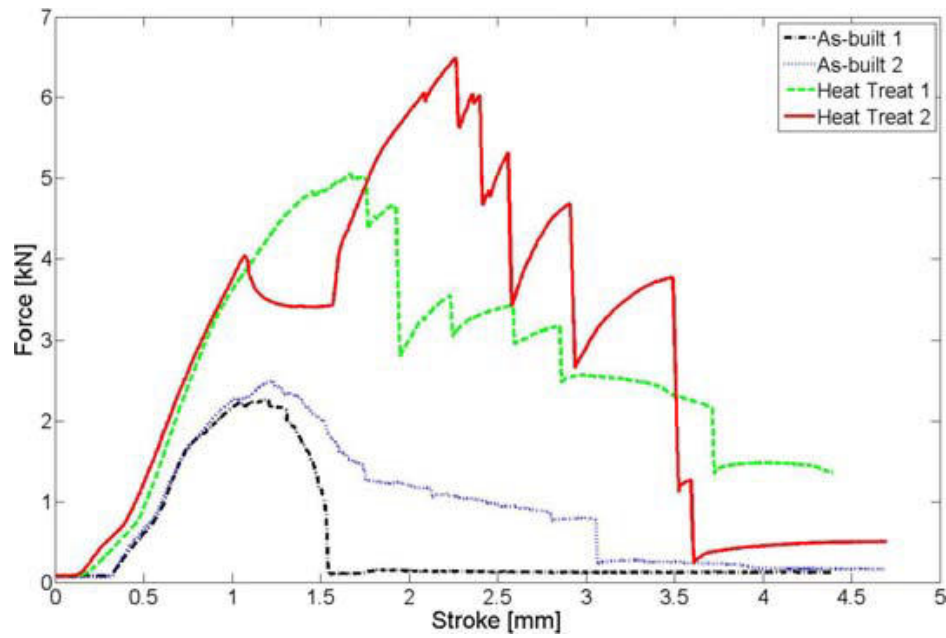


Figure 6.8 The results from the push pin tests on the as built and the heat treated samples

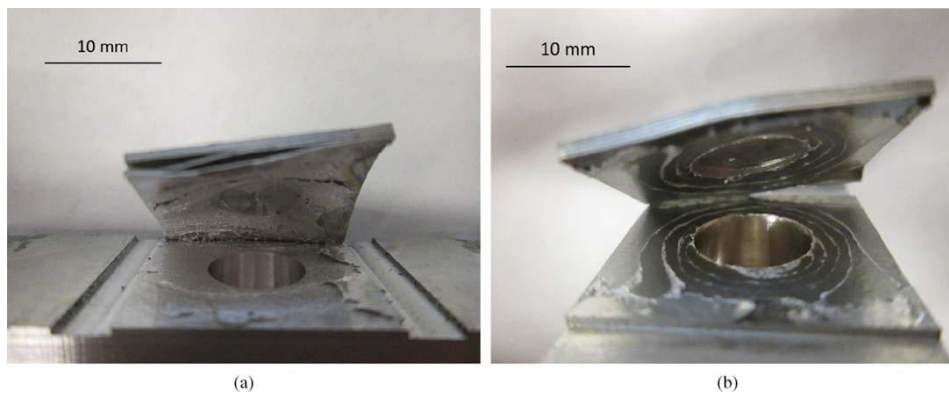


Figure 6.9 Shows the failure morphology of the push pin specimens (a) Heat treated (b) As built

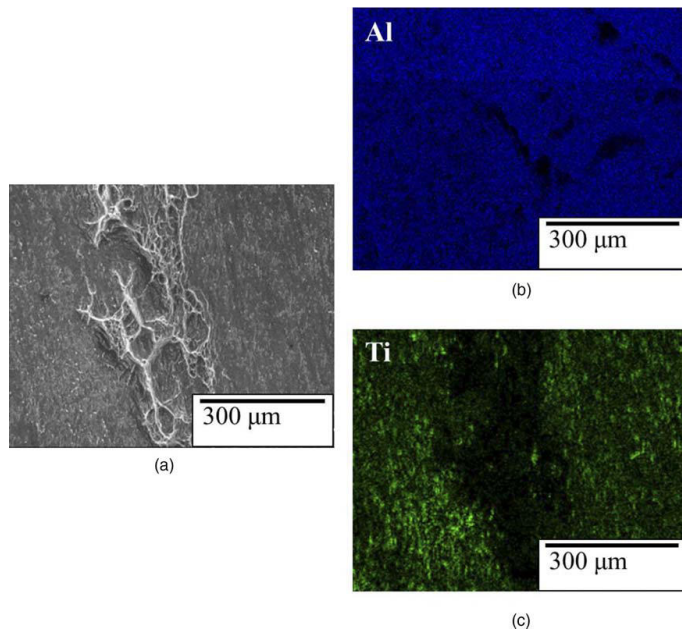


Figure 6.10 Shows the fractographs of the as welded specimen. (a) Shows the presence of localized ductile failure at the interface (b) Shows the Al distribution map (c) Shows the Ti distribution map. Showing the absence of Ti in the region where the sample failed in a ductile fashion meaning complete bonding between the Al and Ti layers at that location

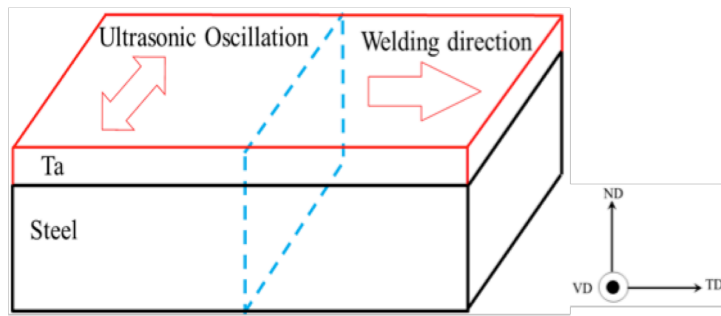


Figure 7.1 Schematic illustration of build fabricated by VHP-UAM and specimens cut off from the build (indicated by a dotted line)

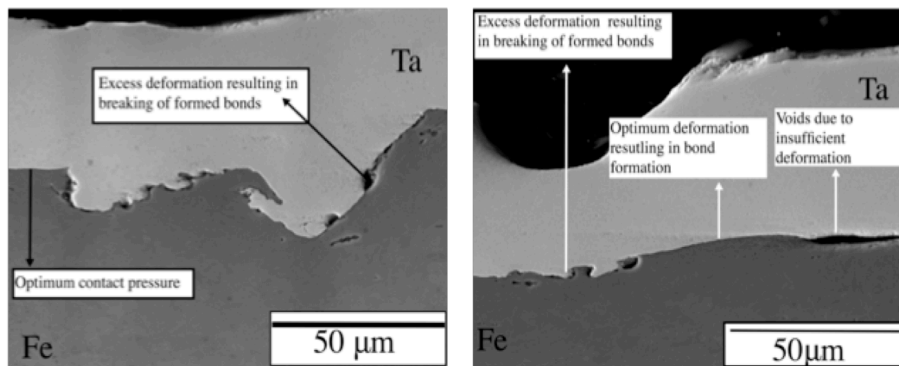


Figure 7.2 (a) SEM image showing bonded regions voids and the waves (b) SEM image showing waves at the interface

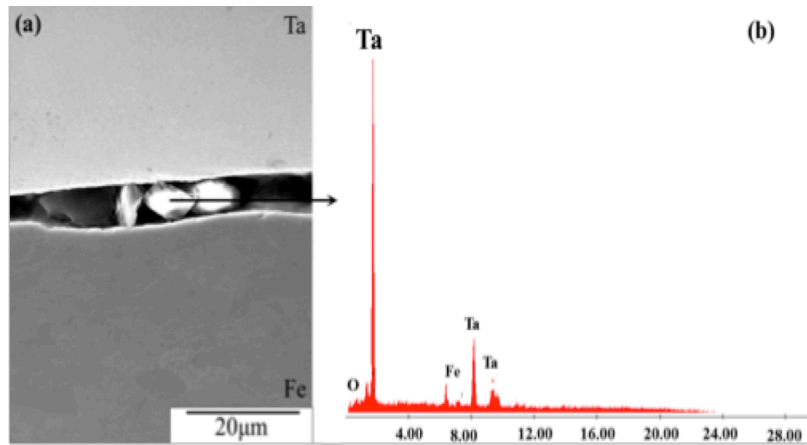


Figure 7.3 SEM micrographs of the Ta steel interface (a) Sliding debris (b) EDS spectrum of the debris

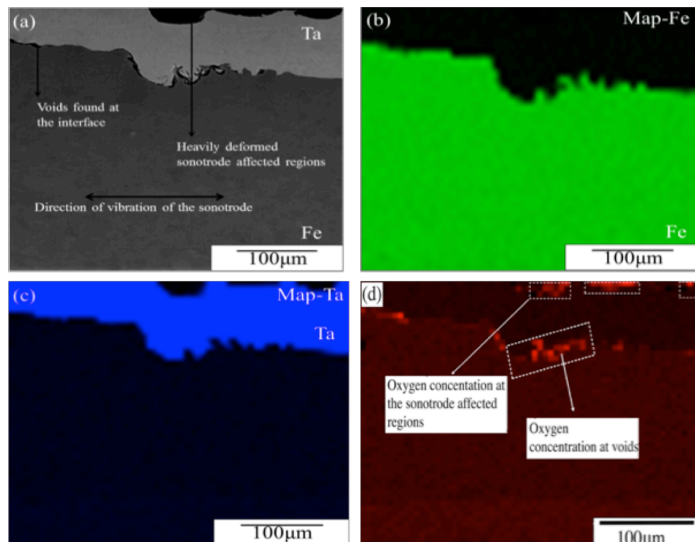


Figure 7.4 EDS maps show oxygen concentration at the interface and in the sonotrode affected regions

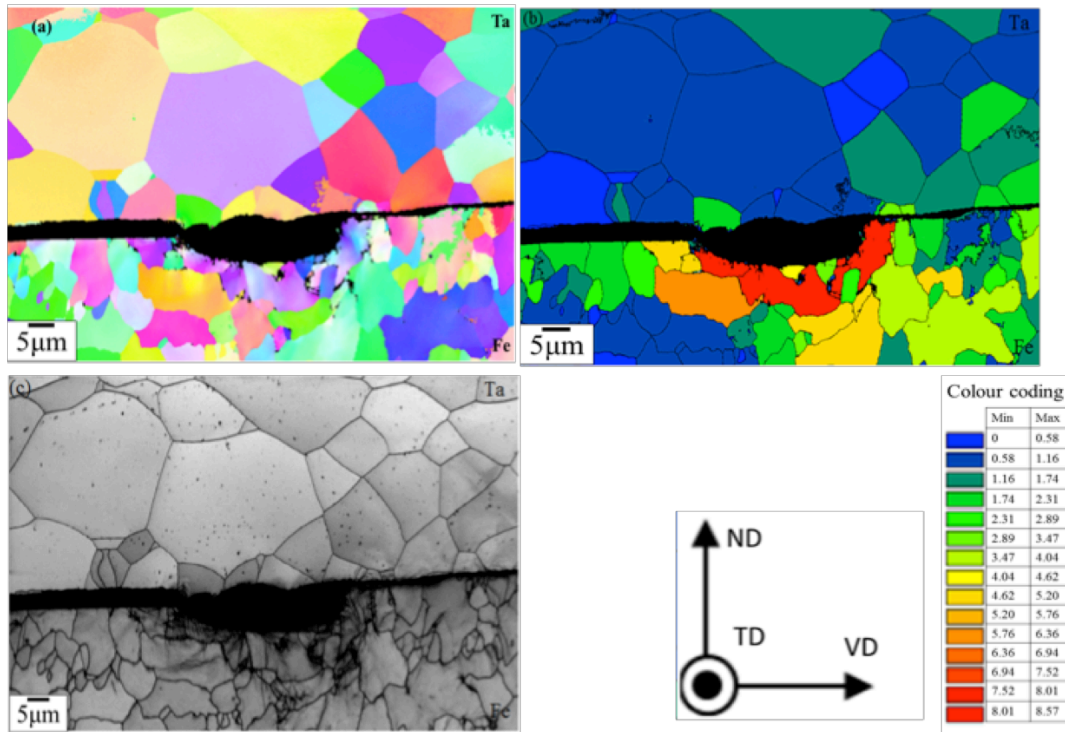


Figure 7.5 Microstructural characteristics of the unbounded area (a) Inverse pole figure of the unbonded region (b) Grain Orientation spread of the subject region(c) Image quality index of the corresponding region

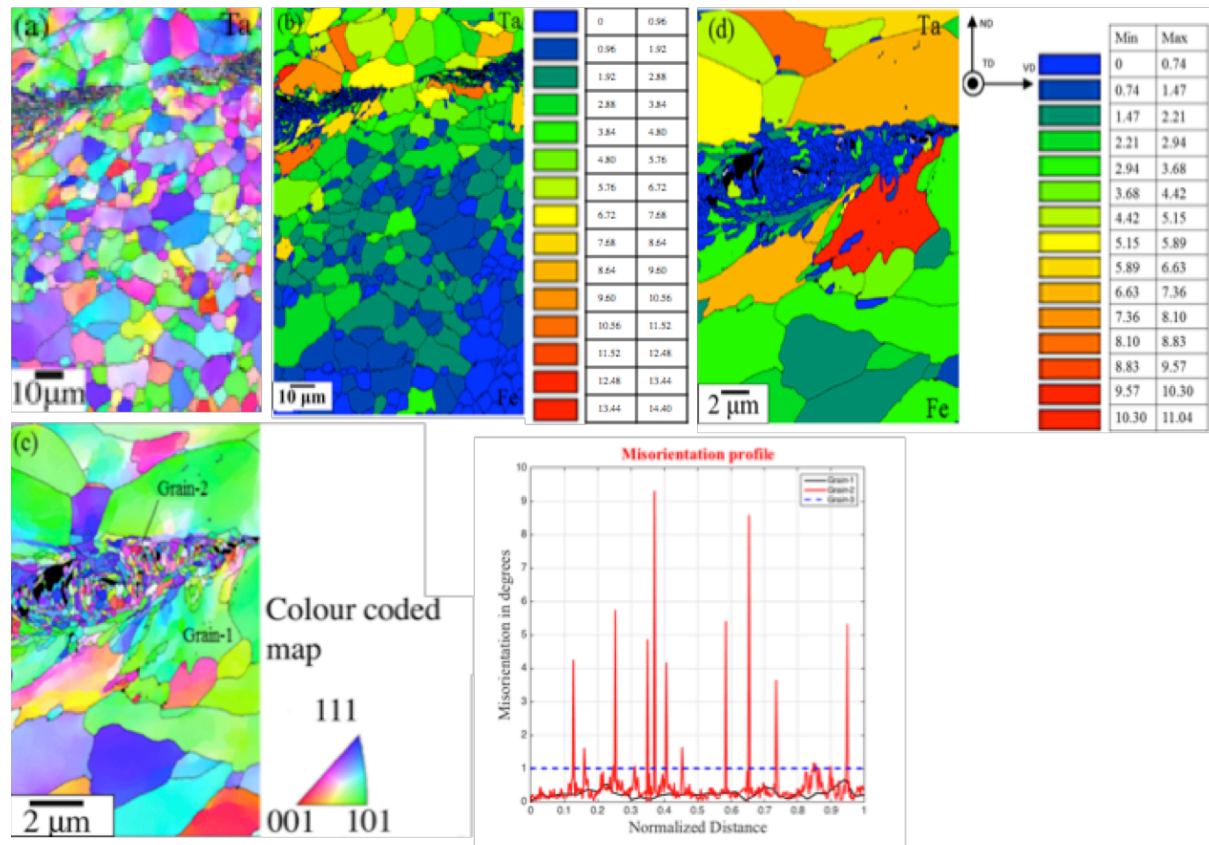


Figure 7.6 Microstructural characteristics of the bonded area (a) Inverse pole figure of the bonded region (b) Corresponding GOS (c) IPF of the a bonded region in higher mag (d) Corresponding GOS map

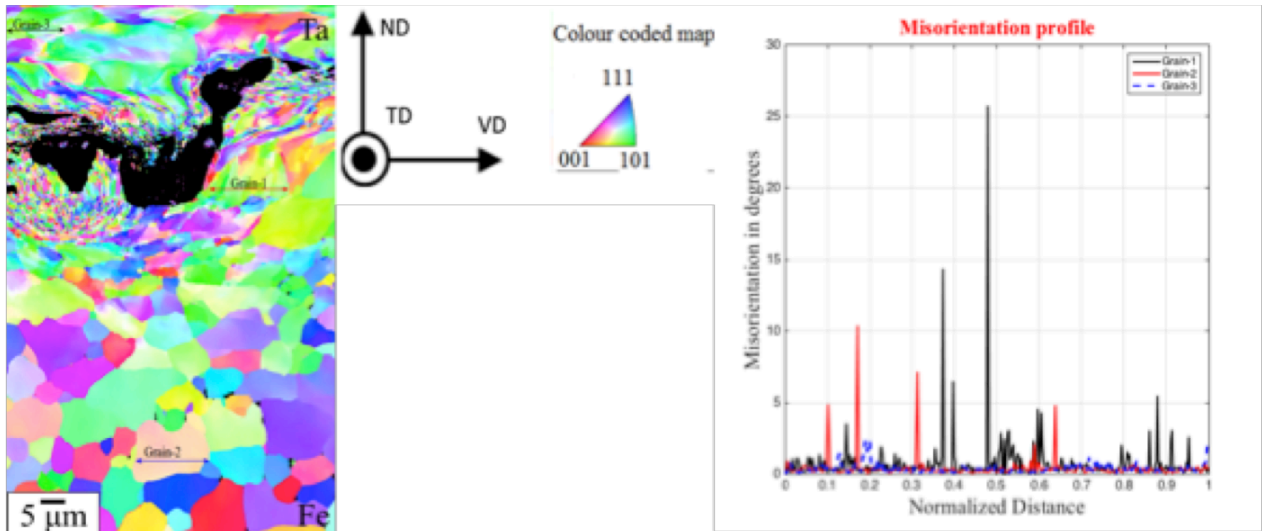


Figure 7.7 Microstructural characteristics of a heavily deformed region (a) Inverse pole figure
(b) Misorientation distribution for grain-1, grain-2 and grain-3

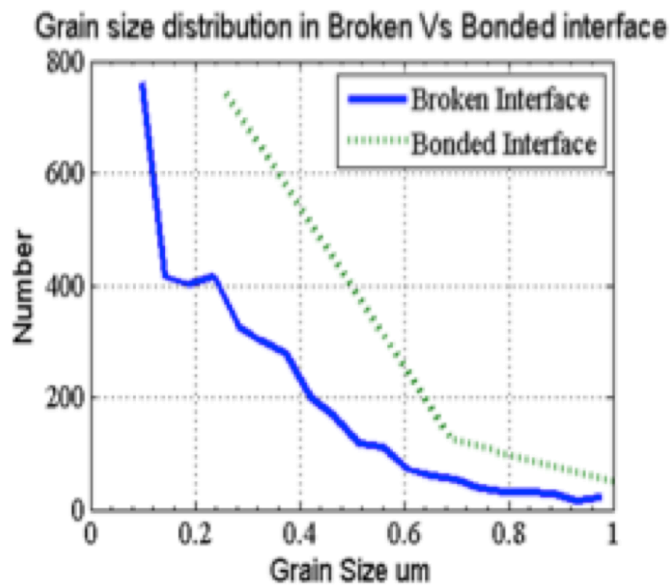


Figure 7.8 Grain size distribution in the both the bonded and the broken interface

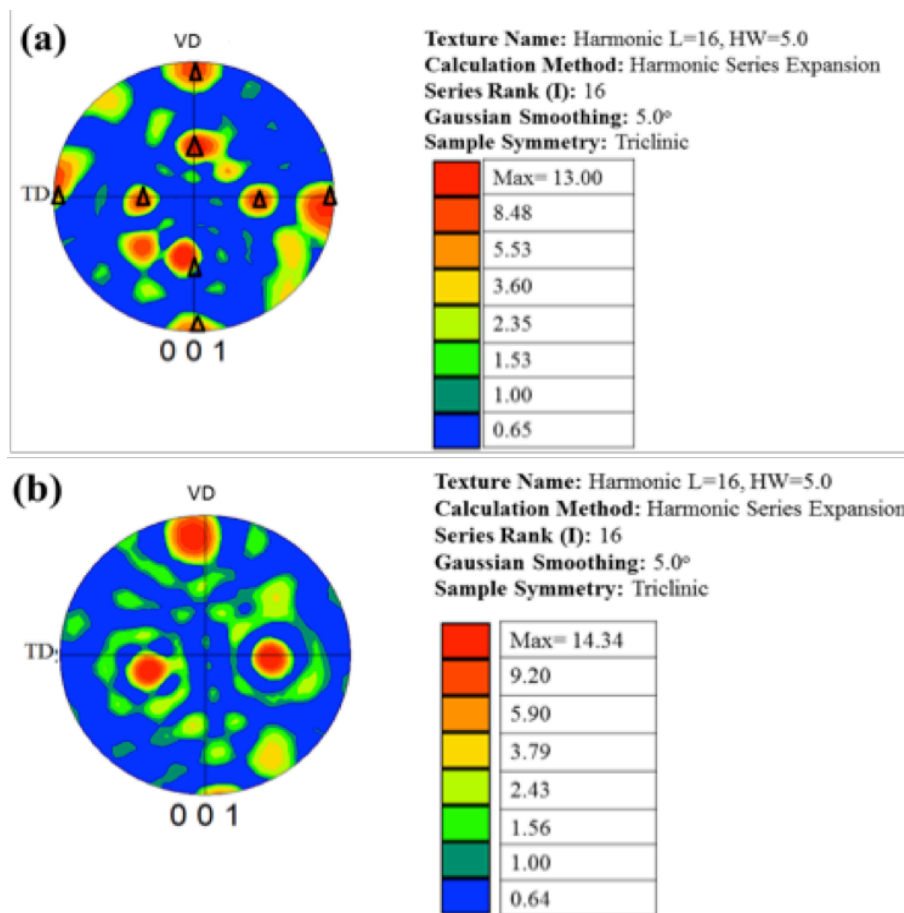


Figure 7.9 (a) Texture at the region where bonding was observed (b) micro texture at the region where excess deformation was observed

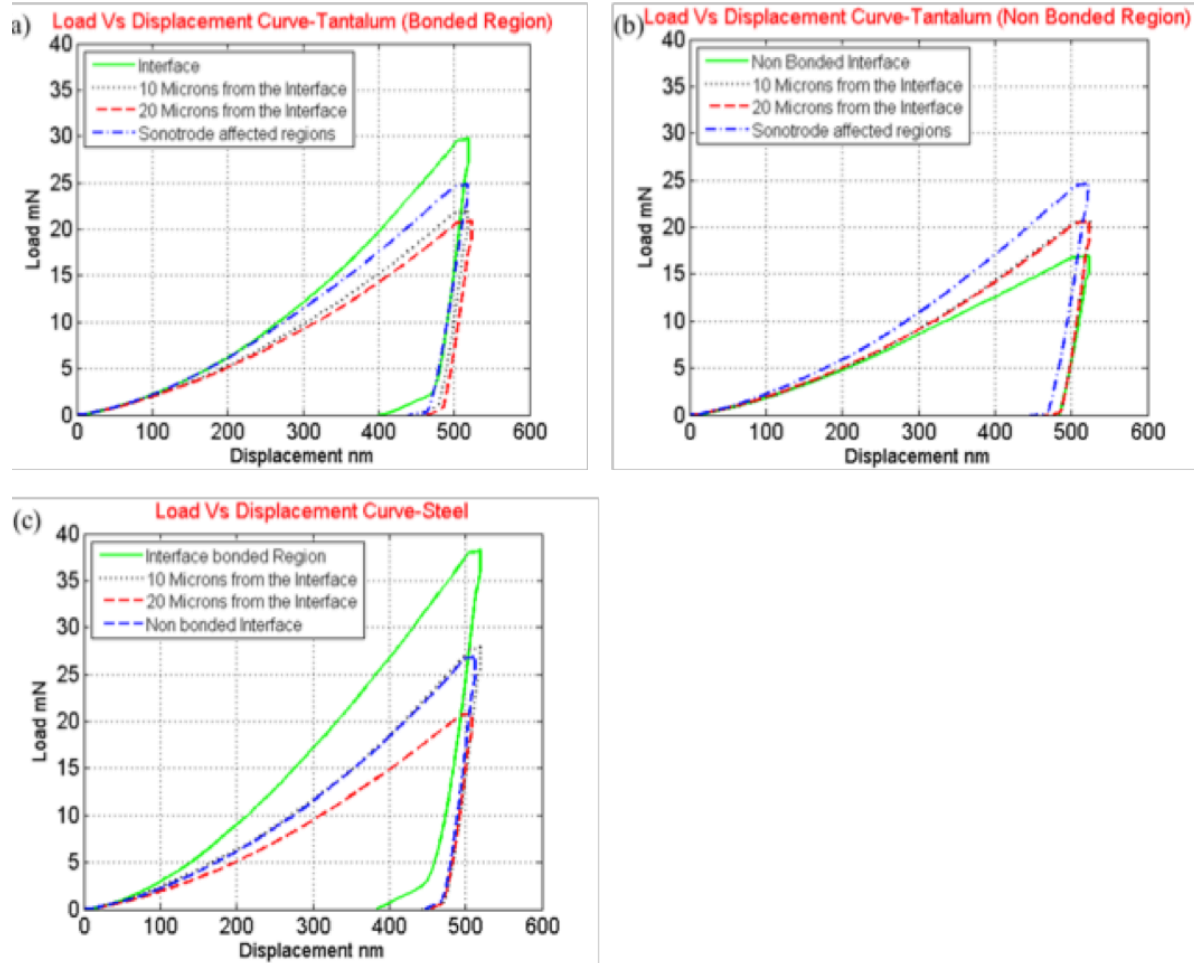


Figure 7.10 (a) Load Vs. displacement curves on the Ta side of the interface (bonded) (b) Load vs. displacement curves on the Ta side of the interface (not bonded) (c) Load vs. Displacement curves on the steel side of the interface

Vita

Niyanth was born in Vellore Tamil Nadu, India on 2nd April 1988. He did his schooling in Golden Gates Matriculation higher secondary school and graduated in 2005. Following high school he earned his undergraduate degree in metallurgical engineering from PSG College of Technology Coimbatore, India (2005-2009). He then worked for the refineries division of Indian Oil Corporation Limited and was responsible for plant maintenance and inspection from (June'09- May'12). Following the brief stint at Indian Oil Corporation Limited, he enrolled for a PhD program in Welding Engineering at The Ohio State University Columbus (June'12-July'13) and transferred over to the Bredesen Center program at UTK in Aug'13. His research during PhD focused primarily on manufacturing using the ultrasonic additive manufacturing and laser based direct metal deposition for energy applications. After graduation he will work for Oak Ridge National Laboratory as a postdoctoral researcher in the deposition science and technology group.